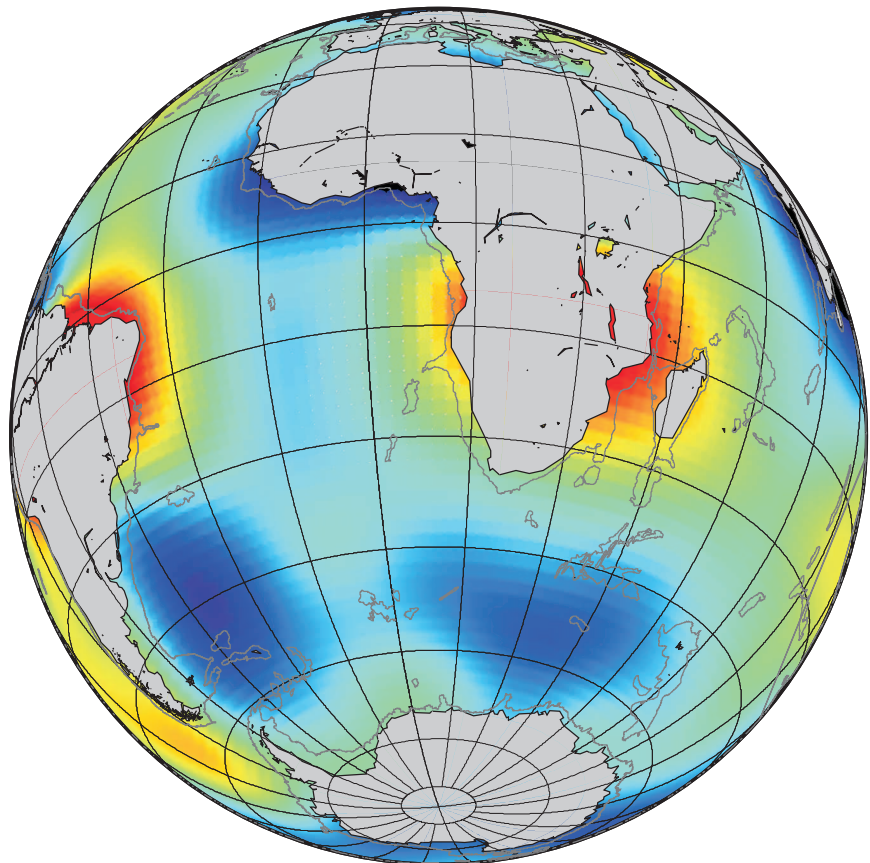


Validation of Oceanic Mass Changes derived from GRACE Gravimetry

*A comparison with independent data from Bottom Pressure
Recorders in the Southern Ocean*



Roelof Rietbroek
Delft University of Technology,
Faculty of Aerospace Engineering,
Chair of Astrodynamics and Satellite Systems

April 13, 2007

Validation of Oceanic Mass Changes derived from GRACE Gravimetry

*A comparison with independent data from Bottom Pressure Recorders in the
Southern Ocean*

Roelof Rietbroek

A thesis submitted for the degree of

Master of Science

at the research group

Astrodynamicics and Satellite systems

in the field of

Aerospace Engineering

at

Delft University of Technology

Submitted for approval on
March 20, 2007

Copyright © 2007, Roelof Rietbroek
Validation of Oceanic Mass Changes derived from GRACE Gravimetry.
A comparison with independent data from Bottom Pressure Recorders in
the Southern Ocean, Roelof Rietbroek, Delft, April 13, 2007.

This research has been carried out at the department:

Astrodynamic & Satellite systems
Faculty of Aerospace Engineering
University of Technology Delft.
Kluyverweg 1, 2629 HS Delft, The Netherlands.



This document was typeset with L^AT_EX 2_&. Reproduction or translation
of any part of this work in any form by print, photoprint or any other
means, without prior permission of either the author or the research
group is prohibited.

Cover illustration: GRACE GRGS equivalent water height for April
2004.

Contents

| | | |
|----------|---|-----------|
| 1 | Introduction | 1 |
| 2 | Scientific Justification | 3 |
| 3 | The Retrieval of Ocean Signals from Gravity | 6 |
| 3.1 | The Earth's Gravitational Field | 6 |
| 3.2 | Dynamic Gravitational Processes | 8 |
| 3.3 | GRACE Data Processing | 10 |
| 3.4 | Error Reduction | 12 |
| 3.4.1 | Spatial Gaussian Smoothing | 13 |
| 3.4.2 | Correlation Filter | 14 |
| 3.5 | Retrieval of Bottom Pressure and Ocean Currents | 15 |
| 3.5.1 | Geocenter Motion | 16 |
| 3.5.2 | Ocean Bottom Pressure | 16 |
| 3.5.3 | Geostrophic Currents | 16 |
| 4 | Bottom Pressure Recorder Analysis and Placement | 20 |
| 4.1 | Features of Bottom Pressure Recorders | 20 |
| 4.1.1 | Instrument | 20 |
| 4.1.2 | Bottom Pressure and Geostrophic Flow | 21 |
| 4.2 | Regions of BPR Placements | 22 |
| 4.2.1 | South Atlantic and Indian Ocean | 24 |
| 4.2.2 | Drake Passage and Argentine Basin | 25 |
| 4.3 | Data Processing | 26 |
| 4.3.1 | Tidal Analysis | 27 |
| 4.3.2 | Tidal Analysis Results | 28 |
| 4.3.3 | Spectral Analysis | 28 |
| 4.3.4 | Spectral Analysis Results | 30 |
| 4.3.5 | Averaging Methodology | 30 |
| 5 | GRACE Validation with Bottom Pressure Recorders | 32 |
| 5.1 | Correlation and Signal to Noise Ratio | 32 |
| 5.2 | Validation of the GRACE Post-Processing Filter | 33 |
| 5.3 | Results of the Bottom Pressure Comparison | 34 |
| 5.3.1 | Crozet Kerguelen Region | 35 |
| 5.3.2 | South Atlantic | 38 |
| 5.3.3 | Argentine Basin | 39 |
| 5.3.4 | Shags Rock Passage | 41 |
| 5.3.5 | Drake Passage | 44 |
| 5.4 | Results of the Geostrophic Flow Comparison | 46 |
| 5.4.1 | Crozet Kerguelen Passage | 46 |
| 5.4.2 | Argentine Basin | 48 |

| | | |
|----------|--|-------------|
| 5.4.3 | South Atlantic | 49 |
| 5.4.4 | Shags Rock and Drake Passage | 49 |
| 6 | Conclusions and Recommendations | 52 |
| 6.1 | Conclusion | 52 |
| 6.2 | Discussion and Recommendations | 54 |
| A | Correlation Tables | A.1 |
| A.1 | Bottom Pressure | A.1 |
| A.2 | Geostrophic Flow | A.5 |
| B | Time series of GRACE (CSR, GFZ) and in situ records | B.8 |
| B.1 | Bottom Pressure Series | B.8 |
| B.2 | Geostrophic Transport series | B.13 |
| C | Spatial Correlation Plots | C.15 |
| D | Power Spectral Densities | D.17 |

List of Figures

| | | |
|------|---|----|
| 3.1 | EIGENGL04S geoid in meters. | 8 |
| 3.2 | Gravity related dynamics on the Earth. | 9 |
| 3.3 | GRACE mission concept. | 10 |
| 3.4 | 1 dimensional example of aliasing into the mean. | 11 |
| 3.5 | Non-physical striations in the GRACE solution. | 13 |
| 3.6 | Geoid error degree amplitudes using Gaussian smoothing. | 14 |
| 3.7 | Striation filter applied to Stokes coefficients. | 15 |
| 3.8 | Coefficient weights for the degree method. | 18 |
| 3.9 | Global maps of eastward geostrophic flow from GRACE (GRGS) | 19 |
| 4.1 | Schematic representation of the mean vertically averaged flow. | 22 |
| 4.2 | DART buoy time series with derived annual sines. | 23 |
| 4.3 | AVISO gridded absolute dynamic topography around Antarctica. | 23 |
| 4.4 | AVISO gridded absolute dynamic topography around Kerguelen. | 25 |
| 4.5 | AVISO gridded absolute dynamic topography through the Drake Passage. | 26 |
| 4.6 | Current system in the South Atlantic ocean. | 27 |
| 4.7 | Amplitudes of the FES2004 model and local bottom pressure records. | 29 |
| 4.8 | Gaussian gridding for non-equispaced data | 30 |
| 5.1 | Improvement in correlation when using the striation filter. | 34 |
| 5.2 | Time series of the in situ records near Crozet and GRACE (GRGS). | 35 |
| 5.3 | Correlation vs. smoothing radius for the PIES and IO recorders. | 36 |
| 5.4 | Spatial correlation of the mean of IO1 and IO2 with GRACE (GRGS). | 37 |
| 5.5 | Variance of GRACE (GRGS) bottom pressure. | 38 |
| 5.6 | Variance of altimetric sea surface height. | 38 |
| 5.7 | Time series of the in situ records in the South Atlantic and GRACE (GRGS). | 39 |
| 5.8 | Spatial correlation of PIES2 with GRACE. | 40 |
| 5.9 | Time series of the in situ records in the Argentine Basin and GRACE (GRGS). | 41 |
| 5.10 | Spatial correlation of the mean of grace2 and grace3 with GRACE (GRGS). | 42 |
| 5.11 | Correlation vs. smoothing radius for the Argentine Basin and Shags Rock | 42 |
| 5.12 | Time series of the in situ records near Shags Rock and GRACE (GRGS). | 43 |
| 5.13 | Spatial correlation of SHAG2 with GRACE. | 43 |
| 5.14 | Time series of the in situ records in the Drake passage and GRACE (GFZ). | 44 |
| 5.15 | Correlation vs. smoothing radius for the Drake passage | 45 |
| 5.16 | Spatial correlation of DPS with GRACE (GRGS). | 45 |
| 5.17 | Transport time series of the in situ records near Crozet and GRACE. | 47 |
| 5.18 | Correlation vs. smoothing radius, geostrophic flow comparison. | 47 |
| 5.19 | Variance of the eastward component of geostrophic flow from GRACE | 48 |
| 5.20 | Transport time series of the in situ records in the Argentine basin. | 49 |
| 5.21 | Transport time series of the in situ records in the South Atlantic. | 50 |
| 5.22 | Transport time series of the in situ records in the Drake passage. | 51 |
| 5.23 | Spatial correlation of the Drake passage geostrophic flow with GRACE. | 51 |

| | | |
|------|---|------|
| B.1 | Time series of the in situ records near Crozet and GRACE (GFZ). | B.8 |
| B.2 | Time series of the in situ records near Crozet and GRACE (CSR). | B.9 |
| B.3 | Time series of the in situ records in the South Atlantic and GRACE (GFZ). . | B.9 |
| B.4 | Time series of the in situ records in the South Atlantic and GRACE (CSR). . | B.10 |
| B.5 | Time series of the in situ records in the Argentine Basin and GRACE (CSR). . | B.10 |
| B.6 | Time series of the in situ records near Shags Rock and GRACE (GFZ). . . . | B.11 |
| B.7 | Time series of the in situ records near Shags Rock and GRACE (CSR). . . . | B.11 |
| B.8 | Time series of the in situ records in the Drake passage and GRACE (GRGS). . | B.12 |
| B.9 | Time series of the in situ records in the Drake passage and GRACE (CSR). . | B.12 |
| B.10 | Transport time series of in situ records near Crozet and GRACE (CSR). . . . | B.13 |
| B.11 | Transport time series of in situ records in the Drake passage and GRACE (CSR). | B.13 |
| B.12 | Transport time series of in situ records in the South Atlantic and GRACE (CSR). | B.14 |
| B.13 | Transport time series of in situ records near Shags Rock and GRACE | B.14 |
| C.1 | Spatial correlation of IO1 and IO2 with GRACE (GRGS). | C.15 |
| C.2 | Spatial correlation of the PIES records with GRACE (GRGS). | C.16 |
| C.3 | Spatial correlation of grace2 and grace3 with GRACE (GRGS). | C.16 |

List of Tables

| | | |
|------|--|-----|
| 3.1 | Reference models used by the GRACE computation centers. | 12 |
| 4.1 | BPR locations, depths and observation periods. | 24 |
| A.1 | Pressure correlations of GRACE GRGS ($r_{smooth} = 600$ km) with BPRs. | A.1 |
| A.2 | Pressure correlations of GRACE CSR ($r_{smooth} = 600$ km) with BPRs. | A.2 |
| A.3 | Pressure correlations of GRACE GFZ ($r_{smooth} = 600$ km) with BPRs. | A.2 |
| A.4 | Pressure correlations of GRACE GRGS ($r_{smooth} = 800$ km) with BPRs. | A.3 |
| A.5 | Pressure correlations of GRACE CSR ($r_{smooth} = 800$ km) with BPRs. | A.3 |
| A.6 | Pressure correlations of GRACE GFZ ($r_{smooth} = 800$ km) with BPRs. | A.3 |
| A.7 | Pressure correlations of GRACE GRGS ($r_{smooth} = 1000$ km) with BPRs. | A.4 |
| A.8 | Pressure correlations of GRACE CSR ($r_{smooth} = 1000$ km) with BPRs. | A.4 |
| A.9 | Pressure correlations of GRACE GFZ ($r_{smooth} = 1000$ km) with BPRs. | A.4 |
| A.10 | Velocity correlations of GRACE GRGS ($r_{smooth} = 400$ km) with BPRs. | A.5 |
| A.11 | Velocity correlations of GRACE CSR ($r_{smooth} = 400$ km) with BPRs. | A.5 |
| A.12 | Velocity correlations of GRACE GFZ ($r_{smooth} = 400$ km) with BPRs. | A.5 |
| A.13 | Velocity correlations of GRACE GRGS ($r_{smooth} = 600$ km) with BPRs. | A.6 |
| A.14 | Velocity correlations of GRACE CSR ($r_{smooth} = 600$ km) with BPRs. | A.6 |
| A.15 | Velocity correlations of GRACE GFZ ($r_{smooth} = 600$ km) with BPRs. | A.6 |
| A.16 | Velocity correlations of GRACE GRGS ($r_{smooth} = 800$ km) with BPRs. | A.6 |
| A.17 | Velocity correlations of GRACE CSR ($r_{smooth} = 800$ km) with BPRs. | A.7 |
| A.18 | Velocity correlations of GRACE GFZ ($r_{smooth} = 800$ km) with BPRs. | A.7 |

Preface

This thesis concludes the Msc research project I carried out at the department of Astrodynamics and Satellite systems. The department is housed at the Aerospace Engineering faculty of the Delft University of Technology. Subjects studied vary from the determination of satellite orbits to the study of the system Earth using space-borne techniques. In particular, the latter one strongly appeals to me. The Msc courses I attended were primarily related to Earth observation, in which oceanography and gravity field determination deserved my special attention.

This project enabled me to combine those two preferred topics into a thesis involving the determination of the oceanic contribution of the time varying gravity field of the Earth. Furthermore, I was given the opportunity to fulfill a three month internship at IFREMER (Institut Français de Recherche pour l'Exploitation de la Mer) in Brest, France. During the internship I compared *in situ* observations measured at the bottom of the ocean with the time varying gravity field measured by the satellite mission GRACE (Gravity Recovery and Climate Experiment). This comparison showed promising results which resulted in a publication. Although the writing of the article took longer than expected and was therefore distracting me somewhat from the main project it served as a welcome and interesting hands-on experience in publishing.

The final stage of writing the report has been a rather stressing experience. In February 2007 I applied for a research position at the GeoForschungZentrum in Potsdam. The job offer was accepted soon after that and as of April 2007 I will be working in Germany. However this constrained the time to finish the thesis considerably and unfortunately caused some of my initial plans to be either reduced or canceled.

This thesis contains a general chapter on scientific justification, which explains the uses and scientific framework of this project. The chapter is digestible for anyone regardless of their background and should be read as a short essay. Furthermore, an abstract is provided, which contains the most important results. As for the remaining chapters, I sincerely hope that everybody is able to understand the main reasoning without having to look at the, sometimes monstrous looking, formulas.

Finally, there are several people who enabled the fulfillment of this project and deserve to be mentioned here. First of all my direct supervisor in Delft, Bert Wouters, was very supportive and was virtually always available for valuable advise and remarks. Together with my other tutor Ejo Schrama he enabled me to schedule my research in a flexible manner, giving me the freedom to choose my own areas of interest.

The data from many of the Bottom Pressure Recorders were kindly provided by Chris Hughes from the Proudman Oceanographic Laboratory. The PIES arrays in the South Atlantic were deployed by the Alfred Wegener Institute and were available through the help of Andreas Macrander. Furthermore, my supervisor during the internship, Pascal LeGrand,

was a great inspirator during the initial phase of the research and was the one who was responsible for the deployment of the recorders near Crozet and the Kerguelen.

The data from the French GRACE solutions and its necessary atmospheric and ocean models were kindly provided by Guillaume Ramillien and Jean-Michel Lemoine from the LEGOS institute in Toulouse. The other GRACE solutions were obtained in a less personal manner, from a ftp site to be precise, but my gratitude goes out to the GRACE-science team for supplying them.

Special thanks go out to my girlfriend Maaike Hollestein, who was in particular supportive during the tough last months. Although she was probably somewhat puzzled by the necessity of computers running over night and incomprehensible scrap paper stacked around the place, she provided me with the appreciated love and understanding I needed.

Roelof Rietbroek, Delft, April 13, 2007

Abstract

The satellite mission GRACE (Gravity Recovery and Climate Experiment) provides monthly solutions of the global gravity field of the Earth. Temporal variations in gravity reflect mass redistributions over the Earth. Those mass movements are caused by physical phenomena such as ice sheet dynamics, accumulation of hydrological masses over land, the dynamics in the solid Earth and the dynamics in the atmosphere and ocean.

This thesis work focuses on the validation of the oceanic mass variations derived from GRACE. The goal of the project is to compare the oceanic estimates from the space-borne instrument with independent data from pressure recorders (BPRs), deployed on the bottom of the deep ocean in the southern ocean. Although those datasets seem to be of a completely different nature they measure the same quantity. Namely, the variations of mass in the atmosphere and ocean, which in their turn influence the dynamics of the ocean. In this study the GRACE data is compared to the following two quantities:

- Local bottom pressure at the BPR stations
- Pairwise differences of local bottom pressure (a measure of the oceanic transport)

The processing methodology applied to the BPR records is as follows: The raw BPR data is de-tided using a harmonic analysis method. The data is then averaged (over a month) to make them equivalent to the GRACE solutions.

GRACE data from three different computing centers¹ are compared. The spherical harmonic coefficients are converted to equivalent water height and geostrophic flow, indicators of the variations in the ocean and atmosphere. The solution is filtered to remove correlated errors, after which the de-aliasing models are added back to the solutions. The final solution is obtained by applying a spatial averaging filter.

The bottom pressure comparison showed good agreements at locations in the southern Indian ocean, the south Atlantic and the Argentine basin. The best correlations obtained values over 0.8 and typical errors of below 1.5 cm. The analysis showed an apparent connection between phenomena in the Argentine basin and near Crozet. A two monthly mode appeared to be present in both areas. The capabilities of GRACE to detect this mode is marginal and further investigation is required.

The comparison for the geostrophic flow (pressure differences) showed a significant agreement in the south Indian ocean, with correlations over 0.7 and errors as low as 7 mm/s. Correlations in other areas were weak or even non existent.

We conclude that, for dedicated areas, GRACE shows the ability to measure realistic large scale variations in bottom pressure and geostrophic flow on spatial scales yet barely explored.

¹CSR release 1, Austin, GFZ release 3, Potsdam, GRGS, Toulouse



Chapter 1

Introduction

The GRACE mission (Gravity Recovery And Climate Experiment), launched in 2002, continuously measures the Earth's gravity field [46]. Temporal variations in gravity are caused by the redistribution of masses originating from sources such as the atmosphere, ocean, hydrology, ice-sheets or the solid Earth [45].

Compared to the gravity signal of continental hydrology, the contribution of the ocean is in general much weaker [51]. For example, the gravity signal associated with the seasonal filling of the Amazon Basin is about ten times stronger than that which is expected over the oceans. Detecting these variations from GRACE therefore represents a major challenge, but is of great value for climate studies and could furthermore be used for validation of ocean models.

One of the first studies related to the oceanic signal from satellite gravimetry established that GRACE was able to detect global ocean mass variations [7]. The results of this study suggested that GRACE could possibly be used on smaller scales.

Mass movements over the ocean generate fluctuations in bottom pressure. These variations of bottom pressure have some important implications. They cause oceanic currents to change in strength and direction, therefore influencing the convection processes in the ocean and subsequently the atmosphere. In theory, GRACE enables us to obtain direct estimates of the variation of currents which extend all the way to the sea floor. No other technique exists which offers this ability with global coverage.

Furthermore changes in bottom pressure cause the solid earth to deform under the oceanic load. An accurate knowledge of this loading is valuable information for solid earth research. GRACE offers a unique ability to contribute in this area by providing actual measurements of the ocean bottom pressure.

However, before measurements can be used, the quality of the oceanic component of GRACE must be thoroughly investigated. The goal of this study is to evaluate the quality of the GRACE oceanic signal by means of independent data from in situ bottom pressure recorders. Such a comparison significantly influences the conclusions that can be drawn from the interpretation of satellite data. A second goal is to validate the deep ocean currents derived from GRACE against local measurements.

In chapter 2 a brief ethical discussion is provided on the personal justification of the author regarding the performed research. It can be read separately from the other chapters and serves to illustrate the relevance of the research according to the author.

Secondly, a mathematical preliminary in chapter 3 elaborates on the derivation of the theory needed to retrieve oceanic signals from GRACE gravimetry. Furthermore, processing methods are presented which reduces errors in the GRACE data. These errors mainly manifest themselves as stripes in the north to south direction which have no physical meaning and thus contaminate the gravity estimate. The data processing techniques of the bottom pressure recorder data are presented in chapter 4. There, one can also find a discussion of the regions in which the recorders were placed.

The GRACE satellite data are then compared with data from bottom pressure recorders (BPRs) deployed at depths of several kilometers in the Indian ocean and in the South Atlantic. Such a comparison has been made before, using BPR observations close to the equator [27]. However, from that study no significant agreements where found with the GRACE observations. In chapter 5 more promising results are presented and different datasets are investigated. Both local bottom pressure and geostrophic flow are compared to GRACE.

Finally, the main conclusions are summarized in chapter 6 where one can also find a discussion of the results and recommendations for further research.

Chapter 2

Scientific Justification

Below you find a short essay on the justification of the scientific research carried out in this project. My opinion is that such a justification should be part of research in general, hence I desire the inclusion of this chapter in the thesis. My intention is to give the reader some insight into a few of my thoughts by raising some ethical questions.

I think every researcher has a moral obligation to ask himself questions like: "What are the social and environmental implications of my research?" "To what extent do my personal interests interfere with my ethical considerations?" "Do I think the money for my research could be better spent elsewhere?". The problem is that asking yourself such questions might possibly raise some conflicts, which we rather avoid. For example, I find it hard to believe that the researchers who did field surveys for the construction of the three Gorges Dam in China had no doubts on the devastating effects of the project they were supporting. However they felt they had no responsibility in the decision whether this dam should be built or not. This so-called ethical relativism appears to be easy to apply but removes the responsibility of the individuals themselves, something I find hard to accept. In order to incorporate the researcher's own ethical considerations I apply a more Kantian¹ like approach by asking the above questions to myself.

So what are the social and environmental implications of this research? To provide myself a satisfactory answer I need to first focus on the general purpose of the project and view it from a broader perspective. This project assesses the quality of the oceanic part of the gravity fields derived from measurements of the twin satellite mission GRACE. Validation of these satellite products are important because a realistic interpretation of the measured fields depend on it. But how useful are those so called gravity fields? The next paragraphs will give some more insight in the applications of the gravity fields.

Let's start with the bigger picture. Human kind is living on this planet without having a proper awareness of the influence it has on the systems of the Earth. Global anthropogenic effects now start having alarming proportions, still we don't have a clue what is really going on or what is going to happen. To sustain a healthy existence, we need more knowledge of our interaction with the physical systems on the Earth. Earth research should give us more insight into physical processes on the Earth and hopefully provides us with scientific evidence of the influence of human kind, which we can use to adapt appropriately. We should be made aware of the consequences of our actions and we will need to make personal sacrifices. Especially people in the western world need to give up their energy draining habits to establish a global sustainable future. Since I'm becoming increasingly aware of the fragility of our planet I'm willing to make those sacrifices. I strive to make other people aware of

¹After Immanuel Kant, German Philosopher, 1724-1804

that same feeling of responsibility for the Earth.

In Earth research, gravity field determination plays a crucial role. When the Earth's (changing) gravity field would be known accurately we could extract information of the internal structure of the Earth and its associated dynamics. Furthermore, we could extract information on the energy exchanges over the globe through ocean currents both on the surface as well as in the deep ocean, serving as important input for climatological models. Gravity field determination would enable us to monitor the exchange of water masses between the ocean and land ice masses, associated with sea level rise. And it could supply information on the hydrological systems present on the Earth. We would be able to detect natural resources underneath the surface, such as gas reservoirs, aquifers and oil deposits. Although, considering the current state of the technology, some of these topics are still out of reach, scientists are making progress.

The above research topics might hopefully contribute to a broader awareness of the interaction of the human kind with the Earth. An example of a study which contributes to this awareness can be found in a recent article published in Nature, which concluded that the rate of run-off from the Greenland ice-sheet was 2.5 times as high in the period 2004-2006 compared to that in the period 2002-2004 [50]. Although it is still possible that this meltdown is part of a decadal cycle it shows us the unique ability of GRACE to monitor the variations of the ice shelves. And most importantly, it shows this to a broad public.

The topic of this thesis is only a very small contribution to this awareness. Therefore it is hard to quantify the associated social implications. But, from another perspective, there are little social threats associated with the GRACE mission, since it is a purely scientific mission. Interesting to note: this might be different when GRACE would have the ability to detect underground deposits of oil. Then other large commercial players would get involved, desiring the exploitation of the discovered resources possibly at the cost of social interests.

The GRACE mission does have an environmental impact. One could argue that launching satellites is environmentally unfriendly. I did not quantify the environmental impact of the mission let alone the impact of the research carried out for this thesis. However, I can't think of any severe environmental consequences, which would convince me that the environmental loads outweigh the scientific potential of this mission.

Working with real satellite data is a pleasure for me. It gives me a comfortable vibe of doing useful research, concerned with global phenomena associated with the ocean and climate. Thus in this case, my personal interests go hand in hand with my ethical values. Concerning Earth system research I could think of possible personal ethical conflicts though. As a minor example, research related opportunities to travel around the globe conflict with my view on minimizing air travel.

The design and operation of satellite missions and deployment of in situ sensors are very expensive. The GRACE mission has a total cost of €76 million [1]. However this is relatively cheap compared to other satellites since GRACE reuses the satellite bus design of the earlier CHAMP (Challenging Minisatellite Payload) mission. Could all this money be better spent? I think not.

On the short term this research only contributed to the validation of the GRACE mission products and to the general knowledge in the particular region of interest. On the long term this research is part of a long chain of research subjects which potentially can lead to important results such as more accurate climate model output. Unfortunately no results are guaranteed so this research could be wasted money and energy. But let's relate this



to the example of the military industry. In this industry ridiculous amounts of money are spent on weaponry, which has potentially harmful consequences in the future [37]. In the year 2006 the US government military budget was €347 billion, this accounts for 3.7 % of the gross national product [54]. In other words, if you have a salary of €3000 a month you would (unvoluntary) spend €111 a month on the military. I'd rather spent that money on Earth research which has potential beneficial consequences in the future. The fact that huge amounts of money are put into the military does not necessarily justify the spending of lesser amounts of money on Earth research. However, to me it serves as a good example to relate the research costs to a socially accepted, or better, tolerated, expenditure like the military industry.

Another example, just for the fun of it. I was not particularly impressed by a recent Hollywood movie, until I saw the price tag, \$ 210,000,000, the equivalent of 2.3 GRACE missions. Apparently, people rather spend money on bad movies than on something as significant as Earth research.

Given the considerations above, I feel comfortable with my involvement in this research. An important conclusion that every researcher should make individually for his/her work.

Chapter 3

The Retrieval of Ocean Signals from Gravity

This chapter is a mathematical elaboration on the retrieval of the oceanic signal from the gravity field. The techniques presented here will be referred to throughout the report. They represent the processing methodology applied to the used GRACE fields. The first section addresses the general representation of the gravity field in terms of spherical harmonics. The interested reader is referred to references [21], [51] and [52]. Section 3.3 briefly outlines the strategy to retrieve gravitational fields from the raw GRACE data. This processing is currently done at several centers in the world and requires extensive computational power. For further reading on this topic [20] and [26] are recommended. Section 3.4 and onward describe the GRACE post processing techniques applied in this thesis and form the basis of the performed research.

3.1 The Earth's Gravitational Field

From a distant perspective the Earth appears to be a perfect homogeneous sphere. The associated gravity field strength at a certain position would be described only by an inverse quadratic dependency of the distance from the Earth's center. However, the real Earth is an approximate ellipsoid and when observing closely, the Earth's surface is not smooth but shaped by topography. Furthermore, the real Earth is inhomogeneous and thus its density varies in lateral and radial directions. This result in an irregular gravity field. The general solution of the gravitational potential outside the surface of the Earth is a harmonic function and obeys Laplace equation. In spherical coordinates Laplace equation is written as:

$$\frac{1}{r^2} \frac{\partial}{\partial r} \left(r^2 \frac{\partial V}{\partial r} \right) + \frac{1}{r^2 \sin \theta} \frac{\partial}{\partial \theta} \left(\sin \theta \frac{\partial V}{\partial \theta} \right) + \frac{1}{r^2 \sin^2 \theta} \frac{\partial^2 V}{\partial \lambda^2} = 0 \quad (3.1)$$

Here V is the gravitational potential, r , θ and λ are the radius, colatitude and the longitude respectively. The analytical solution of equation 3.1 can be written as a double infinite sum [21]:

$$V(r, \theta, \lambda) = \frac{\mu}{r} \sum_{l=0}^{\infty} \sum_{m=0}^{l} \left(\frac{a}{r} \right)^l \bar{P}_{lm}(\cos \theta) [\bar{C}_{lm} \cos(m\lambda) + \bar{S}_{lm} \sin(m\lambda)] \quad (3.2)$$

The gravitational constant and mean radius of the Earth are denoted by μ and a respectively. Here, \bar{P}_{lm} are the associated Legendre polynomials of degree l and order m and \bar{C}_{lm} , \bar{S}_{lm} are the spherical harmonic geopotential coefficients. The bars denote the fully normalized versions of the parameters underneath. The normalization convention follows that of [21]

and is commonly applied in geodesy. The associated Legendre polynomials are defined as:

$$P_{lm}(x) = (1-x^2)^{m/2} \frac{d^m P_l(x)}{dx^m}$$

$$\text{with } P_l(x) = \frac{1}{(-2)^l l!} \frac{d^l}{dx^l} (1-x^2)^l$$

In order to normalize these polynomials we multiply the associated Legendre polynomials with a normalization factor N_{lm} .

$$\bar{P}_{lm}(x) = N_{lm} P_{lm}(x)$$

$$N_{lm}^2 = \frac{(2-\delta_{0m})(2l+1)(l-m)!}{(l+m)!}$$

In the remainder of the report we omit the bars for convenience. The Legendre polynomials can be calculated from recursive formulas (e.g. [30]).

The convergence of the potential series is guaranteed when the potential on the surface of the Earth, σ , is a square-integrable function:

$$\int_{\sigma} V(a, \theta, \lambda) d\sigma < \infty \quad (3.3)$$

The contribution of a certain degree, l , to the power spectrum is denoted by the signal degree variance:

$$\sigma_l^2 = \sum_{m=0}^l [C_{lm}^2 + S_{lm}^2] \quad (3.4)$$

According to Kaula's rule of thumb [28] this follows approximately:

$$\sigma_l^2 \approx 1.6 \cdot 10^{-10} / l^3 \quad (3.5)$$

To guarantee the convergence of the series a maximum proportionality to l^{-2} is required which is satisfied by the factor l^{-3} in Kaula's rule.

The sum of the gravitational potential and the centrifugal potential of the Earth with respect to the potential of a first approximation reference ellipsoid, U , is called the disturbing potential T .

$$T = V + \Phi - U \quad (3.6)$$

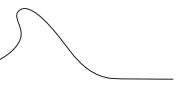
Here T is the disturbing potential, Φ is the centrifugal potential, caused by the rotation of the Earth. Since Φ is also contained in the normal potential U it cancels out in the disturbing potential. The reference ellipsoid commonly applied is that defined as the Geodetic Reference System 1980 (GRS80) [32].

The solution for a given constant potential describes a so-called equipotential surface. The geoid is that equipotential surface which corresponds to the hypothetical ocean surface at rest. A more practical definition uses the Bruns formula:

$$N = \frac{T}{\gamma} \quad (3.7)$$

The symbol γ is the normal gravitational acceleration of U . The geoid height is denoted by N and is the height above the reference ellipsoid. For the Earth maximum values are in the order of 100 m. Figure 3.1 shows the geoid for the Earth. As can be seen the geoid heights resemble tectonic features in the Earth and to a lesser extend mountain ridges. The geoid height can also be expanded in a spherical harmonic series [9].

$$N(\theta, \lambda) = a \sum_{l=0}^{\infty} \sum_{m=0}^l P_{lm}(\cos \theta) [C_{lm} \cos(m\lambda) + S_{lm} \sin(m\lambda)] \quad (3.8)$$



The coefficients differ only from those of equation 3.2 such that the contribution of the normal potential is subtracted from the first few zonal ($m = 0$ with $l=0, 2, 4, 6, 8$) coefficients. In practice, gravity fields are provided in such a set of coefficients, truncated at a certain degree l_{max} .

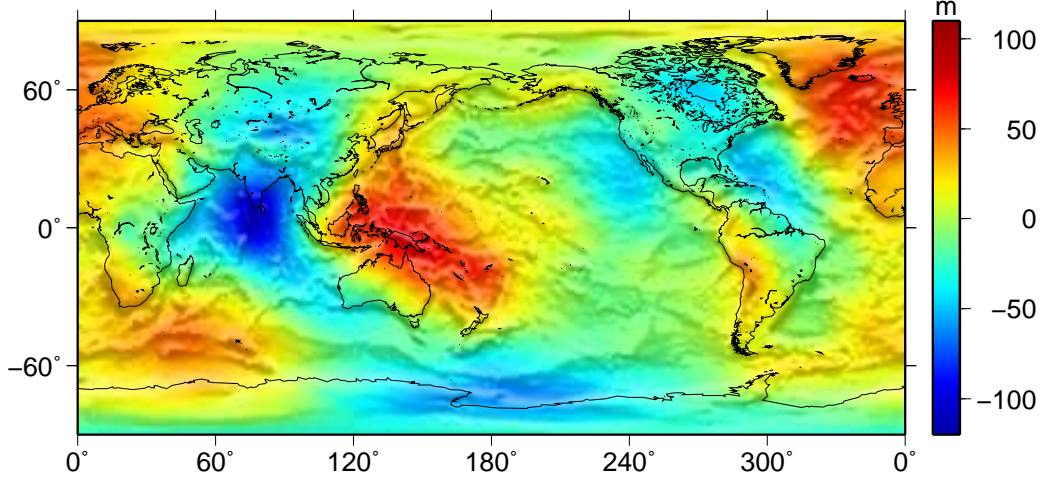


Figure 3.1: EIGENGL04S geoid in meters, shades represent topographic features of the Earth. Maximum degree of the spherical harmonic expansion is 150.

3.2 Dynamic Gravitational Processes

Although the gravity field mainly consists of a static contribution, there are dynamic processes, such as redistribution of ocean, ice, atmosphere, hydrological masses and the Earth's crust and interior as shown in fig. 3.2. Those phenomena result in a time dependent component. Measuring subsequent gravity fields in time enables such dynamic processes to be extracted from the gravity data. The satellite mission GRACE does exactly that, it is dedicated to measuring the variable gravity field averaged over about a month. But how can we retrieve those dynamic signals from the provided gravity solutions?

A reasonable assumption is to state that the redistribution of masses only occur in a thin shell on the outer side of the Earth [51]. This spherical shell should include the atmosphere, ocean, ice-sheets and strongly varying ground water storages. The atmosphere is the thickest part of the shell, consequently the complete layer will have a thickness of around 15 km. The change in surface density, in mass per area, of the spherical shell is obtained by radially integrating the change in density, $\Delta\rho$. [51]:

$$\Delta\sigma(\theta, \lambda) = \int_{thin\ shell} \Delta\rho(r, \theta, \lambda) dr \quad (3.9)$$

Again we can expand the change in surface density as a spherical harmonic series. To make the coefficients dimensionless the series is scaled by $a\rho_w$, with ρ_w representing the density of water.

$$\Delta\sigma(\theta, \lambda) = a\rho_w \sum_{l=0}^{\infty} \sum_{m=0}^l P_{lm}(\cos\theta) [\Delta\hat{C}_{lm} \cos(m\lambda) + \Delta\hat{S}_{lm} \sin(m\lambda)] \quad (3.10)$$

Commonly, the surface density anomaly is written in terms of equivalent water height, which is the change in surface density divided by the density of water. It can be shown that the

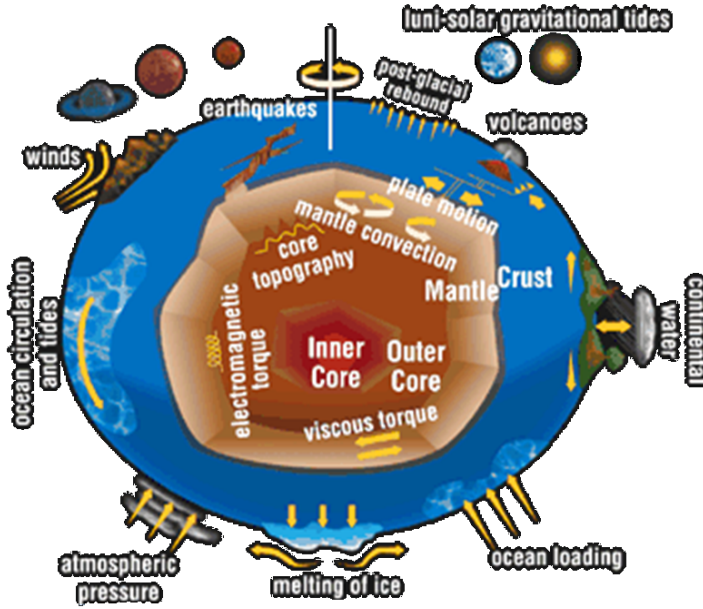


Figure 3.2: Gravity related dynamics on the Earth [8]

coefficients $\Delta\hat{C}_{lm}$ and $\Delta\hat{S}_{lm}$ can be written as a simple multiplication of coefficients ΔC_{lm} and ΔS_{lm} , which represent the change in the geopotential coefficients with respect to the geoid [51, 9].

$$\left\{ \begin{array}{l} \Delta\hat{C}_{lm} \\ \Delta\hat{S}_{lm} \end{array} \right\} = \frac{\rho_{ave}}{3\rho_w} \frac{2l+1}{1+k_l} \left\{ \begin{array}{l} \Delta C_{lm} \\ \Delta S_{lm} \end{array} \right\} \quad (3.11)$$

Here ρ_{ave} and ρ_w are the mean density of the Earth and the density of water respectively. Furthermore, two effects contribute to the change in surface density. The first effect is caused by the redistribution of masses within the shell. The second effect is caused by the elastic response of the solid Earth. The redistribution of the masses induce a change in surface load and therefore a deformation of the solid Earth. The associated change in potential is described by the load Love numbers k_l [14]. In this thesis, Love numbers are used calculated according to [19, 51].

The factor $2l+1$ in eq. 3.11 causes some problems. The most obvious is that it causes an amplification of the relative stronger noise present in the coefficients for large l . Additionally, an underlying and more fundamental problem is the possible divergence of the infinite series. The signal degree variance of the *change* in geopotential coefficients, $\Delta\sigma_l^2$, only guarantees convergence when:

$$\Delta\sigma_l^2 l^4 < \infty \text{ for } l = 0 \dots \infty \quad (3.12)$$

$$\text{with } \Delta\sigma_l^2 = \sum_{m=0}^l [\Delta C_{lm}^2 + \Delta S_{lm}^2] \quad (3.13)$$

Consequently, a behavior of $\Delta\sigma_l^2$ according to the power law of Kaula does not suffice here. However, the convergence of the series can still be guaranteed when applying a weight factor corresponding to a spatial average. This will be illustrated in section 3.4.

To summarize, the determination of the change in surface density yields information on the dynamical systems of the Earth. In this thesis, only the dynamics of the ocean will be

considered. However the contribution of the ocean is relatively small compared to that of continental hydrology with the latter up to ten times larger than the expected ocean signal.

3.3 GRACE Data Processing

This section will review some of the processing strategies used for analyzing the raw GRACE data. First, a general mission overview will be provided. Secondly, the principle of retrieving gravity field data from the measured quantities will be briefly addressed. Finally the models used to reduce aliasing will be described.

The satellite mission GRACE consist of two identical spacecraft orbiting in the same plane. In gravity field determination this configuration is known as low-low satellite-to-satellite tracking (SST). The two satellites are separated approximately 220 km along the track and currently orbit at a height of around 470 km. Each spacecraft carries the following payload [46]:

- An accelerometer to measure the non-gravitational forces.
- A geodetic GPS receiver for accurate positioning.
- A K-band ranging instrument to accurately measure the inter-satellite range rate.
- Two star cameras for attitude determination.

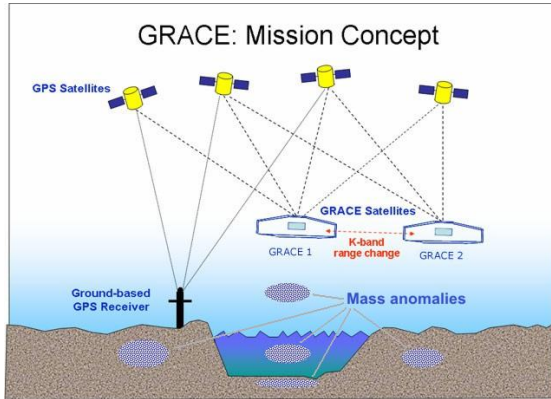


Figure 3.3: The GRACE mission concept showing the interaction between mass anomalies, the GRACE spacecraft and the GPS satellites adapted from: [47]

The information of these instruments is processed, using a large least square adaption, to retrieve the potential coefficients. The general idea is that when the two satellites pass over a mass anomaly on Earth, their inter-satellite distance will change. This is illustrated in fig. 3.3. Using energy considerations, the difference in potential at the locations of the two satellites can be approximately described by [26]:

$$V_{12} \approx |\dot{\mathbf{x}}_1| \dot{r}_{12} \quad (3.14)$$

Here V_{12} is the potential difference between satellite 1 and 2, $\dot{\mathbf{x}}_1$ is the absolute time derivative of the position vector of satellite 1. The range rate, in the line of sight, between the

spacecraft is denoted by $\dot{\rho}_{12}$. The latter term is very small and must therefore be known with accuracies in the order of microns per second [26]. This quantity is measured by the K-band ranging instrument. The first term is in the order of several km/s and therefore the accuracy requirement is less stringent (mm/s). Consequently it can be derived from the orbit determination (GPS, star cameras).

Equation 3.14 is a rough approximation to the real situation. On the satellites act non-conservative forces, such as atmospheric drag and solar radiation pressure. These accelerations can be measured using the on board accelerometers and are used to correct the potential in eq. 3.14. Furthermore a second important contributor to the real potential difference are the apparent forces arising from the rotation of the Earth. These can again be derived from orbit determination of the satellites.

The potential difference V_{12} can be derived from eq. 3.2 and is consequently a linear function of the unknowns C_{lm} and S_{lm} . A large amount of GRACE observations can now be coupled to the unknown potential coefficients and are solved using a least square method. For a set of coefficients up to degree 120 a month's worth of GRACE data are typically used. Therefore, GRACE is able to provide global monthly *mean* fields of the gravity.

The fact that GRACE can only provide monthly mean solutions exposes one of the main shortcomings in the mission. The true potential is dependent on high frequency phenomena, such as tides and variations in the atmosphere and ocean. As a result these phenomena alias into the solutions. Aliasing occurs when the Nyquist¹ frequency of the sampling is lower than the maximum frequency of the, to be measured, signal. As an analogy, fig. 3.4 illustrates the effect of aliasing for the mean of a sine wave sampled above the frequency of the signal. Aliasing in this example causes a relative error of about 20% in the calculated mean.

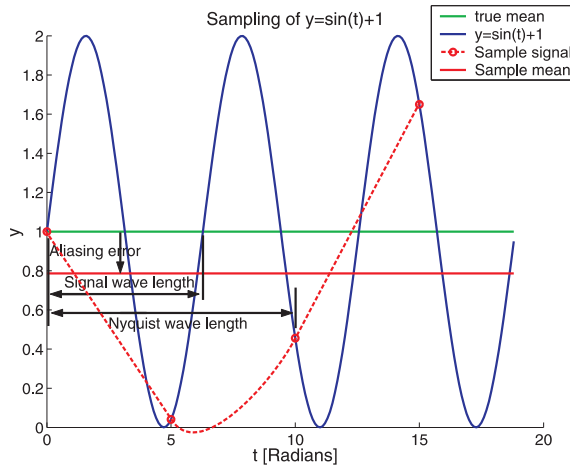


Figure 3.4: One dimensional example of aliasing of an under-sampled signal into the mean of the function $y = \sin t + 1$. The sampling interval is 5 radians and the Nyquist wave length is π radians.

In the GRACE processing the effect of aliasing is reduced by using tide models, ocean models and atmospheric models. The effect on the potential of these models is subtracted before the least square adjustment. Then, after calculating the Stokes coefficients, monthly averages must be added back to the GRACE estimates to retrieve the complete oceanic signal. These corrections are supplied as dealiasing products expressed as spherical harmonic coefficients. Since the models contain errors the effect of aliasing can never be completely eliminated and remain significant. The solutions from the different GRACE computing

¹This corresponds to half of the sampling frequency. After Harry Nyquist, Swedish physicist.

centers differ in the models used and in the method of orbit determination. Table 3.1 shows the differences in background models between the centers. The four centers considered are:

- The Centre of Space Research in Austin, Texas (CSR).
- GeoForschungsZentrum Potsdam, Germany (GFZ).
- Jet Propulsion Laboratory in Pasadena, California (JPL).
- A collaboration between Groupe de Recherche de Géodésie Spatiale and Centre National d'Etudes Spatiales Toulouse, France (GRGS-CNES).

| | CSR (RL01) | GFZ (RL03) | JPL (RL03) | GRGS-CNES |
|-------------------|--------------------|-------------------|------------|--------------------|
| Reference geoid | GGM01C | EIGEN_CG03C | GGM02C | EIGEN_GRACE02S |
| Maximum degree | 120 | 120 | 120 | 50 |
| Atmospheric model | ECMWF ^a | ECMWF | ECMWF | ECMWF |
| Ocean model | PPHA ^b | OMCT ^c | OMCT | MOG2D ^d |
| Ocean tide model | barotropic | baroclinic | baroclinic | barotropic |
| | CSR 4.0 | FES2004 | FES2004 | FES2004 |
| Solid Earth tide | IERS2003 | IERS2003 | IERS2003 | IERS2003 |

^a3D Atmospheric fields from European Center for Medium-Range Weather Forecasts

^bAfter Pacanowski, Ponte, Hirose and Ali, JPL

^cOcean Model for Circulation and Tides [48]

^d2-D gravity waves ocean model [4]

Table 3.1: Used (reference) models and maximum solution degrees for the different computing centers.

In this thesis the emphasis will be on the GRGS-CNES solution. This solution is provided up to degree 50, where the higher degree coefficients are constrained toward the static field. Although the spatial resolution is therefore limited to approximately 666 km [29], the GRACE estimates have certain advantages. One is the use of LAGEOS (Laser Geodynamics Satellites) data to estimate degree two coefficients which are not well determined by GRACE alone [10]. Furthermore, the GRACE-CNES solution provides monthly mean fields every 10 days. The higher temporal resolution of this solution is advantageous when comparing with short time series from BPR data.

3.4 Error Reduction

This section illustrate two methods to reduce the errors in the GRACE fields. Those errors originate from the before mentioned aliasing phenomena, caused by propagation of errors in the applied background models. Another cause of errors is the high sensitivity in the along-track direction of the satellite orbit, due to the aligned K-band ranging instrument. This anti-symmetrical sensitivity deteriorates the assumption that the measurements can be considered as uncorrelated point observations. It causes the "footprint" of the satellites to be of anti-symmetrical nature. As a consequence, mis-modeling of this effect will influence estimates of the coefficients through the inversion process.

The effect of correlated errors is manifested as striations in the surface density anomaly (eq. 3.10). The effect is shown in figure 3.5 for the GRACE-GRGS solution. For the solutions of CSR, GFZ and JPL these errors are even larger in the order of 800 mm, since the higher degree coefficients are noisier.

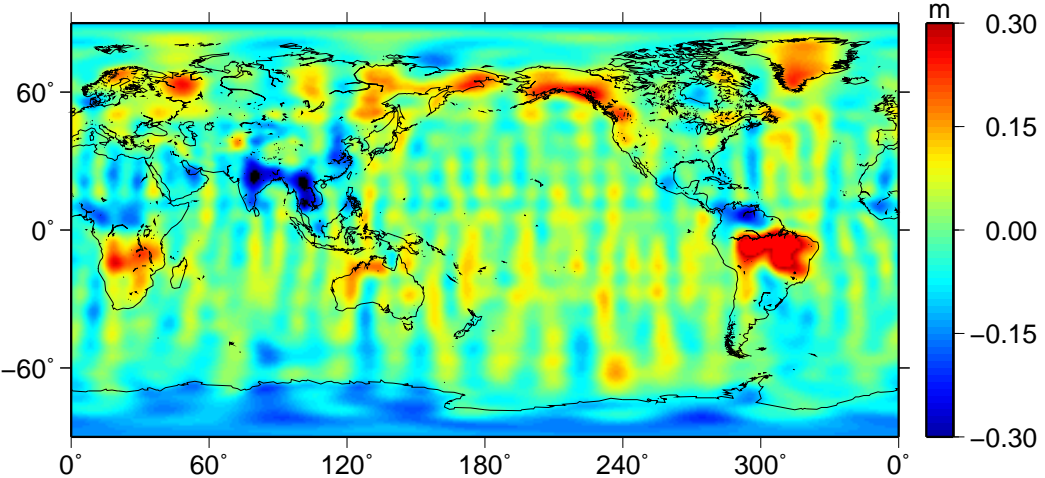


Figure 3.5: Non-physical striations in the GRACE solution, expressed in equivalent water height for the GRGS-CNES solution of April 2004.

3.4.1 Spatial Gaussian Smoothing

The first method to tackle the striation pattern is to average the data in the spatial domain. More specifically, a Gaussian smoothing can be applied to the coefficients which corresponds to a spatial average [51]. This method has the disadvantage that it decreases the spatial resolution and weakens the high resolution signal, but it provides a better accuracy over larger areas.

The spatial smoothing function is a radial symmetric Gaussian centered at the midpoint of interest [25]:

$$W(\phi) = \frac{b}{2\pi} \frac{\exp[-b(1 - \cos \phi)]}{1 - e^{-2b}} \quad (3.15)$$

$$b = \frac{\ln(2)}{(1 - \cos(r_{\frac{1}{2}}/a))} \quad (3.16)$$

Here ϕ represents the distance from the center point in radians. The symbol $r_{\frac{1}{2}}$ denotes the smoothing radius or half-width radius and is the distance along the sphere where $W(r_{\frac{1}{2}}/a) = 1/2$. It can be shown that the smoothed change in surface density, $\overline{\Delta\sigma}$, can be written as [51]:

$$\begin{aligned} \overline{\Delta\sigma}(\theta, \lambda) &= \frac{a\rho_{ave}}{3} \sum_{l=0}^{\infty} \sum_{m=0}^l \frac{2l+1}{1+k_l} W_l P_{lm}(\cos \theta) \\ &\times [\Delta C_{lm} \cos(m\lambda) + \Delta S_{lm} \sin(m\lambda)] \end{aligned} \quad (3.17)$$

The smoothing coefficient W_l can be calculated recursively [25], but in this thesis an approximate analytical function is used which is not sensitive to numerical instabilities [6].

$$W_l = \exp \left[-\frac{(lr_{\frac{1}{2}}/a)^2}{4 \ln(2)} \right] \quad (3.18)$$

The main advantage of this smoothing method can be seen from the equation above. The

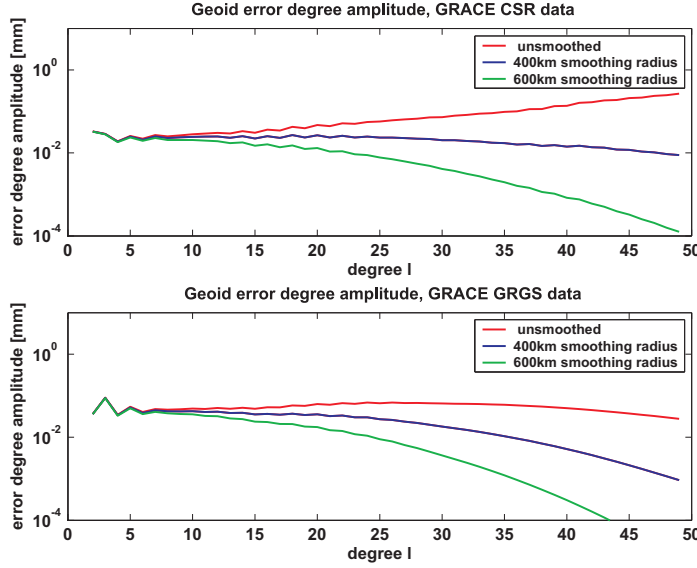


Figure 3.6: Geoid error degree amplitudes of GRACE CSR solution and GRACE-GRGS solution using 1) no smoothing, 2) Gaussian smoothing for half-width radius 400 km and 3) same for 600 km half-width radius.

weight of the coefficients decreases for higher degrees. Fundamentally this guarantees the infinite series in equation 3.17 to converge regardless of the power law behavior of the coefficients. Secondly, the higher noise levels of those coefficients propagate to a lesser extent in the averaged surface density anomaly. The effect of smoothing on the error degree variance is illustrated in figure 3.6. Here the degree error amplitudes decrease for large l when smoothing is applied. The error degree variance, $\sigma(c_l)^2$, of a spherical harmonic coefficient series is taken as a measure of the error and is expressed as.

$$\sigma(c_l)^2 = \sum_{m=0}^l [\sigma(C_{lm})^2 + \sigma(S_{lm})^2] \quad (3.19)$$

3.4.2 Correlation Filter

The second method used for decreasing errors is specifically designed to reduce the effect of the striations in the GRACE solution. The method is described in reference [44]. The main idea behind the method is to filter out the correlation between the coefficients. The following coefficients were found to be correlated [44].

- S_{lm} for odd l and $m >= 8$
- C_{lm} for odd l and $m >= 8$
- S_{lm} for even l and $m >= 8$
- C_{lm} for even l and $m >= 8$

In this thesis we use an adaption of the method of [44] which is more suitable for oceanographic purposes [5]. The main idea is to fit a higher order polynomial to each of the correlated series above and then subtract the polynomial from the original series. For a particular example the filtering is illustrated in fig. 3.7. The method is implemented as follows:

1. For each $m > 8$ select one of the four correlated series above.

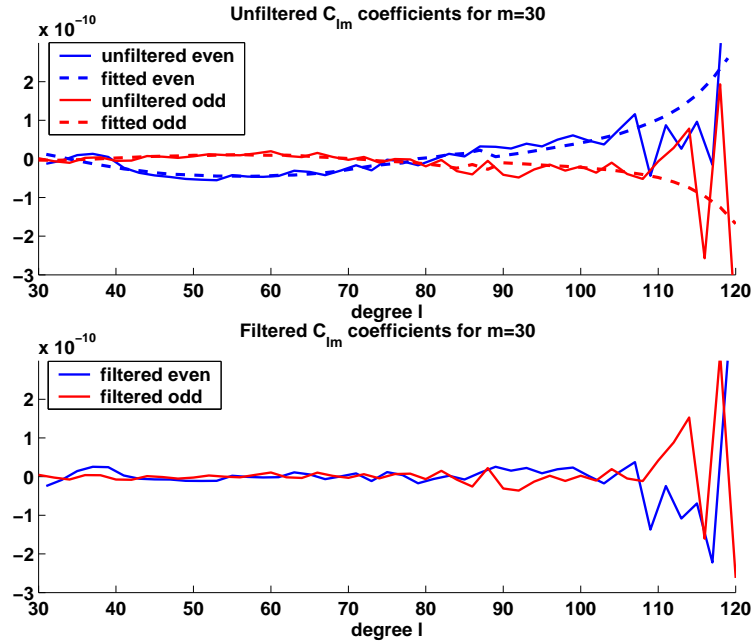


Figure 3.7: Striation filter applied to the C_{lm} Stokes coefficient for $m=30$ (CSR solution).

2. Fit a higher order (eg. 7) polynomial, as a function of l , to the series using least squares.
3. The filtered coefficients result from subtracting the fitted polynomial from the original series.
4. Do this for all of the four scenarios.

The filtering method is a non-physical way of handling correlated errors, it estimates the correlation error which is assumed to be solely an artifact but in fact can still contain real north-south signals. As a consequence real signals might be filtered out in the final results. This version has been evaluated against altimeter data with good results [5]. For completeness, we will evaluate the methods using in situ bottom pressure data in section 5.2. The method is optimized for the GRACE solutions with solution degrees up to 120. However we will also find a suitable scheme for the GRGS solution ,which has a maximum degree of only 50.

3.5 Retrieval of Bottom Pressure and Ocean Currents

This section combines the previous discussion in order to retrieve the ocean bottom pressure and geostrophic currents. Section 3.5.1 first describes the necessity to apply a correction to the GRACE data for the motion of the Earth's geocenter. Furthermore, expressions are provided, which yields the ocean bottom pressure and the geostrophic current components derived from GRACE. The derived expressions form the basis of the GRACE processing used throughout the thesis.

3.5.1 Geocenter Motion

The degree 1 stokes coefficients represent the position of the center of gravity of the Earth relative to the center of figure of the Earth. Predominantly due to seasonal effects the mass distribution changes over the globe. Such redistributions originate from for example ice accumulation at high latitudes during the winter months. Consequently, the center of gravity of the Earth displays seasonal variations. However, the GRACE satellites orbit the instantaneous center of gravity. This implies that the degree 1 coefficients are zero by definition. It is recommended to add back a model of this geocenter motion to the GRACE coefficients to make them consistent with measurements made on Earth [7]. In this study an annual geocenter model is applied which combines data from LAGEOS and the Topex Poseidon altimetry mission [11]. The annual amplitudes, a_{gx} , a_{gy} and a_{gz} relative to the terrestrial reference frame used are 1.1 mm, 3.7 mm and 3 mm respectively. The corresponding phases $\phi_{gx,y,z}$ are 16, 292, and 57 days with respect to the beginning of the year. The geocenter dependency on the time in days of a year, t , can now be constructed:

$$\begin{Bmatrix} x_g(t) \\ y_g(t) \\ z_g(t) \end{Bmatrix} = \begin{Bmatrix} a_{gx} \cos(2\pi(t - \phi_{gx})/365.25) \\ a_{gy} \cos(2\pi(t - \phi_{gy})/365.25) \\ a_{gz} \cos(2\pi(t - \phi_{gz})/365.25) \end{Bmatrix} \quad (3.20)$$

The coordinates of the geocenter, $x_g(t)$, $y_g(t)$ and $z_g(t)$ are related to the normalized degree 1 coefficients as follows [21][11]:

$$\begin{Bmatrix} C_{10}(t) \\ S_{11}(t) \\ C_{11}(t) \end{Bmatrix} = \frac{1}{\sqrt{3}a} \begin{Bmatrix} z_g(t) \\ y_g(t) \\ x_g(t) \end{Bmatrix} \quad (3.21)$$

3.5.2 Ocean Bottom Pressure

The pressure at the sea floor can be expressed as the surface density multiplied by, g , the gravitational acceleration. Therefore the change in bottom pressure, ΔP_{bott} , can be described as:

$$\begin{aligned} \Delta P_{bott}(\theta, \lambda) &= \frac{ag\rho_{ave}}{3} \sum_{l=0}^{\infty} \sum_{m=0}^l \frac{2l+1}{1+k_l} P_{lm}(\cos \theta) \\ &\times [\Delta C_{lm} \cos(m\lambda) + \Delta S_{lm} \sin(m\lambda)] \end{aligned} \quad (3.22)$$

And the smoothed bottom pressure $\Delta \bar{P}_{bott}$:

$$\begin{aligned} \Delta \bar{P}_{bott}(\theta, \lambda) &= \frac{ag\rho_{ave}}{3} \sum_{l=0}^{\infty} \sum_{m=0}^l \frac{2l+1}{1+k_l} W_l P_{lm}(\cos \theta) \\ &\times [\Delta C_{lm} \cos(m\lambda) + \Delta S_{lm} \sin(m\lambda)] \end{aligned} \quad (3.23)$$

As mentioned before, the variation of bottom pressure reflects the total change in mass above the sea floor. When estimating the true variation in pressure, one must add back the averaged model output from the atmospheric and oceanic models used in the processing. In case of the GRACE-GRGS solution these models correspond to the MOG2D barotropic model and the ECMWF pressure fields. The solutions of CSR and GFZ provide these combined models in the form of the GAC products.

3.5.3 Geostrophic Currents

Difference in pressure gradients cause ocean currents. When one assumes geostrophy, stating that the flow is quasi-steady and frictionless then the pressure gradient is in equilibrium with

the Coriolis force [52].

$$2\rho_w \vec{\Omega} \times \vec{v} \approx -\nabla P \quad (3.24)$$

Here $\vec{\Omega}$ is the angular rotation vector of the Earth and \vec{v} denotes the velocity vector. When one assumes that the vertical velocity is negligible compared to the horizontal velocities and that the bottom is approximately a level surface this can be written as two components in southward and eastward direction.

$$v_{south} \approx -\frac{1}{2\rho_w |\vec{\Omega}| a \sin \theta \cos \theta} \frac{\partial}{\partial \lambda} P_{bott} \quad (3.25)$$

$$v_{east} \approx \frac{1}{2\rho_w |\vec{\Omega}| a \cos \theta} \frac{\partial}{\partial \theta} P_{bott} \quad (3.26)$$

One can expand the change of the above components in spherical harmonics.

$$\begin{aligned} \Delta v_{south}(\theta, \lambda) &= -\frac{g\rho_{ave}}{6\rho_w |\vec{\Omega}| \sin \theta \cos \theta} \sum_{l=0}^{\infty} \sum_{m=0}^l P_{lm}(\cos \theta) \\ &\times [\Delta C_{lm}^s \cos(m\lambda) + \Delta S_{lm}^s \sin(m\lambda)] \end{aligned} \quad (3.27)$$

$$\begin{aligned} \Delta v_{east}(\theta, \lambda) &= \frac{g\rho_{ave}}{6\rho_w |\vec{\Omega}| \cos \theta} \sum_{l=0}^{\infty} \sum_{m=0}^l P_{lm}(\cos \theta) \\ &\times [\Delta C_{lm}^e \cos(m\lambda) + \Delta S_{lm}^e \sin(m\lambda)] \end{aligned} \quad (3.28)$$

The velocity stokes coefficients, $\Delta C_{lm}^{s,e}$, $\Delta S_{lm}^{s,e}$, can be written as a linear combination of the change of the potential coefficients. The coefficients of the southward current can be straightforwardly derived from the longitudinal derivative of equation 3.22 substituted in equation 3.25.

$$\left\{ \begin{array}{c} \Delta C_{lm}^s \\ \Delta S_{lm}^s \end{array} \right\} = \frac{m(2l+1)}{1+k_l} \left\{ \begin{array}{c} -\Delta S_{lm} \\ \Delta C_{lm} \end{array} \right\} \quad (3.29)$$

The derivation of the eastward coefficients is somewhat more complicated. It can be achieved by using recursive relations of the Legendre polynomials.

The approach is to use the recursive relation applied in [52]. This method is further referred to as the degree method as it uses a recursion relation dependent on neighboring degrees:

$$\begin{aligned} (2l+1) \sin \theta \frac{dP_{l,m}}{d\theta} &= -\frac{N_{l,m}}{N_{l-1,m}} (l+1)(l+m) P_{l-1,m} \\ &+ \frac{N_{l,m}}{N_{l+1,m}} l(l-m+1) P_{l+1,m} \end{aligned} \quad (3.30)$$

This recursive relation can be combined with equations 3.26 and 3.22. For a given l, m the resulting double summation displays two terms which have the common factor P_{lm} and which determine the coefficients ΔC_{lm}^e and ΔS_{lm}^e .

$$\begin{aligned} \left\{ \begin{array}{c} \Delta C_{lm}^e \\ \Delta S_{lm}^e \end{array} \right\} &= \frac{(l-1)(l-m)}{(1+k_l) \sin \theta} \frac{N_{l-1,m}}{N_{l,m}} \left\{ \begin{array}{c} \Delta C_{l-1,m} \\ \Delta S_{l-1,m} \end{array} \right\} \\ &- \frac{(l+2)(l+m+1)}{(1+k_l) \sin \theta} \frac{N_{l+1,m}}{N_{l,m}} \left\{ \begin{array}{c} \Delta C_{l+1,m} \\ \Delta S_{l+1,m} \end{array} \right\} \end{aligned} \quad (3.31)$$

Smoothed coefficients can be constructed by multiplying by the smoothing coefficient W_l .

$$\left\{ \begin{array}{c} \Delta \bar{C}_{lm}^{e,s} \\ \Delta \bar{S}_{lm}^{e,s} \end{array} \right\} = W_l \left\{ \begin{array}{c} \Delta C_{lm}^{e,s} \\ \Delta S_{lm}^{e,s} \end{array} \right\} \quad (3.32)$$

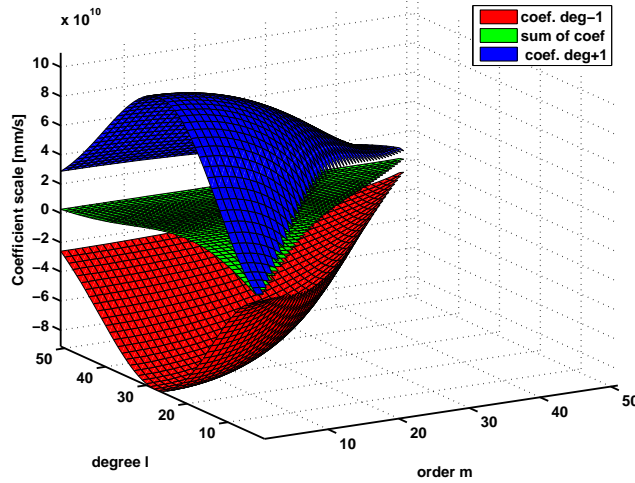


Figure 3.8: Coefficient weights for the degree method. Smoothing radius used is 400 km. The surfaces represent the weights of the coefficient factors of the terms in the right hand side of equation 3.31. The intermediate surface is the sum of the surfaces above and below. The latitude used is 50 degrees.

From equation 3.31 we can see that exactly those coefficients are used which were shown to be correlated earlier. This suggest that those correlated errors will propagate in the geostrophic flow. Figure 3.8 shows the weights which are assigned to the coefficients of varying degree and order. What can be observed is that the weights of the correlated coefficients are of opposite sign. This in fact reduces the correlation pattern. As coefficients of degree $l - 1$ and $l + 1$ have a correlated and similar error, these errors will partly be subtracted from each other.

In retrospect the reduction of the correlated error in the solution seems a logical consequence of the fact that north south striations in the GRACE bottom pressure would result in non-physical north south velocities. The eastward component is relatively unaffected by those striations.

An investigation of a different method to derive geostrophic flow was also made. This should theoretically not change the value of the geostrophic flow, however from a numerical perspective this possibly yields better results.

The method considered uses a recursion relation which relates the derivative of the Legendre polynomial with its neighbours varying in their order. It is referred to as the order method in subsequent discussions.

$$\begin{aligned} 2 \frac{dP_{l,m}}{d\theta} &= \frac{N_{l,m}}{N_{l,m-1}} (l+m)(l-m+1) P_{l,m-1} \\ &\quad - \frac{N_{l,m}}{N_{l,m+1}} P_{l,m+1} \end{aligned} \quad (3.33)$$

This yields for the geostrophic flow coefficients:

$$\left\{ \begin{array}{c} \Delta C_{lm}^e \\ \Delta S_{lm}^e \end{array} \right\} = - \frac{(2l+1)}{2(1+k_l)} \frac{N_{l,m-1}}{N_{l,m}} \frac{a_{m-1}(\lambda)}{a_m(\lambda)} \left\{ \begin{array}{c} \Delta C_{l,m-1} \\ \Delta S_{l,m-1} \end{array} \right\}$$

$$+ \frac{(2l+1)(l+m+1)(l-m)}{2(1+k_l)} \frac{N_{l,m+1}}{N_{l,m}} \frac{a_{m+1}(\lambda)}{a_m(\lambda)} \left\{ \begin{array}{l} \Delta C_{lm+1} \\ \Delta S_{lm+1} \end{array} \right\} \quad (3.34)$$

Where $a_m(\lambda) = \begin{cases} \cos m\lambda & \text{For } C_{l,m} \text{ coefficients} \\ \sin m\lambda & \text{For } S_{l,m} \text{ coefficients} \end{cases}$

Unfortunately, the a_m terms prohibit a closed form of spherical harmonic coefficients, because of the introduction of a dependency on longitude. Numerically, implementation can be done by considering all the summation terms independently.

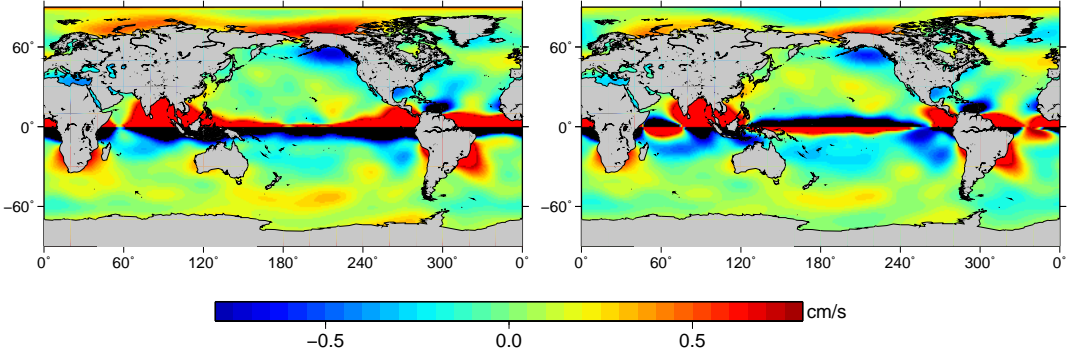


Figure 3.9: Global maps of eastward geostrophic flow from GRACE (GRGS). The left picture depicts the solution obtained by the degree method, the right picture shows the same field obtained using the order method. Smoothing radius used is 800 km.

The two methods results in similar output at higher latitudes. Figure 3.9 shows to global maps of the eastward velocity. As can be seen is that the degree methods is showing some stronger features at higher latitudes than the order method. The most likely cause of the difference is that the degree method uses a different amount of coefficients for a certain truncation degree l_{max} . As the degree method needs coefficients of degree $l_{max} + 1$ to calculate the geostrophic flow the order method only uses coefficients up to l_{max} . Thus for a solution of up to degree 49 the degree method also uses coefficients $C_{50,m}$ for $m = 0 \dots 50$ whereas the order method ignores those coefficients. It was assumed that the increase of the features using the degree method were artifacts. Therefore it was decided to use the order method to calculate the geostrophic flow.

Apparent from the figure is that the strong land hydrological signal from the Amazon basin appears to leak in the Atlantic and Pacific, which causes unrealistic large values for the geostrophic flows. A singularity occurs at the equator where the Coriolis force becomes zero and the geostrophic assumption loses its validity. Close to the equator the two methods differ considerably but what is causing this remains yet unclear.

Chapter 4

Bottom Pressure Recorder Analysis and Placement

This chapter describes the characteristics and processing methodology of bottom pressure recorder data. Furthermore it elaborates on the specific regions of deployments of the used records.

These recorders are deployed on the ocean floor where they record the absolute pressure, induced by the weight of the oceanic and atmospheric column above. Fluctuations in the mass of those columns represent redistribution of mass in the ocean and atmosphere. These redistributions are inherently linked to massive energy transport over the globe and consequently influence our climate. The study of ocean bottom pressure is therefore an important subject in Earth research.

BPRs measure the pressure at a certain point, in contrast to GRACE which is only capable of estimating averages at scales of several hundred km. However, it is still useful to make the comparison. Bottom pressure records are sparse in time and space but provide valuable and independent information on oceanic phenomena. Because of the limited resolution of GRACE this study will focus on large scale features. When those large scale phenomena also have a prominent effect on the local measurements important information can be retrieved about for example seasonal variations of ocean bottom pressure.

The first section describes the pros and cons of the used bottom pressure recorders. In the second section some characteristics of the regions of deployments are clarified. The raw data processing techniques applied are elaborated in section 4.3. In which also a tidal comparison with the FES2004 model is provided.

4.1 Features of Bottom Pressure Recorders

4.1.1 Instrument

The bottom pressure recorders used in this thesis are equipped with a Paroscientific Digiquartz® sensor. Nowadays, this sensor is commonly applied in the oceanographic community because of its good performance. However, it is important to get familiar with the shortcomings of this instrument to value its uses.

First of all the pressure sensor is placed in a hostile and isolated environment exposing it to extreme pressures and salty water. This requires the casing of the sensor to be robust and durable. Typical pressures of 300 to 600 bar occur for placements on the deep ocean floor.

The absolute accuracy of a pressure measurement accounts to 0.01% which then translates to approximately 0.5 m of equivalent water height. As a consequence the absolute values of the pressure are rather useless for our applications. However the noise level of the measurements are in general much better for those situations. Noise levels of 0.15 ppm are common [13] and translate to noise levels of 0.5-1 mm. Therefore the variation of the pressure series can provide us with important information.

Secondly the bottom pressure recorder data displays drifts. Instrumental related drifts originate from the temperature dependency of the pressure sensor, creep associated with high stresses and changes in the internal calibration pressure chamber of the instrument. Furthermore, drifts may occur through non-instrumental effects like the slow adjustment of the BPR to the soft sea floor [13]. Finally, drifts may occur through natural phenomena. Considering the above, it is impossible to distinguish between instrumental drifts and natural phenomena. The observed long term trends in the instrument data must therefore be treated with caution.

The used records are corrected for the drifts by fitting an exponential term and a linear term to the series and then subtracting it from the original series [13]. As a consequence real signals might be filtered out. The dependency by temperature is largely accounted for by using data from the temperature sensor integrated in the pressure sensor. The temperature and drift corrections were applied in an early stage of the processing and therefore the records as provided by Proudman Oceanographic Laboratory (POL) and Alfred Wegener Institute (AWI) were already corrected for this.

Additionally, the clock in the instrument shows a drift in time. The time interval of the measurements is usually calibrated by measuring the time of deployment and recovery with an independent clock and recalculating the interval. When a battery failure occurs this cannot be done however. Time drifts can go up to several minutes per year. In this thesis we only work with monthly averages and those time drifts have virtually no influence on the results.

4.1.2 Bottom Pressure and Geostrophic Flow

The above subsection implies that we can use the bottom pressure recorders to monitor changes in pressure during the observation period. These pressure variations are directly related to the change of mass in the water and atmospheric column overlying the BPR. The largest part of this change is due to ocean tides. On monthly scales these tides are unwanted and have to be removed from the pressure records. Furthermore, since GRACE measures monthly averages, the local time series are averaged according to the GRACE observation periods. The removal of tides and averaging is illustrated in section 4.3. After processing, the residual signal reflects variations in mass with periods longer than two months, equivalent to the Nyquist wave length of the GRACE sampling. Seasonal signals play an important role here but also other signals related to the variation of ocean circulation.

Another interesting feature can be exploited when two or more BPRs are positioned close to each other. Their pressure differences represent the mean geostrophic flow in between. As mentioned before the absolute pressures are highly inaccurate, but the variations can be used. Thus the time series can be used to retrieve mean *variations* in geostrophic flow. Equation 3.24 can accordingly be adapted to yield the mean vertically averaged transport, $\delta\bar{V}$:

$$\delta\bar{V} = \left| \frac{H}{\rho_w f} (\delta p_2 - \delta p_1) (\vec{e}_z \times \vec{e}_{1,2}) \right| \quad (4.1)$$

with $f = 2\Omega \sin \theta$

Here H is the vertical scale height commonly chosen as the depth of the ocean. The change

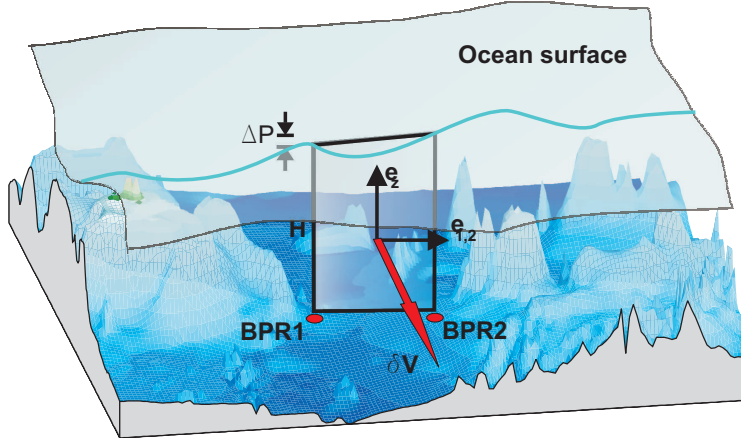


Figure 4.1: Schematic representation of the mean vertically averaged flow in between two BPR stations. Heights are not to scale. Situation depicted is for a location on the southern hemisphere.

in pressure at station 1 and 2 is denoted by δp_2 and δp_1 respectively. The unit vector \vec{e}_z points in the zenith direction and the vector $\vec{e}_{1,2}$ connects the two stations. The transport is bounded by a square perpendicular to the line connecting the stations as can be seen from figure 4.1.

4.2 Regions of BPR Placements

The regions where the BPRs are deployed must be chosen carefully. The location must suit the goal of the BPRs. Two general effects play an important role in this study. The first effect, contamination by tides, is largest when using shallow moorings, since in the shallow oceans tidal amplitudes are larger and more complicated. Secondly, for a good comparison one needs BPRs placed far away from land to prevent gravitational signals originating from land to leak in the GRACE solution during the smoothing process.

The DART (Deep-ocean Assessment and Reporting of Tsunamis) uses bottom pressure recorders at locations close to undersea tectonic margins to detect tsunamis in near real time. The placement of the moorings are in general in deep water. However, for this study, DART sensors are of lesser use. This is because the sensors are generally placed close to land and some of them contain large jumps in the data. In particular many DART moorings are positioned close to the Aleutian trench. This placement is strategical since tsunamis originating from the trench can be detected in an early stage before they reach the east coast of the United States. However strong seasonal land signals from Alaska (snow and ice accumulation) are likely to contaminate the GRACE ocean signals and consequently prohibit a proper comparison. In the first phase of this project an investigation has been made to what extent the annual signals of GRACE corresponded to the annual signals obtained from the DART moorings. The best result is plotted in figure 4.2, where the annual signal of GRACE (CSR release 1) shows a good agreement with that of the DART data. The results differed considerably among the available locations and the raw data needed much fixing and shifting to make some sense. Hence the DART analysis was abandoned when better data became available. Currently, the DART data sets have increased and more recent GRACE data is available, making it an interesting subject for future research.

In this thesis we emphasize on data from the Southern ocean. The Southern ocean is

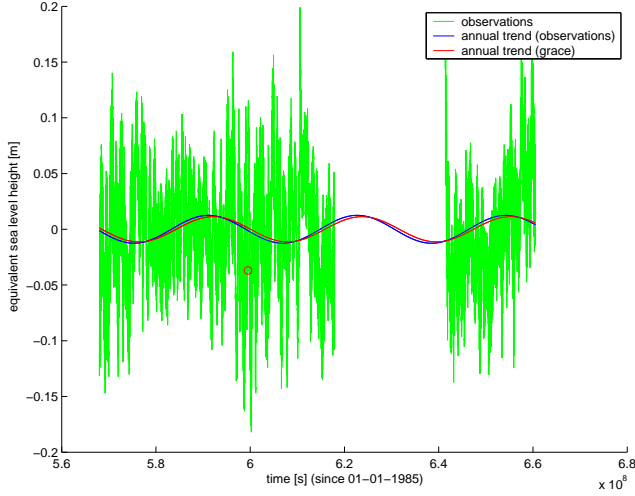


Figure 4.2: Dart data with annual sines from the local data (green) and from GRACE (CSR RL01). Averages of the three DART data segments are removed. The mooring is located in the east of the equatorial Pacific.

Absolute Dynamic Topography 3–3–2004.

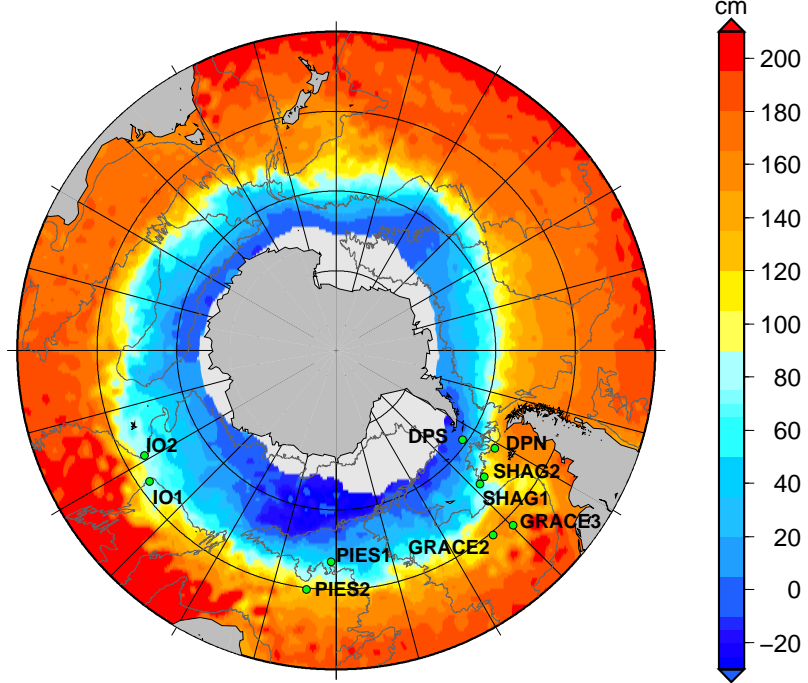


Figure 4.3: AVISO gridded absolute dynamic topography around Antarctica on the 3rd of March 2004. The steep concentric fronts illustrate the presence of the ACC. Superimposed are the bathymetric contours and the positions of the BPR deployments. Absolute dynamic topography is derived from multiple satellites.

characterized by the presence of a strong barotropic front causing the Antarctic Circumpolar Current (ACC) to circle the continent. This can be best visualized using altimetry data. Altimetry serves as a powerful tool to calculate *absolute* geostrophic flows close to the surface.

A measure of these flows is given by the absolute dynamic topography, the sea level height above the static geoid. Steep surfaces in the absolute dynamic topography represent strong geostrophic currents along the constant height lines.

| Name: | Location | period | Depth [m] | nr. of Channels |
|------------------|----------------|--------------------------|-----------|-----------------|
| IO1 | 47.1°S 54.9°E | jan 04 - feb 05 | 3944 | 2 |
| IO2 | 48.8°S 61.3°E | jan 04 - jan 05 | 3925 | 2 |
| PIES1 | 50.3°S 1.4°E | nov 02 - jan 05 | 3897 | 1 |
| PIES2 | 44.7°S 7.1°E | nov 02 - jan 05 | 4619 | 1 |
| SHAG1 | 53.1°S 312.9°E | apr 03 - nov 04 | 1504 | 1 |
| SHAG2 | 53.4°S 310.5°E | apr 03 - nov 04 | 1510 | 1 |
| GRACE2 | 43.2°S 314.7°E | may 02 - may 03 | 5114 | 2 |
| GRACE3 | 44.4°S 319.6°E | may 02 - may 03 | 5141 | 2 |
| DPN ^a | 54.9°S 301.6°E | oct 03 - dec 04 - dec 05 | 1148/1090 | 1/3 |
| DPS ^a | 60.9°S 305.3°E | dec 02 - dec 04 - dec 05 | 1000/1090 | 3/1 |

Table 4.1: BPR locations, depths and observation periods.

^aTwo separate deployments

The presence of the ACC can be seen from figure 4.3. The figure shows that all around Antarctica a strong front is present which shows a height difference of more than 1.5 m. The dominant part of the ACC is barotropic [23] and therefore large barotropic fluctuations can be expected. The ACC is likely to cause a large scale signal in the GRACE solution and is therefore an interesting subject of study. It is for the reasons above that the pressure data from the indicated BPRs are selected. The used BPR records are summarized in table 4.1. The PIES data is obtained from the Alfred Wegener Institute in Germany, the IO data is deployed on behalf of IFREMER and Proudman Oceanographic Laboratory (POL), the other data are all deployed by POL.

4.2.1 South Atlantic and Indian Ocean

The ocean south of Africa is considered a dynamic region. North of the Crozet and the Kerguelen Islands the Albulhas Return Front (ARF) the Subtropical Front (STF) and the Subantarctic front (SAF) merge as they are strongly steered by the bottom topography (see for example [35] and [42])). The intensification, due to topographic steering, of the fronts north of the islands can be seen from Fig. 4.4. In this figure the absolute dynamic topography (AVISO) is plotted but for the subregion around south Africa. One recognizes the above mentioned merging of the fronts north of the islands, which is associated with the majority of the Antarctic Circumpolar Current (ACC) mass flow. According to Park [34] 80% of the total ACC transport flows through the gap in between Kerguelen and the Amsterdam island. Another weaker front, the polar front (PF), is positioned south of Crozet and is highly variable both in position and strength [42]. The front is more concentrated in the western part of the South Atlantic and less obvious close to the Kerguelen plateau.

The presence of the Kerguelen plateau seems to have a strong influence on the circulation in the Southern ocean as it acts as an efficient barrier. The plateau separates two subpolar gyres observed by altimetry [33]. Furthermore, large scale wind curl around the Kerguelen plateau might cause an Ekman flow onto the plateau [31]. Additionally, the plateau causes the ACC to be deflected to its most northern position around Antarctica, the passage between Kerguelen and the Amsterdam Islands.

Moreover, there are indications of interesting deep circulations patterns in this region.

Park [35] suggested that through the passage between Crozet and Kerguelen a deep western boundary current is flowing northwards, as traces of Antarctic Bottom Water (AABW) were found in the Crozet basin. These observations are consistent with sections from the Conrad expedition [24] that showed the presence of AABW midway between Crozet and Kerguelen.

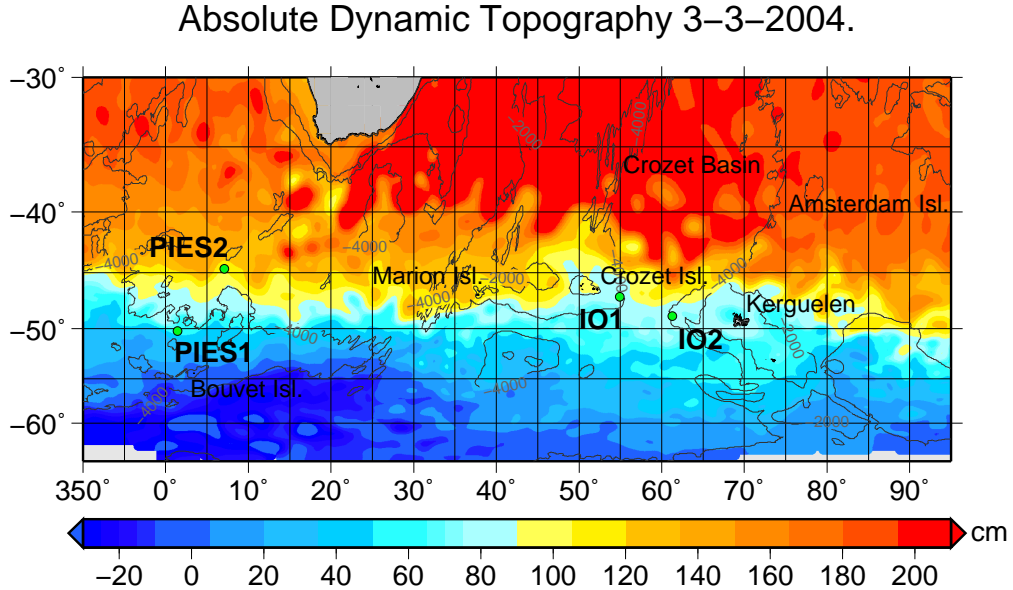


Figure 4.4: AVISO gridded absolute dynamic topography around Kerguelen on the 3rd of March 2004. Superimposed are the bathymetric contours and the positions of the BPR deployments. Absolute dynamic topography is derived from multiple satellites.

The recorders IO1 and IO2 were deployed on each side of the saddle point in between the Crozet plateau and the Kerguelen plateau as to monitor the flow in between. The PIES (Pressure inverted echo sounders)1 and 2 recorders were also aligned such that they were able to efficiently monitor variations of the ACC.

4.2.2 Drake Passage and Argentine Basin

The Drake passage in between south America and Antarctica is a major bottleneck for the ACC. West of the Drake passage the ACC fronts merge before entering the South Atlantic. East of the passage the fronts separate to adapt to the irregular bottom topography.

The most northern front, the Subantarctic front, bends northwards after the passage following the bathymetric contours. After traveling northwards the SAF bends sharply southward again to meet with the Polar front again (see figure 4.6). Both the SAF and PF must cross the North Scotia ridge. A potential crossing point is Shag Rocks passage [2]. On each side of this passage the bottom recorders SHAG1 and SHAG2 were deployed, which can be seen from figure 4.5. Also apparent from this figure is the colliding between the Falkland current, fed for a large part by the ACC and the Brazil current at approximately 40 degrees south. Some phenomena in the Argentine basin are therefore connected to those of the ACC. Moreover, there is an abyssal circulation in the Argentine basin with water originating from the Weddell sea [40].

Recently, bottom pressure records in the Argentine basin showed several significant pressure fluctuations [22]. In particular, the records were dominated by a 20 day mode with

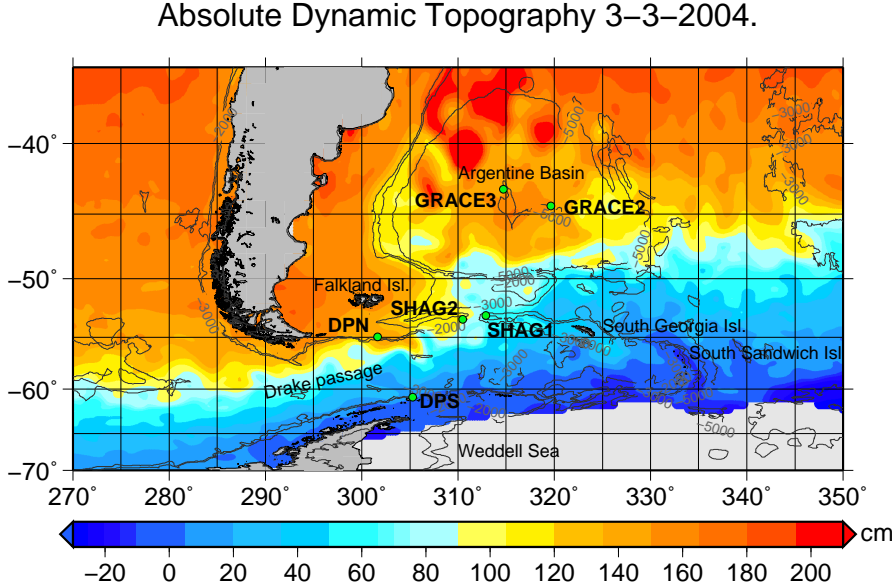


Figure 4.5: AVISO gridded absolute dynamic topography through the Drake Passage on the 3rd of March 2004. Superimposed are the bathymetric contours and the positions of the BPR deployments. Absolute dynamic topography is derived from multiple satellites.

amplitudes up to 15 cm equivalent water height. A similar mode was picked up by analysis of altimetry in the region [17]. The existence of this phenomena can be attributed to the shape of the basin, which is also explained from theory and modeling [17]. The frequency of this mode is too high to be properly detected by GRACE. However, the comparison with GRACE is still performed to investigate other phenomena. The averaging process, applied to the pressure records, removes a large component of this variation as will be illustrated later. These records are denoted GRACE2 and GRACE3 in this thesis. This naming convention derives from the original purpose of the BPRs, the validation of the oceanic component of the GRACE mission.

The BPRs DPN and DPS are positioned north and south of the Drake passage. These positions enable monitoring of nearly the complete transport of the ACC, as the majority of the transport flows in between. The records were recovered and deployed twice. Unfortunately some of the records at the DPS location suffered from high noise levels and some unexplainable jumps.

4.3 Data Processing

The records from the BPRs contain tides. Generally these tides have amplitudes larger than the signal of interest. Therefore in this study the tides are removed using a harmonic tidal analysis [15, 39]. The harmonic analysis method is applied since correcting with the FES2004 model still showed significant tidal energy in the local records. Furthermore it provides the opportunity to compare the FES2004 model with in situ estimates for the tide. After the harmonic analysis the data are averaged to make them equivalent to the monthly GRACE solutions. This section also provides a spectral analysis of the processed series to study the remaining tidal signal and investigate the presence of non-tidal high frequency phenomena.

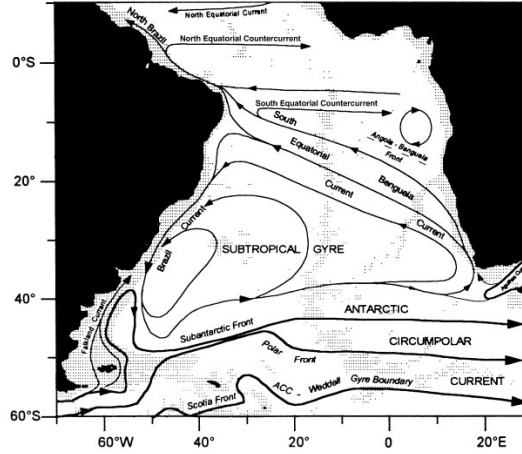


Figure 4.6: Current system in the South Atlantic. After Peterson and Stramma [36].

4.3.1 Tidal Analysis

The bottom pressure series contain tidal effects and non-tidal effects. The tidal contribution and a drift term are modeled as $P_{tide}(t)$:

$$P_{tide}(t) = C_0 t + \sum_{i=1}^n C_i \cos 2\pi\omega_i t + S_i \sin 2\pi\omega_i t \quad (4.2)$$

Here C_i and S_i are the cosine and sine amplitude corresponding to the tidal constituent with discrete frequency ω_i . The time, t , is with respect to the center time of the BPR record. In general the amount of BPR measurements is much larger than the amount of unknowns C_i and S_i . When replacing $P_{tide}(t)$ with the observations of the BPR (minus the average), we get an overdetermined system $A\mathbf{x} = \mathbf{y}$:

$$A = \begin{bmatrix} t_1 & \cos 2\pi\omega_1 t_1 & \cdots & \cos 2\pi\omega_n t_1 & \sin 2\pi\omega_1 t_1 & \cdots & \sin 2\pi\omega_n t_1 \\ \vdots & \vdots & & \vdots & \vdots & & \vdots \\ t_k & \cos 2\pi\omega_1 t_k & \cdots & \cos 2\pi\omega_n t_k & \sin 2\pi\omega_1 t_k & \cdots & \sin 2\pi\omega_n t_k \end{bmatrix}$$

$$\mathbf{x} = \begin{bmatrix} C_0 \\ \vdots \\ C_n \\ S_1 \\ \vdots \\ S_n \end{bmatrix} \quad \mathbf{y} = \begin{bmatrix} P_1 \\ \vdots \\ P_k \end{bmatrix}$$

The observation at time t_i are denoted by P_i . The least squares method is used to estimate the unknown vector \mathbf{x} .

$$\hat{\mathbf{x}} = (A^T Q A)^{-1} A^T Q \mathbf{y} \quad (4.3)$$

The observation covariance matrix, Q , is approximated by a purely diagonal matrix in this thesis. All BPR measurements are assumed to have a Gaussian noise with a standard deviation of 0.5 mm, as discussed earlier. The uncalibrated errors of the estimated coefficients are given by the diagonal of the normal matrix $(A^T Q A)^{-1}$. Under these assumptions the least squares estimate involves the calculation of the inverse of $(A^T A)$. It can be shown that this matrix is positive definite and therefore can be decomposed by the Cholesky method.



In contrast to using Gaussian elimination, the Cholesky decomposition enables an efficient way to invert the matrix and reduces the accumulation of rounding errors in the inversion. General routines from the fortran LAPACK library were used.

The most important tidal constituents are the semi-diurnal and diurnal tides. Other constituents (up to 46) are fitted but have less influence. The calculated constituents are now used to construct an estimate of $P_{tide}(t)$ which can be subtracted from the original series to obtain the tidally corrected series. In this study annual and semi-annual constituents are kept in the series as they are expected to be caused predominantly by seasonal variations instead of by tidal forcing. These signals must also be present in the GRACE solutions and must be considered for a realistic comparison. No attempt to model these long period tides has been made. The observed amplitudes of the annual and semi annual signals are several cm, which is an order of magnitude larger than the equilibrium long period tides.

To distinguish constituents with neighbouring frequencies a record length of more than 18.6 years is needed. Unfortunately, the available data has much shorter lengths. Therefore only the main constituents which show sufficient separation of their spectral lines¹ are fitted to the series [15]. Now when one assumes a fixed amplitude ratio of the fitted components to their smaller neighbours, one can apply a so called nodal correction to the fitted amplitudes and phases [39]. In this thesis this correction is obtained by using the amplitude ratios of the equilibrium tides tabulated in [39].

4.3.2 Tidal Analysis Results

Although the tidal removal program was initially not intended to accurately estimate tidal constituents, the output can still be used to compare the tides with that of the FES2004 tide model. As the FES2004 model is used in both the GRGS and GFZ solution errors in the FES2004 model cause tidal aliasing in the GRACE solution. It is therefore interesting to compare the local FES2004 constituents with those estimated from in situ measurements. The amplitudes of the main constituents of FES2004 and the corresponding ones of the BPRs are shown in figure 4.7. The calculated Greenwich phases show strong differences, however this is most likely due to a reference system issue yet unsolved for by the program². Hence, no conclusions will be drawn from the phase analysis.

From figure 4.7 it can be seen that especially the bottom pressure records in the Drake Passage show large differences in the modeled and calculated amplitudes. Therefore, it is expected that the GRACE solution at those positions contain a large amount of aliased tidal signal. Furthermore, The BPRs IO1 and IO2 near Crozet and the Kerguelen show the smallest overall amplitudes in tides. The PIES BPRs are mainly dominated by semi-diurnal tides. And the GRACE and SHAG records show a similar distribution of the diurnal and semi-diurnal tides. The monthly tide of GRACE3 shows a large error presumably because of leakage of the 20 day mode discussed earlier. Except for the IO records and PIES2 record all locations show some errors larger than 2 cm.

4.3.3 Spectral Analysis

It is interesting to investigate to what extend the remaining series contains high frequency phenomena and noise. In order to do this a power spectral density estimate of the series was made. The method to calculate the power spectral density is somewhat out of scope of this project and is therefore only roughly described. Interested readers are referred to references

¹When constituents differ in the first three digits of the Doodson number

²Unresolved phase shifts of $\frac{1}{4}$, $\frac{3}{4}$, $\frac{1}{2}$ cycles depending on the semidiurnal, diurnal and terdiurnal nature of the constituents [15]

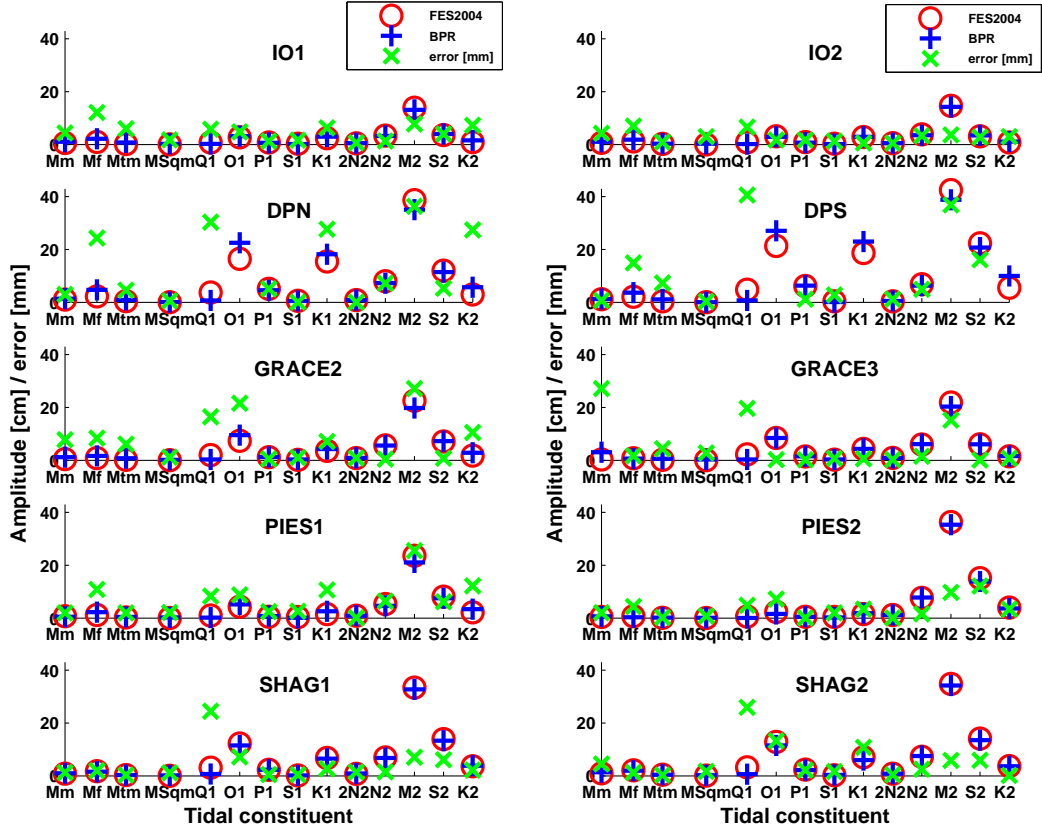


Figure 4.7: Amplitudes of the FES2004 model (red circles) and local bottom pressure records (blue crosses) for the 10 analyzed stations. The difference between the amplitudes, in mm, is denoted by the green x marks.

[53, 18, 12] for an elaborate discussion of this topic.

The power spectral density is estimated using the Welch method [53]. The idea behind this method is to split up the total record in segments, which are allowed to overlap. The fast Fourier transform is then calculated for each segment and squared. The power spectral density is obtained by averaging the segments.

In this study each record is split up in eight segments which overlap by 50%. Furthermore, the data of the segments are weighted with a Hanning window to diminish the effect of the abrupt edges. The fast Fourier transform (FFT) is calculated using the FFTW library [16]. However, the data series possibly contain gaps and intervals are not always evenly distributed³, which is a requirement for the FFT algorithm. Therefore the series is first converted to an equi-spaced time grid, before they are fed in the FFT routine.

To accomplish this gridding one could interpolate values to the missing points, but this would yield non-realistic values when the gaps are too large. A more advanced method is to use Gaussian gridding [18, 12]. The data points of the original series are convolved with a Gaussian kernel. Consequently, the data points are smeared out over their neighboring equi-spaced points, which are denser distributed. A given data point will have a negligible effect on distant points and therefore only the 24 closest grid points are selected. The

³The routine has been originally designed to cope with irregular Dart data.

Gaussian kernel parameter must be adjusted accordingly to minimize the error caused by the above truncation. Figure 4.8 shows the gridding process graphically. The method causes the original data to be smoothed somewhat but this is only favorable since it partly removes noise from the observations.

Once the FFT of the equi-spaced set has been calculated it must be deconvolved back to obtain an estimate for the Fourier transform of the original data.

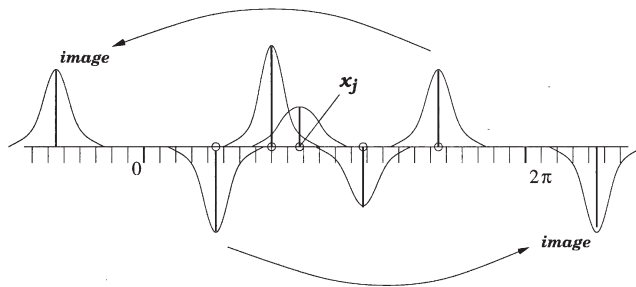


Figure 4.8: Gaussian gridding for non-equispaced data. Circles represent data points and small lines along the axis the equi-spaced grid points. Data is assumed to be periodic outside the domain. Taken from Greengard and Lee [18].

4.3.4 Spectral Analysis Results

In this section the main outcomes of the spectral analysis are discussed. Power spectral density plots for the BPRs and some of their channels are provided in appendix D.

The first observation which can be made is that there is remaining tidal power present. In particular the Drake passage BPRs shows large peaks at the tidal frequencies. This comes as no surprise since figure 4.7 shows the largest tidal amplitudes for the Drake passage, as a consequence larger errors can be expected.

Furthermore, as was already discussed earlier, the records in the Argentine basin show large amplitudes for 20 day periods [22]. A similar but weaker feature can be observed in the IO1 series.

The PIES sensors show a strong feature with a period of about three days. Since the piezoelectric BPRs have sample frequency of once every hour the spectrum is cut off at a lower frequency.

As can be observed the records from the Shags Rock passage contain a relatively high power in the high frequency part of the spectrum. This can indicate instrument noise or high frequency physical phenomena. Some of the Drake BPR channels contain similar shapes (not plotted) and it is therefore most likely that it can be attributed to measurement noise. As both the SHAGEX and Drake BPRs are positioned in relatively shallow water, measured temperature fluctuates more strongly than their deeper counterparts. The temperature corrections applied to counteract the temperature dependency of the sensor might therefore be larger and consequently contain larger errors.

4.3.5 Averaging Methodology

Some of the tidal and high frequency signals left in the records and will be further reduced by the averaging procedure. As the GRACE solutions are considered as monthly means, the BPR series must be averaged according to their GRACE equivalent. For the

case of CSR/GFZ GRACE solutions these corresponds to plain monthly averages. When comparing with the GRGS-GRACE solution a weighted average of the BPR observations is constructed. The weights are 0.5/1/0.5 for three consecutive 10 day intervals centered on the mean observation date of the GRACE solution. As the weights of the outer parts of interval are decreased, the temporal resolution should increase somewhat. However, the resulting averaged series show a correlation in time just as their GRGS counterparts.

Chapter 5

GRACE Validation with Bottom Pressure Recorders

This section presents the results of the comparison of GRACE estimates of ocean bottom pressure and geostrophic velocity with their BPR equivalent. Two important comparison criteria are the correlation and signal to noise ratio elaborated in the next section.

Section 5.2 is concerned with the validation of the GRACE striation filter against the in situ records. Then, sections 5.3 and 5.4 elaborate on the validation of bottom pressure and geostrophic flow respectively. Since GRACE measures spatial averages, an investigation of how the BPR series correlate with the GRACE solution in their surroundings serves as a valuable addition.

5.1 Correlation and Signal to Noise Ratio

The correlation gives an indication of how similar two series behave. It is not a necessary condition that the two series share the same units. The correlation coefficient is used to see how strong a *linear* relation between two observables is and obtains values between -1 and 1, where higher values reflect synchronous behavior. Bearing this in mind one could for example try to find whether there is a correlation between birthrates and successful football matches nine months earlier. The correlation, ρ_{XY} , for two observables, X and Y , with standard deviations σ_X and σ_Y , is expressed as:

$$\rho_{XY} = \frac{\text{cov}(X, Y)}{\sigma_X \sigma_Y} \quad (5.1)$$

In this study the two observables represent the same quantity, and the linear relation is automatically satisfied. However, variances of the observables have no influence on the correlation coefficient since it is a dimensionless quantity. An additional test is therefore required to compare the magnitude of the variations. This can be done with the approximate signal to noise ratio (SNR).

$$SNR_{XY} = \frac{\sum_i X_i^2}{\sum_i (X_i - Y_i)^2} \quad (5.2)$$

When both observables show small discrepancies and display similar variations SBR_{XY} and SNR_{YX} will be larger than 1.

The root mean squared of the differences between the series can be viewed as an approximate error of the GRACE estimate. For N data points this yields:

$$RMS_{diff} = \sqrt{\frac{\sum_i (X_i - Y_i)^2}{N}} \quad (5.3)$$

An inherent problem of the comparison between GRACE and the local measurements is that the amount of data points is very limited. For a one year BPR record only 12 GRACE solutions are available from the CSR and GFZ centers and about 35 for the GRGS solution. The estimation of the correlation coefficient and the SNR is thus very sensitive for outliers in the data. A visual inspection of the series is therefore a necessary addition to its interpretation.

The GRACE data might still display trends originating from sources as post glacial rebound. Furthermore, inter-annual variability possibly emerges as an apparent trend in the relatively short observation periods. The de-trending of the BPR records removes physical secular trends. To guarantee consistency with the records, all trends over the observation period of the BPR must be removed from the GRACE series.

A final note on the correlation coefficient must be made. To establish whether there is any statistical relevance of the calculated coefficient the lower 95 % confidence bound is calculated. The procedure to calculate these bounds is the percentile method which uses bootstrapped samples of the original sets [3]. This method gives more realistic results for the small sample sizes considered.

5.2 Validation of the GRACE Post-Processing Filter

As described in section 3.4.2 a post-processing filter may be applied to the GRACE spherical harmonic coefficients to reduce the striations present in the time variable geoids. The procedure has been validated against a surface mass distribution model [44]. However since the processing methodology is not based on a physically justified method, there is a chance that physical phenomena in the solution are reduced. It is therefore interesting to validate this method against local observations. Furthermore the filtering method has not yet been applied and tailor made to the GRGS solution, which contains only coefficients up to degree 50.

In this thesis we apply the filtering method as described by [5]. The applied method is to fit a polynomial of degree p to the correlated coefficients. Then, under the assumption that it is of non-physical origin, the polynomial is subtracted from the coefficients.

For the CSR and GFZ solution a 7th degree polynomial has been fitted to coefficients which have orders larger than 8 up to 80, the values were adopted from [5]. The GRGS coefficients are fitted with a 6th degree polynomial for orders 8 up to 36. The chosen values were based on trial and error such that the striations in the mapped fields were more or less acceptable. The maximum degree was cut off at 36 since from that degree the influence of the static gravity field, constraining the GRACE solution, becomes significant. Higher degree coefficients show no correlations and should therefore not be incorporated in the filtering method.

The filter is validated against the BPR measurements which showed positive correlations with GRACE for larger smoothing radii. Figure 5.1 shows the improvement in correlation when applying the filter.

The figure shows a particular improvement in correlation for lower smoothing radii. Some negative values are present but they occur for smoothing radii under 600 km for the GRGS

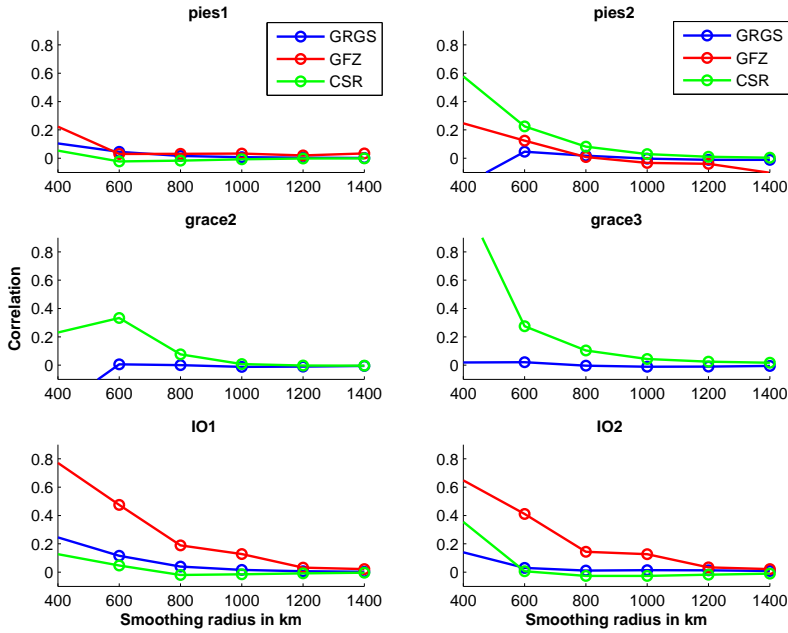


Figure 5.1: Improvement in correlation when using the striation filter. Positive values indicate the increase of correlation when applying the filter. The GFZ solution for the grace records are omitted since only three GFZ solutions were available in the observation period.

solution. Smoothing values under 600 km are of lesser importance as they are under the resolution of the original GRGS sets.

From the above discussion we can conclude that it is advantageous to implement the filter for smoothing radii lower than 800 km. In particular the CSR and GFZ solutions benefit from applying it. The GRGS solutions also show some improvement for lower smoothing radii. The GRACE estimates in subsequent discussions will therefore be filtered unless mentioned otherwise.

5.3 Results of the Bottom Pressure Comparison

Here the results of the bottom pressure comparison are presented. Two types of series are constructed from the BPR records. The measurements for each location and the average at the midpoint of the BPR pairs. Since the spatial resolution of GRACE is large compared to the point observations of the BPRs, the averages of the in situ recorders are a good indication of a spatial mean and thus are included in the analysis. Averages are obtained by taking the time interval where both recorders share measurements and then use a linear interpolation to shift both series to the same time tags. This procedure is performed before averaging the series to their GRACE equivalent.

In appendix A tables for the best correlations are provided for three different smoothing radii and for the computing centers considered. The comparison based on the correlations for each specific region is elaborated below. Time series in this chapter are only shown for the GRGS solution as it shows more details due to the higher temporal resolution. The time series for the GFZ and CSR solutions can be found in appendix B.

5.3.1 Crozet Kerguelen Region

From the tables in appendix A one can find that the BPRs denoted by IO1 and IO2 are strongly correlated with the GRACE solution. Correlations larger than 0.6 are found for all three GRACE solutions. The best correlations of up to 0.9 are found for the average of the two BPRs. When excluding the first month the series show a better agreement. This is probably caused by remaining initial drift in the BPRs. Such a phenomena is not uncommon for bottom pressure recorders deployed in the deep ocean [49].

The first part of the series in figure 5.2 shows a discrepancy in the first month. Overall, it displays similar signatures for both the GRACE and the in situ observations.

The fluctuations of the CSR solutions appear to overestimate the true variation. Compared to the local series and GRACE the standard deviations for the CSR solution are large. The larger fluctuations of the CSR solution can probably be attributed to the lower accuracy of the used release 1 product. A closer look in the figures of appendix B shows that the CSR solution also displays larger fluctuations at other locations. Fluctuations such as those are most likely related to anomalous large values of the C_{20} coefficient found in the release 1 products. This problem has been largely solved in later releases.

The correlations and the figures show that GRACE improves the estimate from the de-aliasing product. GRACE is showing larger and more realistic fluctuations in time than the models alone. Apparently, the phenomena not captured by the barotropic ocean model and atmospheric ECMWF fields are observed by GRACE. It is unlikely that those phenomena are of baroclinic origin as the measured fluctuations are of relatively fast origin.

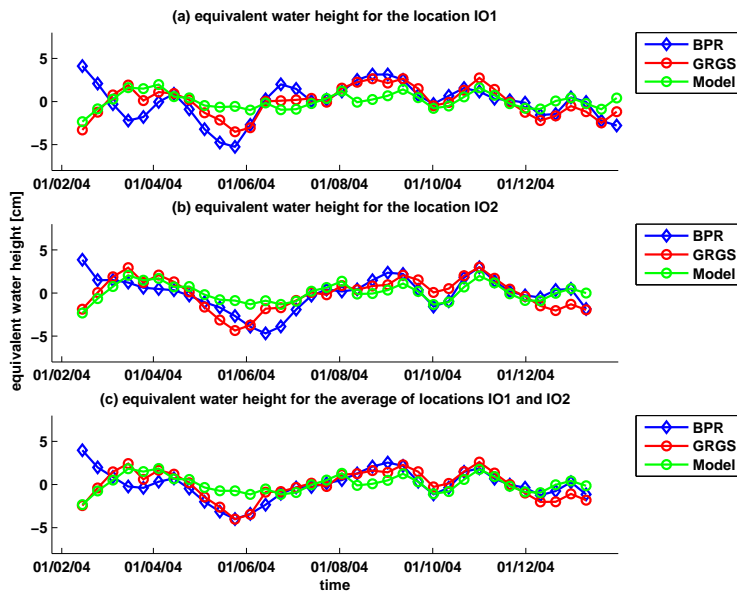


Figure 5.2: Time series of the in situ records near Crozet and GRACE (GRGS). Also shown are the series for the de-aliasing atmosphere and ocean models. Smoothing radius for grace is 800 km.

Figure 5.3 shows the variation of the correlation versus the smoothing radius. From this figure it appears that the GFZ solution is the least accurate one with some significance levels lower than 0. However when examining the time series the GFZ solution and the local

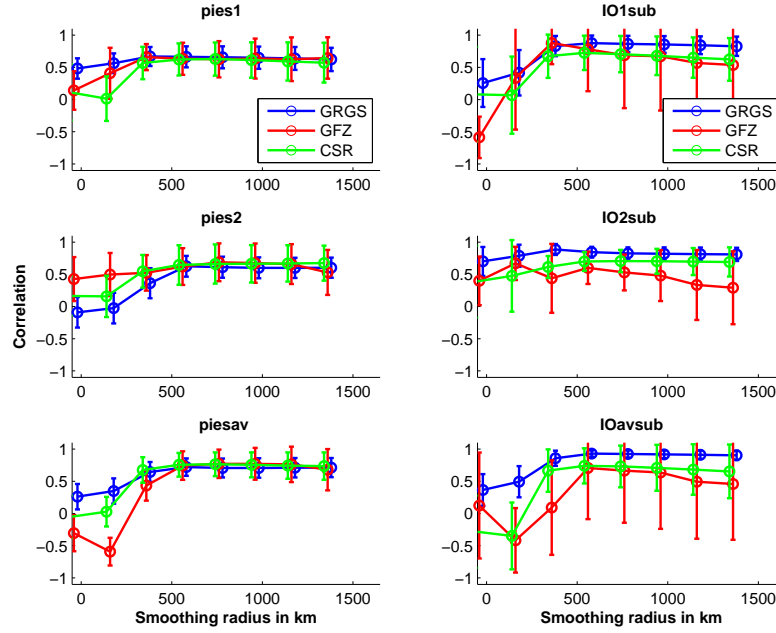


Figure 5.3: Correlation vs. smoothing radius for the PIES and IO recorders. Figures are provided for the local measurements and the average at the midpoint (denoted by ‘av’). The accuracy of the correlation estimates are reflected in the error bars. The prefix ‘sub’ means that the first month from the in situ record is excluded.

records shows some similar signatures. Maximum correlations are obtained for smoothing with a radius around 600 km for all solutions.

The GRGS solution shows the smallest RMS difference of all solutions for the subset of the average of the BPR records this yields a minimal RMS value of 0.7 cm for the most optimal case.

The high signal to noise ratios indicate that GRACE is capturing the real phenomena with good approximation. Most of the SNRs are above 1 suggesting only small discrepancies between the GRACE and in situ series.

It is illustrative to look at how the local measurements are correlated with the GRACE solution at other positions. This might clarify of how and from where unwanted gravity effects leak in the GRACE solution. Furthermore it can identify areas which show a strong interaction. Those interactions will be caused by similar and synchronous signals, possibly of seasonal origin.

Figure 5.4 shows the correlation of the mean of the two local records with GRACE at other locations around Antarctica. The most obvious observation, which can be made, is that in the vicinity of the Crozet and Kerguelen Islands there is a strong agreement with the local observations.

When examining the correlations of the individual locations (appendix C) one sees that two distinct regions east and west of the Kerguelen can be distinguished for the IO2 and IO1 BPRs respectively. Although the BPRs are spaced relatively close together there difference is significant. As we will see later those differences actually cause a high variability of the transport in between. This confirms the earlier observations of strong variability in the region from the previous chapter.

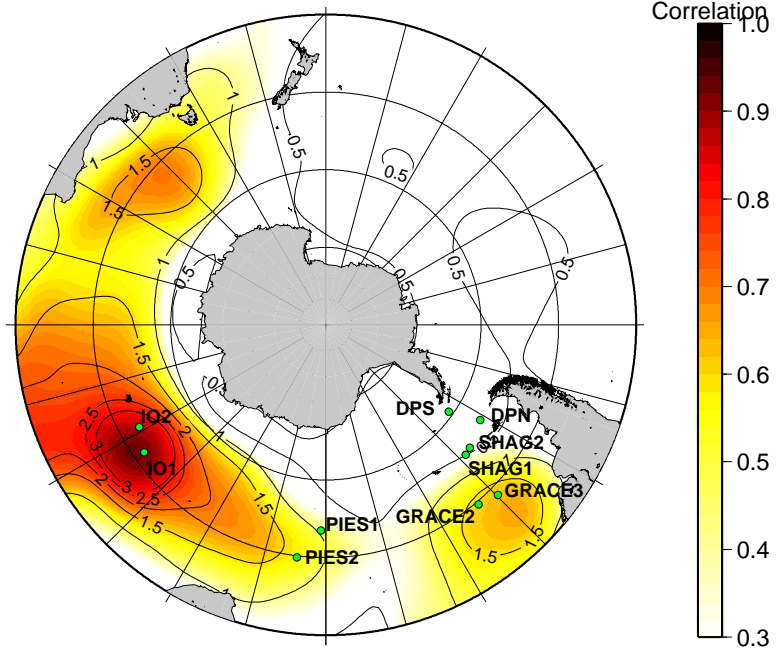


Figure 5.4: Spatial correlation of the mean of IO1 and IO2 with GRACE (GRGS). The smoothing radius of GRACE is 800 km. Signal to noise contours are drawn in black.

Another interesting feature is that there appear to be two regions which show strong correlations with the local Crozet and Kerguelen measurements. One is located south of Australia and one is located right in the Argentine basin. Those regions appear to be strongly linked with the phenomena around the Kerguelen plateau. A brief investigation using a time lag of plus and minus 14 days showed similar but somewhat weaker features.

As mentioned, part of the signal overlies the Kerguelen plateau. Such a large scale signal could correspond to the observation of [31] who suggested that wind curl around the plateau caused Ekman flow onto the Kerguelen plateau increasing the overlying mass. This phenomena occurs for periods between 5 days and a year and thus might be detectable by both GRACE and the BPRs. The variance of the GRACE bottom pressure, spanning from 2002 till 2006, shows three areas of higher variability (figure 5.5). The first area is the Kerguelen plateau, the second one the Argentine basin and there appears to be one west of the Drake passage.

The centers of higher variability from figure 5.5 show a good resemblance with the centers found from altimetry [17]. However from figure 5.6 one observes that the center of the highest variability near the Kerguelen is shifted somewhat to the east compared to GRACE. The disagreement could be due to the fact that the sea surface height variability holds for periods within 20 and 100 days, excluding the annual variability. It is not expected that the steric discrepancy between GRACE and altimetry plays an important role at those latitudes and time scales. The water temperature is lower and the variation is mainly of seasonal origin [38] and thus largely excluded from the discussed altimetry analysis.

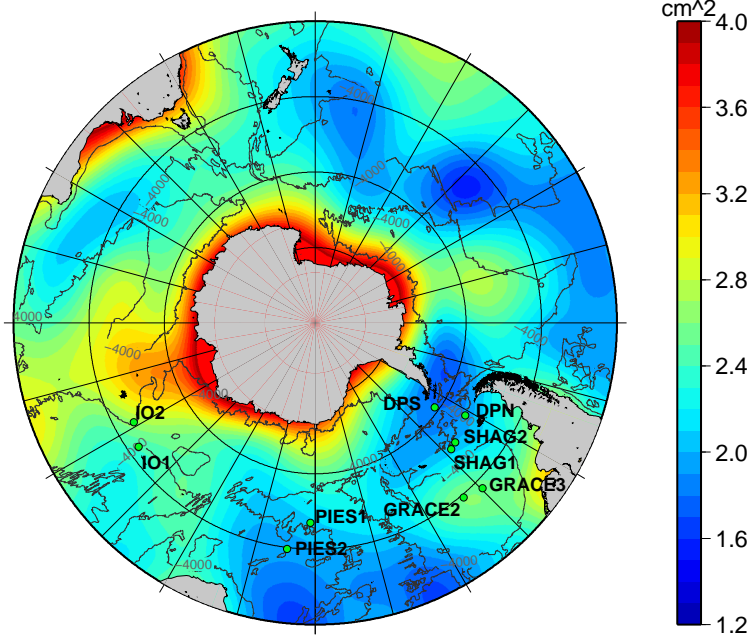


Figure 5.5: Variance of GRACE (GRGS) bottom pressure. The observation period covers 2002 till 2006. Smoothing radius used is 800 km.

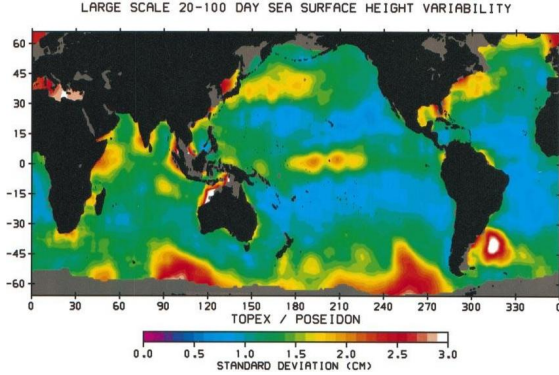


Figure 5.6: Variance of large scale sea surface height from altimetry. Three areas of high variability can be identified in the southern ocean. Taken from [17]

5.3.2 South Atlantic

Here the two BPRs denoted PIES1 and PIES2 are discussed. As the measurement period of the recorders was longer (they measured every hour to save battery time) they yield a better comparison as more data points are shared with GRACE. The accuracy of the correlations benefit from this as can be seen from figure 5.3. The GRGS time series are plotted in figure 5.7. The spatial correlation of the PIES2 recorder with GRACE is plotted in figure 5.8.

The correlations for the South Atlantic pressure recorders are somewhat lower than those

near Crozet and Kerguelen and show values up to 0.6-0.7. The GRGS solution shows smaller fluctuations than the in situ records, which is reflected in the smaller standard deviation of the series and consequently the smaller signal to noise ratios. All GRACE solutions display a more or less consistent correlation for smoothing radii larger than 600 km.

Similar to the comparison in the previous paragraph, one can observe that the correlations with the models decrease compared to those of the GRACE solution, suggesting GRACE is measuring unmodeled phenomena.

Again, from the plotted time series in the appendix it appears that the GFZ solution is again showing a smoother variation of the bottom pressure than the CSR solution.

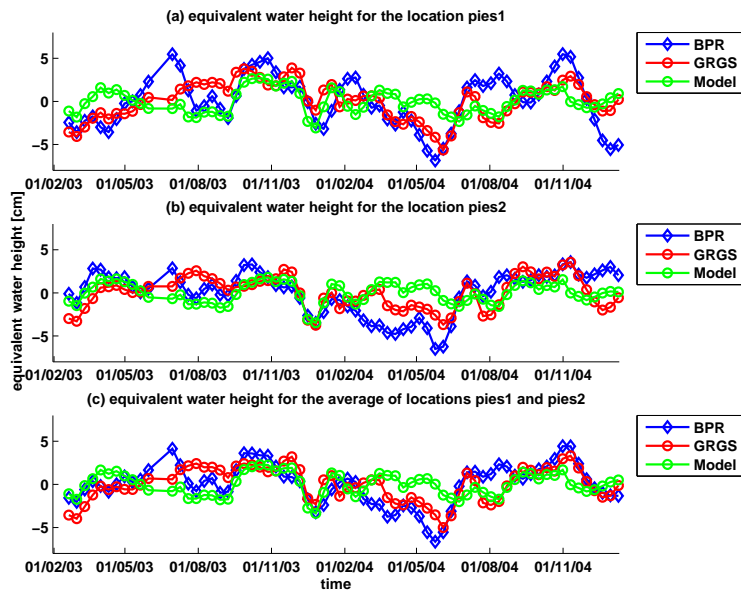


Figure 5.7: Time series of the in situ records in the South Atlantic and GRACE (GRGS). Also shown are the series for the de-aliasing atmosphere and ocean models. Smoothing radius for GRACE is 800 km.

The correlation of the local measurements with GRACE at other locations show that the maximum spatial correlations obtained are less than those of the previous section. The effect is strongest in the vicinity of the PIES stations. This area of higher correlation shows a lobe extending toward the Crozet islands.

Peculiar is that again two regions can be distinguished which show a similar behavior as the local measurements. Those regions are very similar to those found earlier, the first one south of Australia and the other one close the Argentine basin. The centers of maximum correlations are shifted somewhat to the south and south-east respectively with respect to centers found in the previous paragraphs. It is interesting to note that the PIES1 recorder, the most southern one, is showing only significant correlations in its direct surroundings.

5.3.3 Argentine Basin

The BPRs, which were originally deployed for a comparison with GRACE, were positioned at deep locations in the Argentine basin. As discussed earlier the records showed dominating

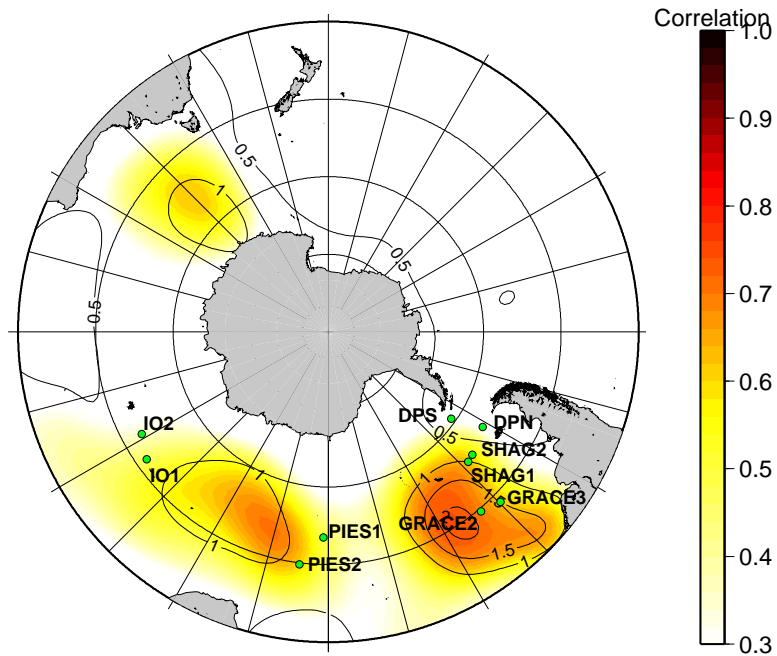


Figure 5.8: Spatial correlation of PIES2 with GRACE (GRGS). The smoothing radius of GRACE is 800 km. Signal to noise contours are drawn in black.

signals in 20 day period band. As this period is too short to be properly detected by GRACE it was feared that this signal would contaminate the monthly estimates. Additionally, the GRACE GRGS solution suffered from a data gap right in the middle of the BPR observation period. The same holds for the GFZ solution which had only three data points in common with the local records and is therefore excluded from the analysis. Finally the GRACE data suffered from a decreased quality in the initial phase of the mission.

The correlations found earlier in the Argentine basin were convincing enough to do the analysis anyway, which yielded some unexpected results.

Figure 5.9 shows the time series of the GRACE GRGS solution with the Argentine basin records. In particular in the first period there is a strong resemblance with both the model and GRACE series. It appears that there is an oscillation with a period of about two months. A previous study, which used altimetry, revealed the presence of a 40 day mode in the Argentine basin [17]. GRACE does not sample this 40 day mode dense enough to retrieve it but some of it may leak in the GRACE solution as an apparent fluctuation at the Nyquist frequency of GRACE ($\approx 60d$). Whether the observed two monthly fluctuations are related to the 40 day mode of [17] remains to be seen.

The correlations associated with the series are consequently high. Some values above 0.9 are obtained for the averaged records. The signal to noise ratios are largest for the averaged records followed by the series of grace3 and grace2. The good agreement with the averaged records show that GRACE is picking up a large scale signal from the Argentine basin. The above analysis again confirms the existence of phenomena in the Argentine Basin which can be detected by GRACE.

Spatial correlations from figure 5.10 indicate an area with large correlations over the Argentine basin. It also confirms, the earlier observation that the phenomena in the Basin

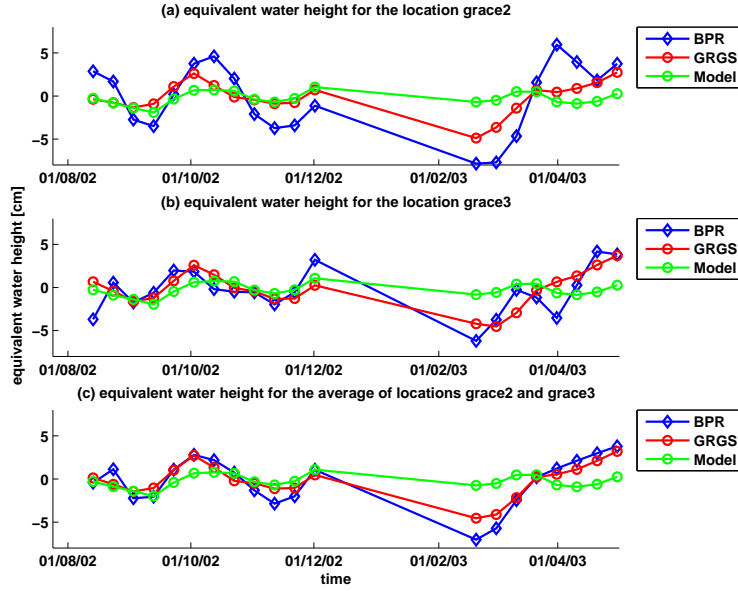


Figure 5.9: Time series of the in situ records in the Argentine Basin and GRACE (GRGS). Also shown are the series for the de-aliasing atmosphere and ocean models. Smoothing radius for GRACE is 800 km. Note that GRACE is missing data in the middle of the observation period.

are stronger linked to the northern PIES2 record than the PIES1 record. This can be seen from the larger correlations closer to the PIES2 deployment location.

North of the Crozet islands there is also an area where good correlations were found. An even more surprising area of high correlation exists on the eastern side of Australia.

The spatial correlations which were found north of the Crozet area and vice versa might not merely be caused by seasonal and semi seasonal signals. Recently, good agreements were found for GRACE averages along ACC fronts compared to independent ocean models [56]. These agreements were mainly found for (semi) annual scales, which were shown to be synchronous in the southern part of the Indian and Pacific ocean basins but not so much for the Atlantic.

The GRGS solution appears to perform somewhat better than the CSR solution. Consistent higher correlations for smoothing radii larger than 600 km are found for the GRGS solution. This can be clearly seen from figure 5.11.

5.3.4 Shags Rock Passage

The records made on each side of the Shags Rock passage were from locations which were the closest together of all used BPR pairs. It is therefore to be expected that the measurements show similarities. However, from figure 5.12 it can be seen that the BPR records show large differences. This suggests that the flow through the passage is changing considerably.

GRACE is not able to detect these high resolution variations. Figure 5.11 shows no significant correlations and similar signatures in the time series do not look as convincing agreements.

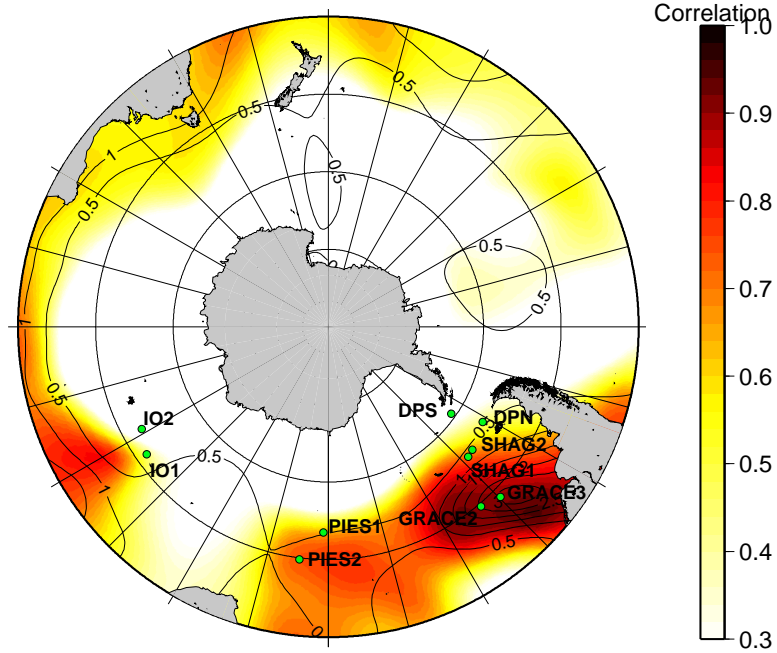


Figure 5.10: Spatial correlation of the mean of grace2 and grace3 with GRACE (GRGS). The smoothing radius of GRACE is 800 km. Signal to noise contours are drawn in black.

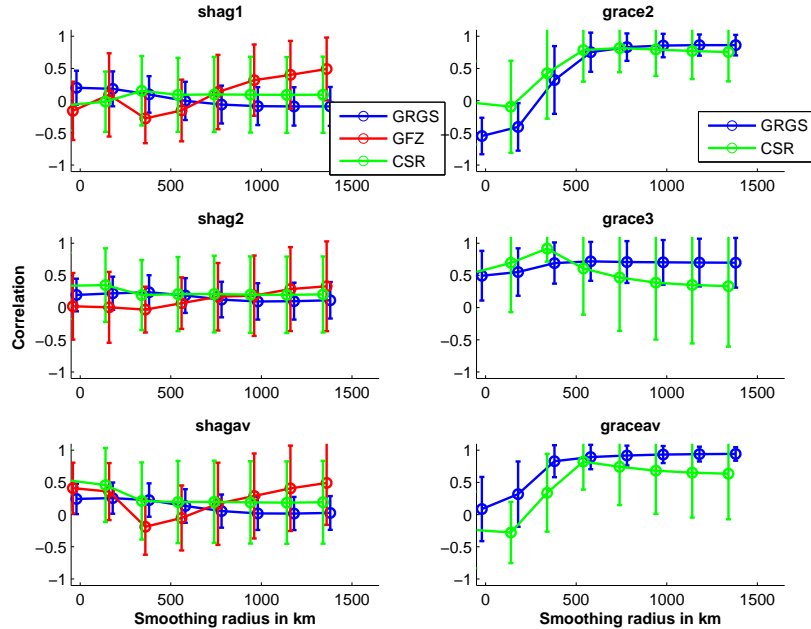


Figure 5.11: Correlation vs. smoothing radius for the Argentine Basin and Shags Rock. Figures are provided for the local measurements and the average at the midpoint (denoted by 'av'). The accuracy of the correlation estimates are reflected in the error bars.

The spatial correlation of SHAG2 shows only weak correlation areas in the Indian ocean. Correlation with phenomena in the South Atlantic are virtually absent. For the SHAGEX

mean and SHAG1 series no correlations worth mentioning were found.

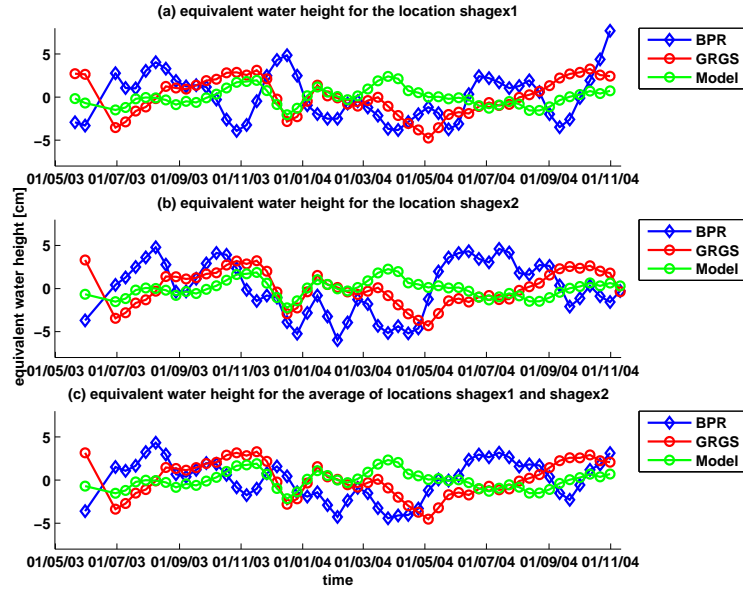


Figure 5.12: Time series of the in situ records near Shags Rock and GRACE (GRGS). Also shown are the series for the de-aliasing atmosphere and ocean models. Smoothing radius for GRACE is 800 km.

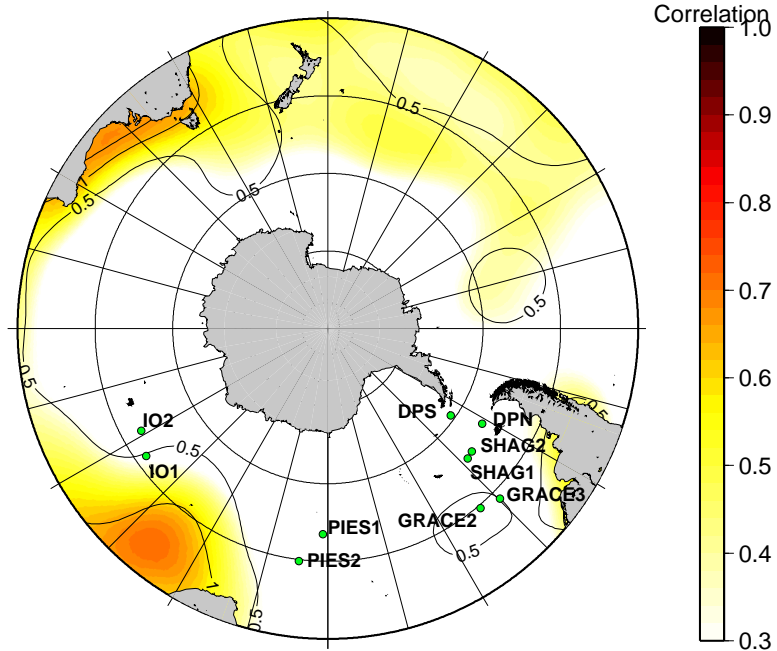


Figure 5.13: Spatial correlation of SHAG2 with GRACE (GRGS). The smoothing radius of GRACE is 800 km. Signal to noise contours are drawn in black.

The bad correlations found with the SHAGEX recorders could be the cause of the propagation of high frequency noise of the recorders. Furthermore the bad agreement between the

daily Q1 tide from FES2004 and from the tidal analysis might cause tidal signal to be aliased in the GRACE solution. However, the closely spaced time series of the BPRs show large differences, while the GRACE solution doesn't. This makes it less plausible that the cause of the discrepancy is caused by tidal aliasing in the GRACE solution. The most likely reason is that the BPRs capture a high resolution feature which is not detectable by GRACE. This is illustrated by the fact that close to the deployment location no spatial correlation was found with GRACE.

5.3.5 Drake Passage

The Drake passage records consist of multiple series ‘glued’ together. From the analysis no strong correlations were found. Only the GRACE GFZ solution appears to have a marginal capability to reproduce the local BPR values of the most southern DPS recorder. This is apparent from figures 5.15 and 5.14, the latter one showing signatures present in both GRACE and GFZ data.

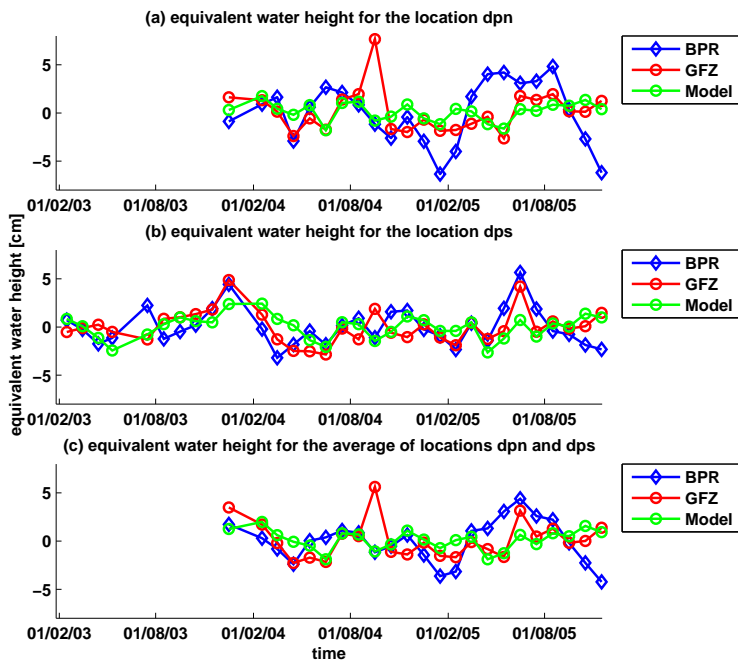


Figure 5.14: Time series of the in situ records in the Drake passage and GRACE (GFZ). Also shown are the series for the de-aliasing atmosphere and ocean models. Smoothing radius for GRACE is 800 km.

The spatial correlation is even weaker than for the SHAG2 case. The DPS record shows a weak correlation band around Antarctica but this can probably be attributed to the continental seasonal signal which causes leakage in the values over sea.

The bad correlation with the Drake records can be caused by aliasing of tidal signal. The Drake passage shows the strongest tidal components of all the in situ records and also the largest errors between the observed and modeled tides. A second explanation is similar to that of the SHAGEX records. The measurements in the Drake passage should yield variations in a large scale phenomena like the ACC. However the bottom pressure is greatly influenced by turbulent flow through the Drake Passage. In figure 4.5 one sees considerable

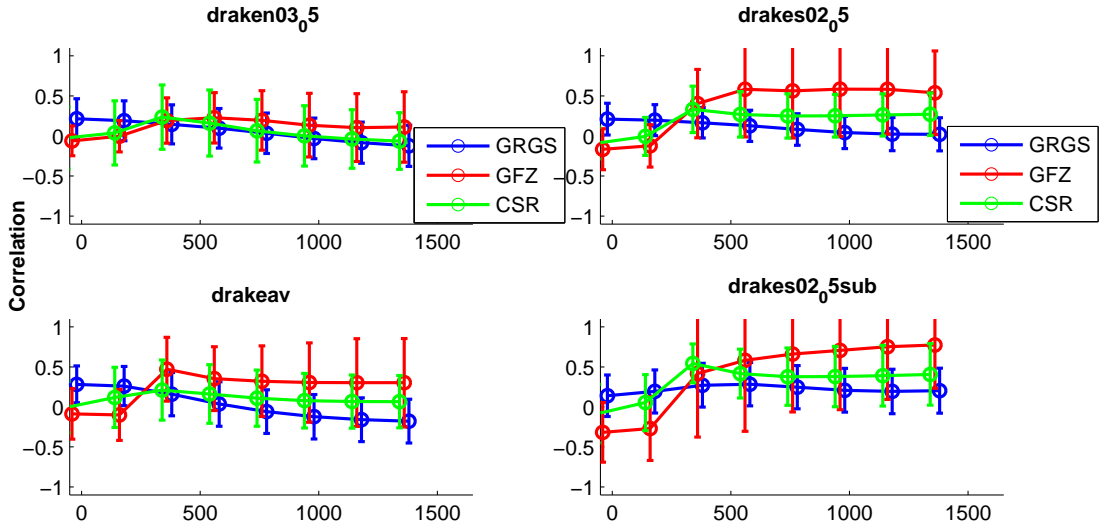


Figure 5.15: Correlation vs. smoothing radius for the Drake passage. Figures are provided for the local measurements and the average at the midpoint (denoted by ‘av’). The accuracy of the correlation estimates are reflected in the error bars. The prefix ‘sub’ denotes that only a subset is used.

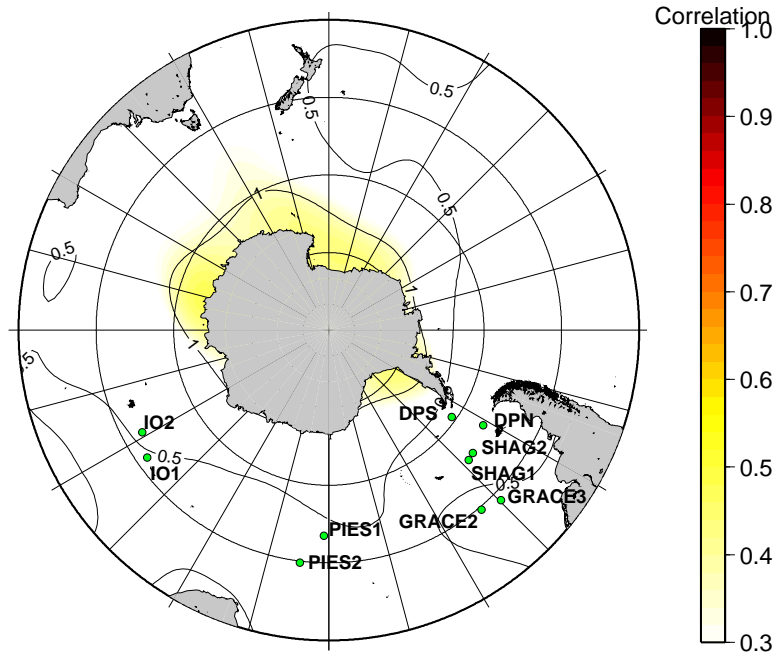


Figure 5.16: Spatial correlation of DPS with GRACE (GRGS). The smoothing radius of GRACE is 800 km. Signal to noise contours are drawn in black.

meanders in the northern part of the Drake passage.

Earlier pressure observations in the Drake passage were found to be difficult to relate to altimetry [23, 55]. Compared to altimetry GRACE displays a much lower resolution and meanders in the fronts cannot be resolved properly. Detection of the variations in the dynamic Drake area by means of GRACE is therefore a challenge.

However from another comparison of BPRs and altimetry the southern measurements were found to show greater discrepancies [55]. From the same study it was found that the southern bottom pressure measurements correlate to a larger extent with the ACC variability than their northern counterparts. This suggests that GRACE is capable of picking up some of the ACC variability. Just recently, this ability has been demonstrated by studying GRACE data along the ACC fronts [56].

5.4 Results of the Geostrophic Flow Comparison

The pairwise deployment of the bottom pressure recorders enables the geostrophic flow between the recorders to be monitored. This offers a unique opportunity to compare the GRACE derived velocities with independent observations of deep ocean transport. The performed comparison is quite ambitious since the capabilities of GRACE on such small spatial scales are questionable.

The section describes the comparison between the geostrophic transport derived from the BPRs with that which is derived from the GRACE solutions. As in the chapter above a discussion of the results will be provided per set of recorders.

The order method will be used to derive the geostrophic transport from GRACE. An other method using the same methodology as the BPR records has been investigated but had, not surprisingly, similar results. The latter one uses the GRACE bottom pressure difference between the BPR locations as opposed to the direct velocity at the midpoint. This has the disadvantage that yet another spatial averaging procedure is applied to the GRACE data. However from the tables it appears that the RMS of the differences benefits from this method, it consistently showed lower values.

All velocities will be scaled with a factor to represent the volume transport through the section above the BPRs. This factor arises from the area bounded by the ocean bottom the sea surface and the verticals above the recorders (figure 4.1).

The GRACE geostrophic flow at the midpoint is again a spatial average and is therefore suited as a comparison candidate for the BPR derived velocity. The BPRs can only observe the velocity component perpendicular to the line connecting the recorders. Therefore east and south components from the GRACE velocity are decomposed accordingly. Tabulated correlations can be found in appendix A.

5.4.1 Crozet Kerguelen Passage

The recorders IO1 and IO2 were placed on both sides of the gap in between the Crozet islands and the Kerguelen. The Kerguelen plateau is an important obstruction for the eastward flow of the ACC. The passage is one of the few crossing points for fronts such as the Polar front.

The BPR observations suggest strong transport fluctuations. Variations of ± 10 Sv are observed for the data from the recorders. Time series are plotted in figure 5.17.

As can be seen from figure 5.18, the in situ flow correlates well with GRACE. Values over 0.6 are reached for the GRGS solution and the GFZ solution. The correlations are somewhat weaker and less accurate than for the bottom pressure.

The GAC model correlations of the GFZ solution are somewhat higher than those of the GRACE estimates themselves. This suggest that GRACE actually deteriorates the estimate from the models. However figure 5.17 illustrates that GRACE displays a larger and more realistic variation compared to the GAC product.

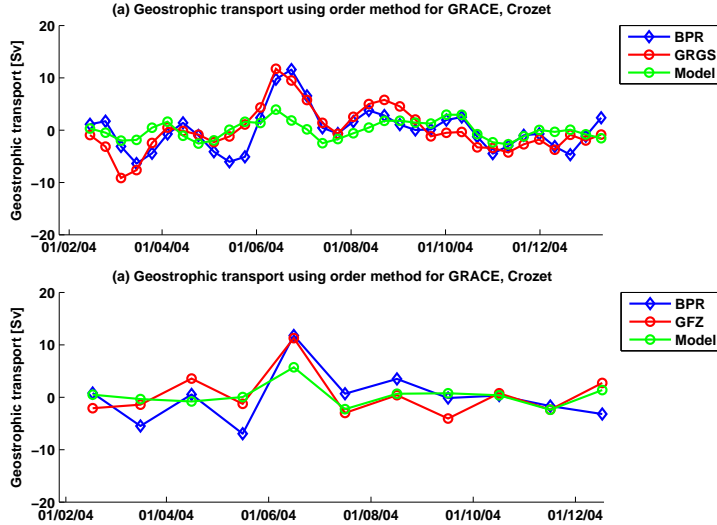


Figure 5.17: Transport time series of the in situ records near Crozet and GRACE (top: GRGS bottom: GFZ). Smoothing radius used is 600 km.

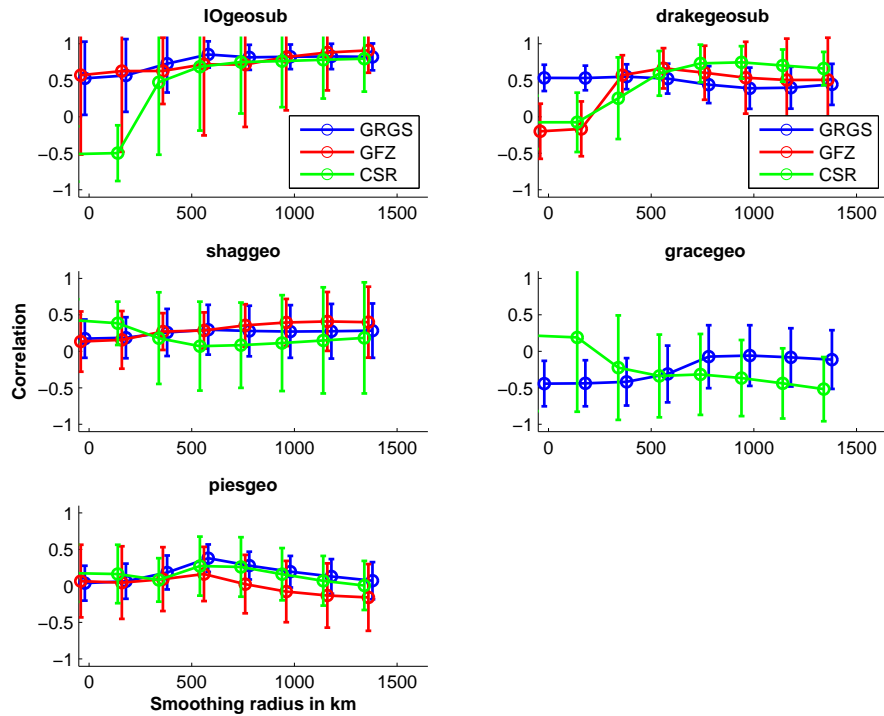


Figure 5.18: Correlation vs. smoothing radius, geostrophic flow comparison.

The correlations are consistent for larger smoothing radii. This implies that the varia-

tions are of a larger scale than merely the separation of the recorders. An observation which is consistent with those found earlier for the bottom pressure.

The geostrophic transport appears to fluctuate with a two month period, right on the Nyquist period of GRACE. This is most apparent for the GRGS solution but can also be seen from the GFZ series. This fluctuation is present in both the BPR measurements and GRACE measurements. A similar mode has already been discussed for the bottom pressure in the Argentine basin.

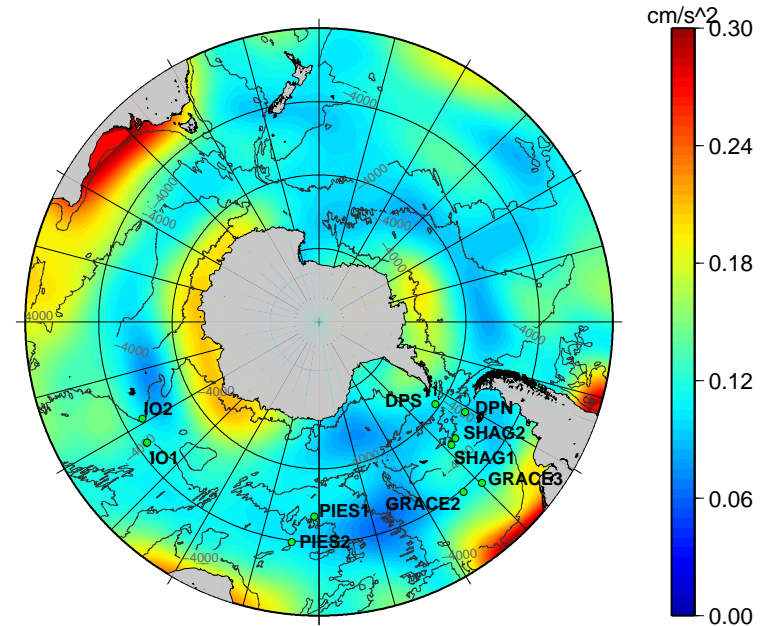


Figure 5.19: Variance of the eastward component of geostrophic flow from GRACE. The observation period considered is from 2002 till 2006. Smoothing radius used is 800 km.

Figure 5.19 shows the variability of the eastward component of the geostrophic flow calculated from GRACE. South east of the Kerguelen is an area of lower variability. This could be an artifact from the leakage of Antarctic continental signal. However there might be a physical explanation for this. From measuring the time averaged drifts of ARGO and PALACE floats a long term mean drift field in the region was obtained [38]. It was found that in the wake of the Kerguelen islands there was a presence of an area of relatively weaker velocities. The exaggerated zonally stretched shape in figure 5.19 could be due to errors propagating more strongly in longitudinal direction. Similar zonal features can also be observed by looking at figure 3.9.

5.4.2 Argentine Basin

The correlation of the flow in between the grace recorders and that of GRACE is somewhat disappointing. No significant correlations exist and some even appear to be negative for small smoothing radii. This implies that, in this region, GRACE is not able to measure the flow at this spatial scale and that larger scale signals are contaminating the estimate. The estimates from the models alone are showing much lower fluctuations than the in situ records. The disagreement could be due to the presence of the 20 day mode discussed earlier.

However there is an interesting feature worth mentioning. Although completely out of phase, both GRACE and the BPR series show a 2 month fluctuation. This mode has now been observed from the bottom pressures and geostrophic flow in the Argentine basin and from the geostrophic flow near Crozet. Where both GRACE as well as the local measurements are consistent. Furthermore, there has already been established that there was a correlation between those areas. And from an earlier mentioned study those agreements might not be of seasonal origin, since the Atlantic shows seasonal signals out of phase compared to those in the Indian ocean [56]. This suggest the interesting possibility that the two monthly mode plays a role in this relation.

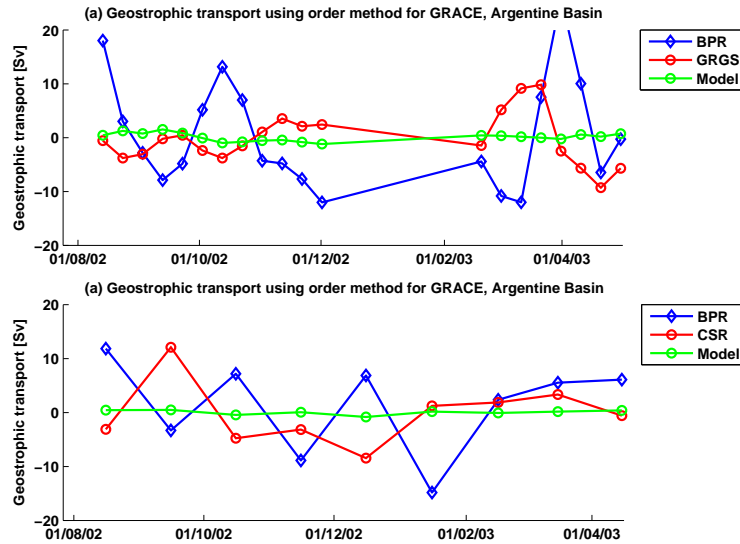


Figure 5.20: Transport time series of the in situ records in the Argentine basin and GRACE (top:GRGS bottom: CSR). Smoothing radius used is 600 km.

5.4.3 South Atlantic

The geostrophic flow in between the two PIES recorders only show a very marginal correlation with GRACE for a smoothing radius of 600 km. The GRACE derived geostrophic flow is therefore not representative for the actual measured flow in between the recorders. Some features are reproduced by both data types (figure 5.21) but this appears to be more of an exception. As mentioned before this location was well suited for a comparison with GRACE. It was expected that GRACE would have been able to detect some of the ACC transport variability. However from this comparison the geostrophic signal appears to be to weak. This is confirmed by the lower GRACE variance for the eastward component in figure 5.19.

5.4.4 Shags Rock and Drake Passage

Correlations with the Shags rock passage transport are non-existent. This comes as no surprise since no convincing correlations were found for the bottom pressure analysis. The records showed large differences among them resulting in very strong geostrophic flow fluctuations. To detect such a difference with satellite gravimetry would require an accurate and high degree gravity field solution, currently non existent.

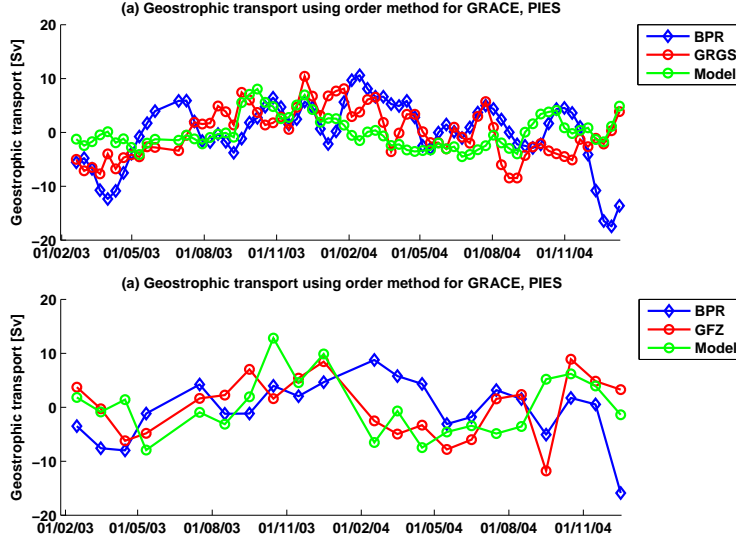


Figure 5.21: Transport time series of the in situ records in the South Atlantic and GRACE (top:GRGS bottom: GFZ). Smoothing radius used is 600 km.

From figure 5.18 it appears that GRACE, is showing good correlations with the local measurements. However a closer look at the tables in appendix A tells us that the dealiasing models consistently show higher correlations. Figure 5.22 shows the time series at the Drake passage. When the anomalous large GRACE value is excluded the correlation is increased but not above the GAC values. This implies that GRACE is actually deteriorating the estimates from the models somewhat and is only of marginal use here. As mentioned before, the Drake passage is a turbulent area in which strong phenomena, such as meanders, with relatively small spatial scales exist. It is of no surprise that GRACE is not able to detect such features. It can be conclude however that the geostrophic flow measured by the recorders is adequately reflecting the variation of the transport through the Drake passage.

At other locations the local transport series of the Drake passage appear to be related to large scale eastward flow derived from GRACE. This can be seen from figure 5.23, where the local measurements are correlated with the eastward GRACE velocity at other locations. A large area of good correlations can be seen in the Atlantic and Indian ocean. Whether this correlation can be attributed to GRACE or just to the de-aliasing product remains to be seen, but what remains obvious is that the measured Drake transport is related to the ACC variability around Antarctica.

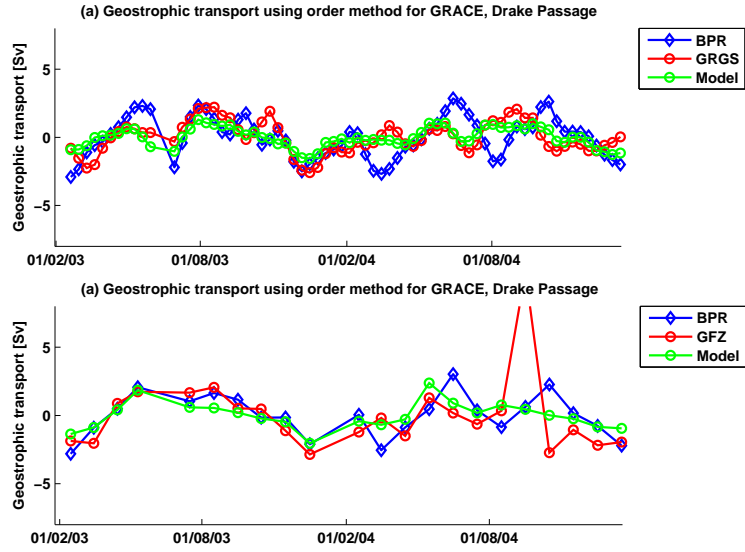


Figure 5.22: Transport time series of the in situ records in the Drake passage and GRACE (top:GRGS bottom: GFZ). Smoothing radius used is 600 km.

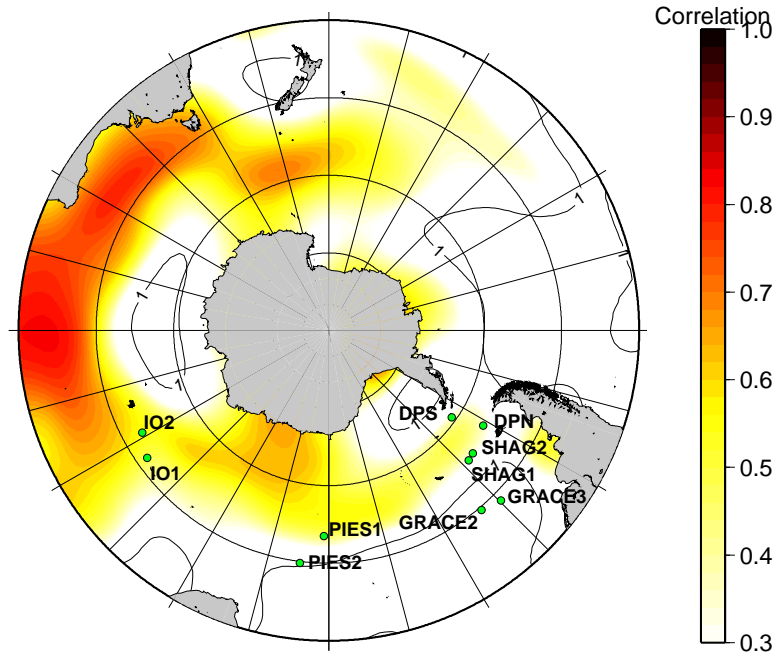


Figure 5.23: Spatial correlation of the local Drake passage geostrophic flow with GRACE (GRGS). The smoothing radius of GRACE is 800 km. Signal to noise contours are drawn in black.

Chapter 6

Conclusions and Recommendations

The main results of the analysis are summarized in this chapter. Furthermore a discussion of the obtained results is provided, in which possible topics for future research are proposed.

6.1 Conclusion

The first aim of this thesis work was to validate the GRACE bottom pressure estimates from independent in situ recorders. Ten of those recorders were used in the analysis all placed in the southern ocean. This area was suited because a large scale barotropic component was expected due to the presence of the ACC.

The conclusion can be made that GRACE detects large scale oceanic bottom pressure variations in the Southern ocean, with reasonable accuracy. Furthermore there are areas in the Southern ocean where GRACE shows an ability to observe geostrophic flow directly.

The results for the comparison are not of homogeneous nature. Regions of strong agreement are found in the southern Indian Ocean and in the Argentine basin.

Below one finds a more elaborate summary of the conclusion which can be drawn from this thesis work.

Local Bottom Pressure Validation

The bottom pressure recorders near the Crozet and Kerguelen islands showed a good agreement with the GRACE estimates. Correlations above 0.8 were achievable for the optimal situations. The average of the in situ records showed an RMS of as low as 7 mm for a smoothing radius of 600 km.

The good agreement appears to be due to large scale variations both detected by the in situ recorders and GRACE. Those large scale signals might be due to the presence of the Kerguelen plateau strongly influencing the circulation in the area on a large scale.

Good agreements were also found for the recorders in the Argentine basin with high correlations reaching values over 0.9 and good signal to noise ratios. This was unexpected since the BPR records were dominated by a 20 day mode in the raw records. Apparently the averaging procedure removed this efficiently. The most eastern BPR (grace2) showed slightly better results.

Records in the South Atlantic showed a somewhat lesser but significant agreement with GRACE. RMS errors of around 1.6 cm were shown for the comparison with the average of

the two local series.

Only the southern in situ record in the Drake passage showed a marginal agreement with GRACE. Maximum correlations of 0.7 were obtained for the GFZ solution but with low accuracy.

The Shags rock recorders showed no significant agreement. Although their separation was small, the differences between the recorders were large, suggesting large variations on small spatial scales. Signals measured by the SHAGEX recorders are not detectable by GRACE due to the high resolution nature of the phenomena associated.

Regions of Interest

The bottom pressure series of the local records identified some interesting areas for which the GRACE solution showed agreements with the distant BPRs.

Phenomena in the Argentine basin appear to be closely related to phenomena in the Crozet Kerguelen region. A possibility is that this is caused by synchronous seasonal signals, however this contradicts a recent observation from GRACE and ocean models [56]. Further investigation in those areas would serve as an interesting subject of study.

The variance of the GRACE solution showed centers of high variability which agreed with earlier observations from altimetry. These centers were in the Argentine basin, over the Kerguelen plateau and West of the Drake passage.

Geostrophic flow comparison

The observations of the local geostrophic flow through the Crozet Kerguelen passage agree to a large extent with the GRACE derived velocity. Large correlations up to 0.8 are found for the flow across this section. RMS values of the differences as low as 0.7 mm/s were found for a smoothing radius of 600 km.

Again, this agreement must be due to the fact that the recorders measure part of a larger signal, which can be picked up by GRACE quite accurately.

Marginal agreements were found in the Drake passage where it must be mentioned that the GAC product showed a better resemblance with the local measurements than GRACE. The local records did however seem to reflect the variability of the ACC in the Southern Ocean.

Comparison between different GRACE solutions

The three different GRACE solutions performed differently in the analyzed areas. The CSR solution showed the least realistic behavior, where fluctuations were in general overestimated. These fluctuations are now generally believed to be caused by anomalous values of the C_{20} coefficient, associated with the release 1 product, and is improved in later solutions. The GFZ solution and the GRGS solution were comparable in performance. The GRGS solution showed better results in the Crozet Kerguelen region and the GFZ solution appeared to perform better in the Drake Passage.

The advantage of the GRGS solution is that it contains more measurements in a certain timespan making it more suitable to compare with BPR series which in general cover only short observation periods.

Two monthly mode

From the bottom pressure in the Argentine Basin and from the geostrophic flow through

the Crozet Kerguelen passage it appears that there exists a mode with a period of around two months in the Southern Ocean. Both the GRACE solution and the local measurements display this mode. It remains unclear whether this mode is the cause of the apparent link between the Argentine Basin and the Crozet Kerguelen region. In a previous study a smaller mode over the Argentine basin was discovered with a 40 day period [17]. Whether those modes are related is an interesting subject of future research.

6.2 Discussion and Recommendations

The performed analysis suffer from some shortcomings. First of all, since the used BPR series were short, the amount of GRACE data within this time span was limited. Outliers in either the GRACE data or the local measurements therefore have a relatively large influence on the results.

The use of the GRGS solution for comparison is favorable since it has a larger density of measurements. However the individual solutions will be correlated with the neighboring solutions. This decreases the apparent Nyquist frequency of twenty days toward two months. The error estimates of the correlation coefficients assume that the data points are not correlated, which is in fact an erroneous assumption.

The two monthly mode which has been observed is on the limit of the detection capabilities of GRACE. Further research is therefore necessary to make more conclusive statements about this mode. It is possible that fluctuations with a somewhat higher frequency leak into the GRACE solution as an apparent two monthly mode. It is my opinion that a GRACE solution with a higher temporal resolution, at the cost of spatial resolution, would provide valuable information in the study of oceanic signals such as those found in the southern ocean.

The cause of the agreement between the Argentine basin and the Crozet Kerguelen region remains unclear. Seasonal signals might be the cause but the two monthly mode might be a contributor as well. It would serve useful to extract the seasonal terms in the GRACE data and do the comparison again to investigate whether higher frequency phenomena are causing the agreement.

Considering the above, it is highly recommended to do an Empirical Orthogonal Function analysis to identify those possible modes and to establish a fundamental frame work to study those inter-location agreements. Although an EOF analysis has been originally planned as part of this thesis work it was canceled due to time constraints.

The oceanic models and the ECMWF fields influence to a large extend the GRACE solution over the oceans. GRACE provides only a valuable addition when the estimates of the models are enhanced by GRACE. This has not always been the case in this analysis and therefore one must proceed with caution to make conclusive statements about the measurement capabilities of GRACE. The comparison against the de-aliasing product must therefore always be included.

In this thesis the GRACE solution has not been masked over land. This potentially causes land hydrological signals to contaminate the GRACE solution over the ocean. It is recommended to mask the spherical harmonic coefficients using the method described by [43] when analyzing BPRs positioned close to the coast. An attempt has been made to at least remove the atmospheric signal above land by converting the spherical harmonics to a masked grid and subsequently use a spatial averaging kernel to make them equivalent to the GRACE solution. However this had mixed results for different locations, took much computation time

and yielded an enormous amount of data, consequently the idea was abandoned. The newer GRGS corrections, which were kindly provided to me earlier this year, are all masked over land, in contrast to the GAC products¹. Furthermore, the newer GRGS corrections were also averaged according to their GRACE equivalent, in contrast to the monthly averages used earlier. This yielded a particular improvement for the geostrophic flow comparison for the Indian ocean records.

The good agreement of GRACE around the Crozet and Kerguelen passage invites future researchers to combine altimetry observations with GRACE bottom pressure estimates in the area. The theory elaborated in [41] is a prime candidate for monitoring the flow through the Crozet Kerguelen passage using space-borne techniques.

¹At the time of writing a release 4 GAD product has been released which reduces the leakage of land hydrological signal over the ocean

Acknowledgments

This study could not have been performed without the help and data of several institutes and their researchers. The deployment of in situ pressure records involves large investments in money and personnel. Similarly, the designing, launching and operating of the GRACE satellites requires several investors and dedicated researchers. Once data is acquired their value strongly depends on the researchers interpreting it. For this project several institutes and people deserve to be mentioned:

- Pascal LeGrand, Olivier Peden, IFREMER (Institut Français de Recherche pour l'Exploitation de la Mer): Deployment of the South Indian ocean BPRs.
- IPEV (Institut Polaire Francais Paul Emile Victor): Allowing the deployment of the IFREMER BPRs from the vessel Marion Dufresne.
- Chris Hughes, Peter Foden, Proudman Oceanographic Laboratory (POL): Deployment of the Drake passage BPRs, the Argentine basin BPRs, Shags Rock BPRs and for collecting the South Indian ocean BPRs
- Andreas, Macrander, Alfred Wegener Institute (AWI): Supplying South Atlantic BPR data and deployment of the arrays.
- Guillaume Ramillien and Jean-Michel Lemoine, Laurent Testut, Laboratoire d'Etudes en Géophysique et Océanographie Spatiales (LEGOS): French GRGS solution and their atmospheric and oceanic dealiasing corrections and BPR processing strategy.
- GRACE science team, Center of Space research (CSR), GeoForschungZentrum (GFZ), Jet Propulsion Laboratory (JPL): Monthly GRACE solutions and dealiasing products.

Bibliography

- [1] National Aeronautics and Space Administration (NASA). FY 2003 congressional budget, 2003.
http://www.nasa.gov/pdf/118829main_FY03_budget.pdf.
- [2] M. Arhan, A. C. Naveira Garabato, K. J. Heywood, and D. P. Stevens. The Antarctic Circumpolar Current between the Falkland Islands and South Georgia. *Journal of Physical Oceanography*, 32(6):1914–1931, June 2002.
- [3] J. Carpenter and J. Bithell. Bootstrap confidence intervals: when, which, what? A practical guide for medical statisticians. *Statistics in Medicine*, 19(9):1141–1164, 2000.
- [4] L. Carrère and F. Lyard. Modeling the barotropic response of the global ocean to atmospheric wind and pressure forcing - comparisons with observations. *Geophysical Research Letters*, 30:8–1, March 2003.
- [5] D. P. Chambers. Evaluation of new GRACE time-variable gravity data over the ocean. *Geophysical Research Letters*, 33:17603–+, September 2006.
- [6] D. P. Chambers. Observing seasonal steric sea level variations with GRACE and satellite altimetry. *Journal of Geophysical Research (Oceans)*, 111(C10):3010–+, March 2006.
- [7] DP Chambers, J Wahr, and RS Nerem. Preliminary observations of global ocean mass variations with GRACE. *Geophysical Research Letters*, 31(13), July 2004.
- [8] B. F. Chao. <http://www.agu.org/sections/geodesy/images/Earth.png>.
- [9] B. F. Chao and R. S. Gross. Changes in the earth's rotation and low-degree gravitational field induced by earthquakes. *Geophysical Journal*, 91:569–596, December 1987.
- [10] J. L. Chen, M. Rodell, C. R. Wilson, and J. S. Famiglietti. Low degree spherical harmonic influences on Gravity Recovery and Climate Experiment (GRACE) water storage estimates. *Geophysical Research Letters*, 32:14405–+, July 2005.
- [11] J.-F. Crétaux, L. Soudarin, F. J. M. Davidson, M.-C. Gennero, M. Bergé-Nguyen, and A. Cazenave. Seasonal and interannual geocenter motion from SLR and DORIS measurements: Comparison with surface loading data. *Journal of Geophysical Research (Solid Earth)*, 107, December 2002.
- [12] A. Dutt and V. Rokhlin. Fast fourier transforms for nonequispaced data. *SIAM Journal on Scientific Computing*, 14(6):1368–1393, 1993.
- [13] M.C. Eble and F.I. Gonzalez. Deep-Ocean Bottom Pressure Measurements in the Northeast Pacific. *J. Atmos. Oceanic Tech.*, 8(2):221–233, April 1991.
- [14] W. E. Farrell. Deformation of the Earth by Surface Loads. *Reviews of Geophysics and Space Physics*, 10:761–+, August 1972.

- [15] M.G.G. Foreman. *Manual for Tidal Heights analysis and prediction*. Institute of Ocean Sciences, Patricia Bay Victoria, B.C., 1977(rev.1996).
- [16] Matteo Frigo and Steven G. Johnson. The design and implementation of FFTW3. *Proceedings of the IEEE*, 93(2):216–231, 2005. special issue on "Program Generation, Optimization, and Platform Adaptation".
- [17] L-L Fu, B Cheng, and B Qiu. 25-Day Period Large-Scale Oscillations in the Argentine Basin Revealed by the TOPEX/Poseidon Altimeter. *Journal of Physical Oceanography*, 31(2):506–517, February 2001.
- [18] Leslie Greengard and June-Yub Lee. Accelerating the nonuniform fast fourier transform. *SIAM Review*, 46(3):443–454, 2004.
- [19] D. Han and J. Wahr. The viscoelastic relaxation of a realistically stratified Earth, and a further analysis of postglacial rebound. *Geophysical Journal International*, 120(2):287–311, February 1995.
- [20] Shin-Chan Han. *Efficient global gravity determination from satellite-to-satellite tracking (SST)*. PhD thesis, The Ohio State University, September 2003.
- [21] W. A. Heiskanen and H. Moritz. *Physical Geodesy*. W. H. Freeman and Co., 1967.
- [22] C. W. Hughes, V. N. Stepanov, L.-L. Fu, B. Barnier, and G. W. Hargreaves. Three forms of variability in Argentine Basin ocean bottom pressure. *Journal of Geophysical Research*, 112, January 2007.
- [23] C. W. Hughes, P. L. Woodworth, M. P. Meredith, V. Stepanov, T. Whitworth, and A. R. Pyne. Coherence of Antarctic sea levels, Southern Hemisphere Annular Mode, and flow through Drake Passage. *Geophysical Research Letters*, 30:17–1, May 2003.
- [24] S. S. Jacobs and D. T. Georgi. Observations on the southwest indian/antarctic ocean. In *A Voyage of Discovery*, pages 43–84. Pergamon Press, Oxford, 1977.
- [25] C. Jekeli. *Alternative methods to smooth the Earth's gravity field*. The Ohio State University, December 1981.
- [26] Christopher Jekeli. The determination of gravitational potential differences from satellite-to-satellite tracking. *Celestial Mechanics and Dynamical Astronomy*, 75:85–101(17), October 1999.
- [27] T. Kanzow, F. Flechtner, A. Chave, R. Schmidt, P. Schwintzer, and U. Send. Seasonal variation of ocean bottom pressure derived from gravity recovery and climate experiment (grace): Local validation and global patterns. *Journal of Geophysical Research*, 110, 2005.
- [28] W. M. Kaula. *Theory of satellite geodesy. Applications of satellites to geodesy*. Waltham, Mass.: Blaisdell, 1966, 1966.
- [29] M. Llubes, J-M. Lemoine, and F. Rémy. Antarctica seasonal mass variations detected by GRACE, 2006. submitted to Earth and Planetary Science Letters.
- [30] T. M. MacRobert. *Spherical Harmonics, An Elementary Treatise on Harmonic Functions with Applications*. Pergamon Press, 3rd edition, 1967.
- [31] M. P. Meredith and C. W. Hughes. On the wind-forcing of bottom pressure variability at Amsterdam and Kerguelen Islands, southern Indian Ocean. *Journal of Geophysical Research (Oceans)*, 109(C18):3012–+, March 2004.

- [32] H. Moritz. Geodetic Reference System 1980. *Journal of Geodesy*, 66(2):187–192, 1992.
- [33] Y.-H. Park and L. Gambéroni. Large-scale circulation and its variability in the south Indian Ocean from TOPEX/POSEIDON altimetry. *Journal of Geophysical Research*, 100:24911–24930, December 1995.
- [34] Y.-H. Park, L. Gamberoni, and E. Charriaud. Frontal structure and transport of the Antarctic Circumpolar Current in the south Indian Ocean sector, 40 – 80° E. *Marine Chemistry*, 35:45–62, 1991.
- [35] Y.-H. Park, L. Gamberoni, and E. Charriaud. Frontal structure, Water Masses, and Circulation in the Crozet Basin. *Journal of Geophysical Research*, 98(C7):12,361–12,385, 1993.
- [36] R.G. Peterson and L. Stramma. Upper-level circulation in the South Atlantic Ocean. *Progress in Oceanography*, 26:1–73, 1990.
- [37] R. Rietbroek. Social responsibility of the military engineer. Essay Platform Ethiek en Techniek, Technische Universiteit Delft, 2005 available at: <http://www.platformet.tudelft.nl/download/socialrespon2.pdf>.
- [38] J-B. Sallée, N. Wienders, Speer K., and R. Morrow. Formation of subantarctic mode water in the southeastern Indian Ocean. *Ocean Dynamics*, 56(5):525–542, December 2005.
- [39] E.J.O. Schrama. Tides. Lecture notes Earth oriented space research, course AE4-876, University of Technology Delft, February 2007.
- [40] D. Smythe-Wright and S. Boswell. Abyssal circulation in the Argentine Basin. *Journal of Geophysical Research*, 103:15845–15852, 1998.
- [41] Y. T. Song. Estimation of interbasin transport using ocean bottom pressure: Theory and model for Asian marginal seas. *Journal of Geophysical Research (Oceans)*, 111(C10):11–+, November 2006.
- [42] M. D. Sparrow, K. J. Heywood, J. Brown, and D. P. Stevens. Current structure of the south Indian Ocean. *Journal of Geophysical Research*, 101 (C3):6377–6391, 1996.
- [43] S. Swenson and J. Wahr. Methods for inferring regional surface-mass anomalies from Gravity Recovery and Climate Experiment (GRACE) measurements of time-variable gravity. *Journal of Geophysical Research (Solid Earth)*, 107:3–1, September 2002.
- [44] S. Swenson and J. Wahr. Post-processing removal of correlated errors in GRACE data. *Geophysical Research Letters*, 33, 2006.
- [45] B. D. Tapley, S. Bettadpur, J. C. Ries, P. F. Thompson, and M. M. Watkins. GRACE Measurements of Mass Variability in the Earth System. *Science*, 305:503–506, July 2004.
- [46] B. D. Tapley, S. Bettadpur, M. Watkins, and C. Reigber. The gravity recovery and climate experiment: Mission overview and early results. *Geophysical Research Letters*, 31:9607–+, May 2004.
- [47] B. D. Tapley and Ch. Reigber. GRACE: Gravity Recovery And Climate Experiment - An Earth System Science Pathfinder (ESSP) Mission.
<http://www.csr.utexas.edu/grace/publications/presentations/HPC2001.html>.
- [48] M. Thomas, J. Sündermann, and E. Maier-Reimer. Consideration of ocean tides in an OGCM and impacts on subseasonal to decadal polar motion excitation. *Geophysical Research Letters*, 28:2457–2460, June 2001.

- [49] J. M. Vassie, A. J. Harrison, P. L. Woodworth, S. A. Harangozo, M. J. Smithson, and S. R. Thompson. On the temporal variability of the transport between Amsterdam and Kerguelen islands. *Journal of Geophysical Research*, 99:937–950, January 1994.
- [50] I. Velicogna and J. Wahr. Acceleration of Greenland ice mass loss in spring 2004. *Nature*, 443(7109):329–331, 2006.
- [51] J. Wahr, M. Molenaar, and F. Bryan. Time variability of the Earth’s gravity field: Hydrological and oceanic effects and their possible detection using GRACE. *Journal of Geophysical Research*, 103:30205–30230, December 1998.
- [52] J. M. Wahr, S. R. Jayne, and F. O. Bryan. A method of inferring changes in deep ocean currents from satellite measurements of time-variable gravity. *Journal of Geophysical Research (Oceans)*, 107:11–1, December 2002.
- [53] P. Welch. The use of fast Fourier transform for the estimation of power spectra: A method based on time averaging over short, modified periodograms. *Audio and Electroacoustics, IEEE Transactions on*, 15(2):70– 73, June 1967.
- [54] Wikipedia. Military of the United States, 2006. url address:
http://en.wikipedia.org/wiki/Military_of_the_United_States.
- [55] P. L. Woodworth, J. M. Vassie, C. W. Hughes, and M. P. Meredith. A test of the ability of TOPEX/POSEIDON to monitor flows through the Drake Passage. *Journal of Geophysical Research*, 101:11935–11948, 1996.
- [56] V. Zlotnicki, J. Wahr, I. Fukumori, and Y. Song. Antarctic Circumpolar Current Transport Variability during 2003-05 from GRACE. *Journal of Physical Oceanography*, 37(2):230–244, February 2007.

Appendix A

Correlation Tables

The tables below are the output of the correlation analysis. Tables are provided for the GRACE solution of the computing centers GRGS, CSR and GFZ¹ and are grouped according to smoothing radius. The selected BPR channels are the best performing ones, but unless they are very noisy the differences are not very significant.

A.1 Bottom Pressure

The symbol ρ denotes the correlation coefficient, with its lower 95 % confidence interval supplied. The approximate signal to noise ratio is shown in the column denoted by SNR . The standard deviations, σ_{grc} and σ_{BPR} are in cm and for the GRACE and BPR series respectively. The number of shared datapoints is provided in the third column. The locations which have a ‘sub’ appended to their names only use a subset of the BPR data. The names which contain an ‘av’ are obtained from averaging the neighboring BPR pairs and using the midpoint as a the reference. There is also a column denoted by ρ_{mod} which indicate the correlation with the dealiasing models only. Finally the RMS, in cm, of the difference of the compared series is tabulated in the last column.

| Location | Span (yyymmdd) | No | ρ | 95% _{low} | ρ_{mod} | SNR | σ_{grc} | σ_{BPR} | RMS |
|----------------|----------------|-----|--------|--------------------|--------------|-------|----------------|----------------|------|
| IO1 | 040123-050217 | 36 | 0.63 | 0.24 | 0.069 | 1.2 | 1.9 | 2.1 | 1.8 |
| IO2 | 040124-050131 | 34 | 0.71 | 0.44 | 0.49 | 1.9 | 2.1 | 1.9 | 1.5 |
| IOav | 040124-050131 | 34 | 0.68 | 0.31 | 0.27 | 1.7 | 1.9 | 1.7 | 1.5 |
| IO1sub | 040301-050217 | 32 | 0.88 | 0.76 | 0.38 | 3.6 | 1.9 | 2 | 1 |
| IO2sub | 040301-050131 | 30 | 0.84 | 0.76 | 0.82 | 3.4 | 1.9 | 1.7 | 1 |
| IOavsub | 040301-050129 | 30 | 0.93 | 0.88 | 0.69 | 6.8 | 1.8 | 1.5 | 0.69 |
| grace2 | 020516-030516 | 20 | 0.75 | 0.45 | 0.24 | 0.78 | 2.3 | 4 | 2.6 |
| grace3 | 020517-030517 | 20 | 0.72 | 0.41 | 0.29 | 1.8 | 2.7 | 2.6 | 2 |
| graceav | 020516-030516 | 20 | 0.89 | 0.7 | 0.3 | 4 | 2.5 | 2.8 | 1.3 |
| pies1 | 021201-050131 | 68 | 0.66 | 0.5 | 0.28 | 0.8 | 2 | 3 | 2.2 |
| pies2 | 021129-050128 | 68 | 0.62 | 0.46 | 0.23 | 0.88 | 1.9 | 2.5 | 2 |
| piesav | 021129-050126 | 68 | 0.74 | 0.61 | 0.29 | 1.4 | 1.9 | 2.4 | 1.6 |
| shag1 | 030505-041117 | 52 | -0.004 | -0.3 | -0.45 | 0.35 | 2 | 2.7 | 3.4 |
| shag2 | 030507-041128 | 52 | 0.19 | -0.082 | -0.17 | 0.32 | 1.9 | 3.1 | 3.4 |
| shagav | 030507-041117 | 51 | 0.13 | -0.13 | -0.41 | 0.48 | 1.9 | 2.3 | 2.7 |
| drakes02-05 | 021227-051211 | 100 | 0.005 | -0.18 | -0.32 | 0.41 | 1.6 | 2 | 2.5 |
| drakes02-05sub | 021227-040601 | 44 | 0.28 | 0.012 | -0.35 | 0.58 | 1.8 | 2.1 | 2.4 |
| draken03-05 | 031031-051207 | 74 | -0.004 | -0.22 | -0.25 | 0.19 | 1.5 | 3.1 | 3.5 |
| drakeav | 031031-051207 | 74 | -0.14 | -0.4 | -0.54 | 0.27 | 1.4 | 2.1 | 2.7 |

Table A.1: Pressure correlations of GRACE GRGS ($r_{smooth} = 600$ km) with BPRs.

¹ Argentine basin bottom pressure records are omitted since only three data points were shared in the observation period

| Location | Span (yymmdd) | No | ρ | $95\%_{low}$ | ρ_{mod} | SNR | σ_{grc} | σ_{BPR} | RMS |
|----------------|---------------|----|--------|--------------|--------------|-------|----------------|----------------|-----|
| IO1 | 040123-050217 | 12 | 0.59 | 0.18 | 0.2 | 1.5 | 3.1 | 2.3 | 2.5 |
| IO2 | 040124-050131 | 12 | 0.65 | 0.46 | 0.094 | 1.7 | 3.6 | 2 | 2.7 |
| IOav | 040124-050131 | 12 | 0.65 | 0.41 | 0.15 | 1.7 | 3.4 | 1.8 | 2.6 |
| IO1sub | 040301-050217 | 11 | 0.72 | 0.46 | 0.8 | 2.1 | 3.3 | 2.1 | 2.3 |
| IO2sub | 040301-050131 | 11 | 0.7 | 0.55 | 0.56 | 1.9 | 3.7 | 1.9 | 2.7 |
| IOavsub | 040301-050129 | 10 | 0.74 | 0.47 | 0.83 | 1.9 | 3.4 | 1.5 | 2.5 |
| grace2 | 020516-030516 | 9 | 0.79 | 0.29 | 0.31 | 0.65 | 2 | 3.6 | 2.5 |
| grace3 | 020517-030517 | 9 | 0.61 | -0.11 | -0.27 | 0.85 | 2.4 | 3.2 | 2.6 |
| graceav | 020516-030516 | 9 | 0.82 | 0.39 | 0.043 | 1.4 | 2.2 | 3.1 | 1.8 |
| pies1 | 021201-050131 | 24 | 0.62 | 0.37 | 0.23 | 1.6 | 3.9 | 2.7 | 3.1 |
| pies2 | 021129-050128 | 24 | 0.65 | 0.34 | 0.38 | 1.7 | 3.1 | 2.3 | 2.4 |
| piesav | 021129-050126 | 24 | 0.77 | 0.61 | 0.44 | 2.3 | 3.7 | 2.1 | 2.5 |
| shag1 | 030505-041117 | 16 | 0.09 | -0.48 | -0.093 | 0.72 | 3.1 | 2.3 | 3.7 |
| shag2 | 030507-041128 | 16 | 0.21 | -0.37 | 0.17 | 0.65 | 3.1 | 3 | 3.9 |
| shagav | 030507-041117 | 16 | 0.19 | -0.44 | 0.047 | 0.83 | 3.1 | 2.1 | 3.4 |
| drakes02-05 | 021227-051211 | 32 | 0.27 | -0.015 | -0.17 | 1 | 3.1 | 1.6 | 3.1 |
| drakes02-05sub | 021227-040601 | 16 | 0.42 | 0.11 | -0.14 | 1.1 | 2.6 | 1.8 | 2.5 |
| draken03-05 | 031031-051207 | 22 | 0.16 | -0.25 | -0.25 | 0.56 | 2.9 | 3 | 3.9 |
| drakeav | 031031-051207 | 22 | 0.16 | -0.2 | -0.54 | 0.86 | 3.1 | 1.8 | 3.3 |

 Table A.2: Pressure correlations of GRACE CSR ($r_{smooth} = 600$ km) with BPRs.

| Location | Span (yymmdd) | No | ρ | $95\%_{low}$ | ρ_{mod} | SNR | σ_{grc} | σ_{BPR} | RMS |
|----------------|---------------|----|--------|--------------|--------------|-------|----------------|----------------|-----|
| IO1 | 040123-050217 | 12 | 0.7 | -0.075 | 0.31 | 1.3 | 1.9 | 2.3 | 1.7 |
| IO2 | 040124-050131 | 11 | 0.61 | 0.39 | 0.61 | 1.3 | 2 | 2 | 1.7 |
| IOav | 040124-050131 | 11 | 0.64 | -0.13 | 0.42 | 1.5 | 1.9 | 1.8 | 1.6 |
| IO1sub | 040301-050217 | 11 | 0.78 | 0.13 | 0.45 | 2.1 | 2 | 2.1 | 1.4 |
| IO2sub | 040301-050131 | 10 | 0.6 | 0.35 | 0.83 | 1.4 | 2 | 1.7 | 1.7 |
| IOavsub | 040301-050129 | 10 | 0.71 | -0.088 | 0.69 | 2 | 2 | 1.5 | 1.4 |
| pies1 | 021201-050131 | 22 | 0.63 | 0.38 | 0.28 | 1.3 | 2.6 | 2.7 | 2.3 |
| pies2 | 021129-050128 | 21 | 0.62 | 0.34 | 0.46 | 1.2 | 2.2 | 2.4 | 2 |
| piesav | 021129-050126 | 21 | 0.75 | 0.54 | 0.56 | 2.1 | 2.4 | 2.2 | 1.6 |
| shag1 | 030505-041117 | 15 | -0.15 | -0.63 | 0.13 | 0.47 | 2.6 | 2.3 | 3.8 |
| shag2 | 030507-041128 | 15 | 0.069 | -0.33 | -0.36 | 0.56 | 3.1 | 3 | 4.2 |
| shagav | 030507-041117 | 15 | -0.053 | -0.56 | -0.21 | 0.61 | 2.9 | 2.2 | 3.7 |
| drakes02-05 | 021227-051211 | 32 | 0.58 | -0.012 | 0.23 | 0.97 | 1.6 | 1.9 | 1.6 |
| drakes02-05sub | 021227-040601 | 14 | 0.58 | -0.3 | 0.37 | 0.92 | 1.5 | 1.9 | 1.6 |
| draken03-05 | 031031-051207 | 23 | 0.23 | -0.088 | 0.12 | 0.52 | 2.6 | 3.1 | 3.6 |
| drakeav | 031031-051207 | 23 | 0.35 | -0.046 | -0.026 | 0.67 | 1.9 | 2.1 | 2.3 |

 Table A.3: Pressure correlations of GRACE GFZ ($r_{smooth} = 600$ km) with BPRs.

| Location | Span (yymmdd) | No | ρ | $95\%_{low}$ | ρ_{mod} | SNR | σ_{grc} | σ_{BPR} | RMS |
|----------------|---------------|-----|--------|--------------|--------------|-------|----------------|----------------|-----|
| IO1 | 040123-050217 | 36 | 0.59 | 0.19 | 0.036 | 1 | 1.8 | 2.1 | 1.8 |
| IO2 | 040124-050131 | 34 | 0.67 | 0.37 | 0.47 | 1.5 | 1.9 | 1.9 | 1.6 |
| IOav | 040124-050131 | 34 | 0.63 | 0.22 | 0.24 | 1.4 | 1.8 | 1.7 | 1.5 |
| IO1sub | 040301-050217 | 32 | 0.86 | 0.74 | 0.36 | 3.1 | 1.8 | 2 | 1 |
| IO2sub | 040301-050131 | 30 | 0.83 | 0.73 | 0.81 | 3 | 1.8 | 1.7 | 1 |
| IOavsub | 040301-050129 | 30 | 0.92 | 0.87 | 0.68 | 6.7 | 1.8 | 1.5 | 0.7 |
| grace2 | 020516-030516 | 20 | 0.83 | 0.62 | 0.29 | 0.63 | 2 | 4 | 2.5 |
| grace3 | 020517-030517 | 20 | 0.71 | 0.38 | 0.36 | 1.4 | 2.2 | 2.6 | 1.9 |
| graceav | 020516-030516 | 20 | 0.92 | 0.76 | 0.37 | 3 | 2.1 | 2.8 | 1.2 |
| pies1 | 021201-050131 | 68 | 0.66 | 0.48 | 0.24 | 0.67 | 1.8 | 3 | 2.2 |
| pies2 | 021129-050128 | 68 | 0.61 | 0.45 | 0.24 | 0.82 | 1.8 | 2.5 | 2 |
| piesav | 021129-050126 | 68 | 0.72 | 0.58 | 0.28 | 1.2 | 1.8 | 2.4 | 1.6 |
| shag1 | 030505-041117 | 52 | -0.061 | -0.35 | -0.47 | 0.31 | 1.9 | 2.7 | 3.4 |
| shag2 | 030507-041128 | 52 | 0.12 | -0.15 | -0.26 | 0.26 | 1.7 | 3.1 | 3.3 |
| shagav | 030507-041117 | 51 | 0.054 | -0.2 | -0.49 | 0.4 | 1.8 | 2.3 | 2.8 |
| drakes02-05 | 021227-051211 | 100 | -0.044 | -0.23 | -0.36 | 0.35 | 1.5 | 2 | 2.5 |
| drakes02-05sub | 021227-040601 | 44 | 0.25 | -0.025 | -0.39 | 0.47 | 1.6 | 2.1 | 2.3 |
| draken03-05 | 031031-051207 | 74 | -0.059 | -0.27 | -0.31 | 0.15 | 1.4 | 3.1 | 3.6 |
| drakeav | 031031-051207 | 74 | -0.22 | -0.47 | -0.56 | 0.22 | 1.3 | 2.1 | 2.7 |

Table A.4: Pressure correlations of GRACE GRGS ($r_{smooth} = 800$ km) with BPRs.

| Location | Span (yymmdd) | No | ρ | $95\%_{low}$ | ρ_{mod} | SNR | σ_{grc} | σ_{BPR} | RMS |
|----------------|---------------|----|--------|--------------|--------------|-------|----------------|----------------|-----|
| IO1 | 040123-050217 | 12 | 0.58 | 0.2 | 0.2 | 1.4 | 2.9 | 2.3 | 2.4 |
| IO2 | 040124-050131 | 12 | 0.66 | 0.47 | 0.079 | 1.8 | 3.1 | 2 | 2.3 |
| IOav | 040124-050131 | 12 | 0.66 | 0.41 | 0.14 | 1.8 | 3 | 1.8 | 2.3 |
| IO1sub | 040301-050217 | 11 | 0.7 | 0.42 | 0.8 | 2 | 3 | 2.1 | 2.1 |
| IO2sub | 040301-050131 | 11 | 0.71 | 0.53 | 0.54 | 2 | 3.2 | 1.9 | 2.3 |
| IOavsub | 040301-050129 | 10 | 0.73 | 0.41 | 0.83 | 2 | 2.9 | 1.5 | 2.1 |
| grace2 | 020516-030516 | 9 | 0.81 | 0.44 | 0.34 | 0.54 | 1.8 | 3.6 | 2.4 |
| grace3 | 020517-030517 | 9 | 0.47 | -0.36 | -0.27 | 0.55 | 2.2 | 3.2 | 3 |
| graceav | 020516-030516 | 9 | 0.74 | 0.15 | 0.057 | 0.87 | 2 | 3.1 | 2.1 |
| pies1 | 021201-050131 | 24 | 0.63 | 0.37 | 0.22 | 1.6 | 3.5 | 2.7 | 2.8 |
| pies2 | 021129-050128 | 24 | 0.66 | 0.36 | 0.38 | 1.7 | 2.9 | 2.3 | 2.2 |
| piesav | 021129-050126 | 24 | 0.78 | 0.61 | 0.43 | 2.5 | 3.3 | 2.1 | 2.1 |
| shag1 | 030505-041117 | 16 | 0.096 | -0.49 | -0.14 | 0.71 | 3.1 | 2.3 | 3.7 |
| shag2 | 030507-041128 | 16 | 0.21 | -0.38 | 0.087 | 0.63 | 3 | 3 | 3.8 |
| shagav | 030507-041117 | 16 | 0.2 | -0.44 | -0.03 | 0.82 | 3 | 2.1 | 3.3 |
| drakes02-05 | 021227-051211 | 32 | 0.25 | -0.027 | -0.21 | 0.97 | 2.9 | 1.6 | 2.9 |
| drakes02-05sub | 021227-040601 | 16 | 0.38 | 0.02 | -0.21 | 0.98 | 2.4 | 1.8 | 2.4 |
| draken03-05 | 031031-051207 | 22 | 0.065 | -0.33 | -0.31 | 0.48 | 2.7 | 3 | 3.9 |
| drakeav | 031031-051207 | 22 | 0.11 | -0.24 | -0.55 | 0.8 | 2.9 | 1.8 | 3.2 |

Table A.5: Pressure correlations of GRACE CSR ($r_{smooth} = 800$ km) with BPRs.

| Location | Span (yymmdd) | No | ρ | $95\%_{low}$ | ρ_{mod} | SNR | σ_{grc} | σ_{BPR} | RMS |
|----------------|---------------|----|--------|--------------|--------------|-------|----------------|----------------|-----|
| IO1 | 040123-050217 | 12 | 0.62 | -0.23 | 0.31 | 0.97 | 1.8 | 2.3 | 1.8 |
| IO2 | 040124-050131 | 11 | 0.55 | 0.28 | 0.6 | 1 | 1.8 | 2 | 1.8 |
| IOav | 040124-050131 | 11 | 0.6 | -0.17 | 0.44 | 1.3 | 1.8 | 1.8 | 1.6 |
| IO1sub | 040301-050217 | 11 | 0.69 | -0.13 | 0.46 | 1.4 | 1.9 | 2.1 | 1.6 |
| IO2sub | 040301-050131 | 10 | 0.53 | 0.25 | 0.81 | 1.1 | 1.9 | 1.7 | 1.8 |
| IOavsub | 040301-050129 | 10 | 0.66 | -0.14 | 0.7 | 1.7 | 1.9 | 1.5 | 1.4 |
| pies1 | 021201-050131 | 22 | 0.62 | 0.34 | 0.32 | 1 | 2.2 | 2.7 | 2.2 |
| pies2 | 021129-050128 | 21 | 0.69 | 0.39 | 0.47 | 1.1 | 1.9 | 2.4 | 1.8 |
| piesav | 021129-050126 | 21 | 0.78 | 0.56 | 0.57 | 2.2 | 2.1 | 2.2 | 1.4 |
| shag1 | 030505-041117 | 15 | 0.13 | -0.44 | 0.091 | 0.49 | 2 | 2.3 | 2.9 |
| shag2 | 030507-041128 | 15 | 0.17 | -0.35 | -0.37 | 0.4 | 2.1 | 3 | 3.3 |
| shagav | 030507-041117 | 15 | 0.17 | -0.47 | -0.23 | 0.58 | 2.1 | 2.2 | 2.8 |
| drakes02-05 | 021227-051211 | 32 | 0.56 | -0.024 | 0.25 | 0.93 | 1.6 | 1.9 | 1.7 |
| drakes02-05sub | 021227-040601 | 14 | 0.66 | -0.064 | 0.39 | 1.3 | 1.6 | 1.9 | 1.4 |
| draken03-05 | 031031-051207 | 23 | 0.19 | -0.18 | -0.009 | 0.34 | 1.9 | 3.1 | 3.3 |
| drakeav | 031031-051207 | 23 | 0.32 | -0.12 | -0.045 | 0.57 | 1.7 | 2.1 | 2.3 |

Table A.6: Pressure correlations of GRACE GFZ ($r_{smooth} = 800$ km) with BPRs.

| Location | Span (yymmdd) | No | ρ | $95\%_{low}$ | ρ_{mod} | SNR | σ_{grc} | σ_{BPR} | RMS |
|----------------|---------------|-----|--------|--------------|--------------|-------|----------------|----------------|------|
| IO1 | 040123-050217 | 36 | 0.57 | 0.17 | -0.002 | 0.91 | 1.7 | 2.1 | 1.8 |
| IO2 | 040124-050131 | 34 | 0.65 | 0.33 | 0.45 | 1.3 | 1.8 | 1.9 | 1.6 |
| IOav | 040124-050131 | 34 | 0.61 | 0.19 | 0.21 | 1.3 | 1.7 | 1.7 | 1.5 |
| IO1sub | 040301-050217 | 32 | 0.85 | 0.72 | 0.34 | 2.6 | 1.7 | 2 | 1 |
| IO2sub | 040301-050131 | 30 | 0.82 | 0.72 | 0.8 | 2.6 | 1.7 | 1.7 | 1 |
| IOavsub | 040301-050129 | 30 | 0.92 | 0.86 | 0.66 | 6.4 | 1.7 | 1.5 | 0.67 |
| grace2 | 020516-030516 | 20 | 0.85 | 0.67 | 0.38 | 0.42 | 1.7 | 4 | 2.6 |
| grace3 | 020517-030517 | 20 | 0.7 | 0.36 | 0.44 | 1 | 1.9 | 2.6 | 1.9 |
| graceav | 020516-030516 | 20 | 0.93 | 0.8 | 0.48 | 1.9 | 1.8 | 2.8 | 1.3 |
| pies1 | 021201-050131 | 68 | 0.65 | 0.48 | 0.2 | 0.57 | 1.7 | 3 | 2.3 |
| pies2 | 021129-050128 | 68 | 0.6 | 0.44 | 0.23 | 0.72 | 1.7 | 2.5 | 2 |
| piesav | 021129-050126 | 68 | 0.72 | 0.58 | 0.25 | 1.1 | 1.7 | 2.4 | 1.6 |
| shag1 | 030505-041117 | 52 | -0.085 | -0.38 | -0.5 | 0.28 | 1.8 | 2.7 | 3.4 |
| shag2 | 030507-041128 | 52 | 0.096 | -0.19 | -0.32 | 0.23 | 1.6 | 3.1 | 3.3 |
| shagav | 030507-041117 | 51 | 0.018 | -0.24 | -0.53 | 0.36 | 1.7 | 2.3 | 2.8 |
| drakes02-05 | 021227-051211 | 100 | -0.08 | -0.27 | -0.38 | 0.32 | 1.4 | 2 | 2.5 |
| drakes02-05sub | 021227-040601 | 44 | 0.21 | -0.066 | -0.4 | 0.4 | 1.4 | 2.1 | 2.2 |
| draken03-05 | 031031-051207 | 74 | -0.13 | -0.34 | -0.35 | 0.13 | 1.3 | 3.1 | 3.6 |
| drakeav | 031031-051207 | 74 | -0.29 | -0.52 | -0.58 | 0.2 | 1.2 | 2.1 | 2.7 |

Table A.7: Pressure correlations of GRACE GRGS ($r_{smooth} = 1000$ km) with BPRs.

| Location | Span (yymmdd) | No | ρ | $95\%_{low}$ | ρ_{mod} | SNR | σ_{grc} | σ_{BPR} | RMS |
|----------------|---------------|----|--------|--------------|--------------|-------|----------------|----------------|-----|
| IO1 | 040123-050217 | 12 | 0.56 | 0.21 | 0.19 | 1.3 | 2.6 | 2.3 | 2.3 |
| IO2 | 040124-050131 | 12 | 0.66 | 0.47 | 0.067 | 1.8 | 2.8 | 2 | 2.1 |
| IOav | 040124-050131 | 12 | 0.66 | 0.4 | 0.13 | 1.8 | 2.7 | 1.8 | 2 |
| IO1sub | 040301-050217 | 11 | 0.68 | 0.38 | 0.8 | 1.9 | 2.7 | 2.1 | 2 |
| IO2sub | 040301-050131 | 11 | 0.7 | 0.51 | 0.53 | 2 | 2.9 | 1.9 | 2.1 |
| IOavsub | 040301-050129 | 10 | 0.71 | 0.35 | 0.82 | 2 | 2.5 | 1.5 | 1.8 |
| grace2 | 020516-030516 | 9 | 0.79 | 0.38 | 0.38 | 0.45 | 1.7 | 3.6 | 2.5 |
| grace3 | 020517-030517 | 9 | 0.39 | -0.5 | -0.24 | 0.42 | 2 | 3.2 | 3.1 |
| graceav | 020516-030516 | 9 | 0.68 | 0.011 | 0.11 | 0.65 | 1.8 | 3.1 | 2.2 |
| pies1 | 021201-050131 | 24 | 0.61 | 0.34 | 0.21 | 1.5 | 3.3 | 2.7 | 2.7 |
| pies2 | 021129-050128 | 24 | 0.66 | 0.37 | 0.38 | 1.7 | 2.8 | 2.3 | 2.2 |
| piesav | 021129-050126 | 24 | 0.77 | 0.59 | 0.42 | 2.4 | 3.1 | 2.1 | 2 |
| shag1 | 030505-041117 | 16 | 0.093 | -0.49 | -0.19 | 0.7 | 3 | 2.3 | 3.6 |
| shag2 | 030507-041128 | 16 | 0.2 | -0.39 | 0.049 | 0.62 | 3 | 3 | 3.8 |
| shagav | 030507-041117 | 16 | 0.19 | -0.45 | -0.079 | 0.81 | 3 | 2.1 | 3.3 |
| drakes02-05 | 021227-051211 | 32 | 0.25 | -0.015 | -0.2 | 0.96 | 2.8 | 1.6 | 2.9 |
| drakes02-05sub | 021227-040601 | 16 | 0.38 | 0.002 | -0.22 | 0.95 | 2.3 | 1.8 | 2.4 |
| draken03-05 | 031031-051207 | 22 | 0.001 | -0.38 | -0.34 | 0.42 | 2.6 | 3 | 4 |
| drakeav | 031031-051207 | 22 | 0.078 | -0.26 | -0.56 | 0.76 | 2.8 | 1.8 | 3.2 |

Table A.8: Pressure correlations of GRACE CSR ($r_{smooth} = 1000$ km) with BPRs.

| Location | Span (yymmdd) | No | ρ | $95\%_{low}$ | ρ_{mod} | SNR | σ_{grc} | σ_{BPR} | RMS |
|----------------|---------------|----|--------|--------------|--------------|-------|----------------|----------------|-----|
| IO1 | 040123-050217 | 12 | 0.62 | -0.22 | 0.33 | 0.95 | 1.8 | 2.3 | 1.8 |
| IO2 | 040124-050131 | 11 | 0.51 | 0.11 | 0.61 | 0.92 | 1.8 | 2 | 1.9 |
| IOav | 040124-050131 | 11 | 0.59 | -0.2 | 0.45 | 1.2 | 1.8 | 1.8 | 1.7 |
| IO1sub | 040301-050217 | 11 | 0.67 | -0.17 | 0.48 | 1.2 | 1.9 | 2.1 | 1.7 |
| IO2sub | 040301-050131 | 10 | 0.48 | 0.084 | 0.81 | 1 | 1.9 | 1.7 | 1.9 |
| IOavsub | 040301-050129 | 10 | 0.64 | -0.24 | 0.72 | 1.6 | 1.9 | 1.5 | 1.5 |
| pies1 | 021201-050131 | 22 | 0.64 | 0.33 | 0.35 | 0.88 | 2 | 2.7 | 2.1 |
| pies2 | 021129-050128 | 21 | 0.67 | 0.37 | 0.48 | 0.97 | 1.8 | 2.4 | 1.8 |
| piesav | 021129-050126 | 21 | 0.78 | 0.54 | 0.59 | 1.9 | 1.9 | 2.2 | 1.4 |
| shag1 | 030505-041117 | 15 | 0.32 | -0.23 | 0.059 | 0.67 | 2.1 | 2.3 | 2.6 |
| shag2 | 030507-041128 | 15 | 0.19 | -0.44 | -0.35 | 0.41 | 2.1 | 3 | 3.3 |
| shagav | 030507-041117 | 15 | 0.29 | -0.37 | -0.23 | 0.71 | 2.1 | 2.2 | 2.5 |
| drakes02-05 | 021227-051211 | 32 | 0.58 | -0.007 | 0.26 | 0.82 | 1.4 | 1.9 | 1.5 |
| drakes02-05sub | 021227-040601 | 14 | 0.71 | -0.034 | 0.43 | 1.2 | 1.4 | 1.9 | 1.3 |
| draken03-05 | 031031-051207 | 23 | 0.14 | -0.26 | -0.07 | 0.19 | 1.4 | 3.1 | 3.2 |
| drakeav | 031031-051207 | 23 | 0.3 | -0.19 | -0.056 | 0.41 | 1.4 | 2.1 | 2.2 |

Table A.9: Pressure correlations of GRACE GFZ ($r_{smooth} = 1000$ km) with BPRs.

A.2 Geostrophic Flow

Below one finds the correlations tables for the geostrophic flow, denoted with ‘geo’. The standard deviations and RMS values are in mm per second except for the location names which contain ‘dif’. Those series are obtained by calculating the GRACE geostrophic flow from bottom pressure differences between the two BPR positions equivalently to the way the local records are used to derive the geostrophic flow. Consequently the standard deviation and RMS is given as the difference in equivalent water height (cm). The location name ‘shaggeo-s’ is a solution which is obtained from taking the southward component of the GRACE solution only.

| Location | Span (yyymmdd) | No | ρ | 95% _{low} | ρ_{mod} | SNR | σ_{grc} | σ_{BPR} | RMS |
|-------------|----------------|----|--------|--------------------|--------------|-------|----------------|----------------|-----|
| IOgeosub | 040301-050129 | 30 | 0.73 | 0.33 | 0.47 | 1.8 | 4.3 | 1.9 | 3.2 |
| IOgeo | 040124-050131 | 34 | 0.68 | 0.35 | 0.51 | 1.5 | 5.4 | 1.9 | 4.4 |
| IODif | 040124-050131 | 34 | 0.67 | 0.3 | 0.47 | 1.6 | 2.5 | 1 | 2 |
| gracegeo | 020516-030516 | 20 | -0.42 | -0.74 | -0.087 | 0.67 | 11 | 4.5 | 14 |
| gracedif | 020516-030516 | 20 | -0.41 | -0.74 | -0.077 | 0.63 | 4 | 1.9 | 5 |
| piesgeo | 021129-050126 | 68 | 0.18 | -0.049 | 0.11 | 0.98 | 4.2 | 1.8 | 4.2 |
| piesdif | 021129-050126 | 68 | 0.21 | -0.02 | 0.18 | 0.94 | 2.6 | 1.4 | 2.7 |
| shaggeo | 030507-041117 | 51 | 0.26 | -0.065 | 0.6 | 0.034 | 1.7 | 9.6 | 9.3 |
| shaggeo-s | 030507-041117 | 51 | 0.38 | 0.072 | 0.62 | 0.039 | 1.8 | 9.6 | 9 |
| shagdif | 030507-041117 | 51 | 0.24 | -0.084 | 0.61 | 0.035 | 0.3 | 1.8 | 1.6 |
| drakegeo | 021227-050202 | 68 | 0.49 | 0.34 | 0.65 | 1.1 | 2.3 | 1.9 | 2.1 |
| drakedif | 021227-050202 | 68 | 0.47 | 0.3 | 0.6 | 1.1 | 2.1 | 1.6 | 2 |
| drakegeosub | 030201-040801 | 50 | 0.55 | 0.38 | 0.72 | 1.3 | 2.4 | 2 | 2.1 |

Table A.10: Velocity correlations of GRACE GRGS ($r_{smooth} = 400$ km) with BPRs.

| Location | Span (yyymmdd) | No | ρ | 95% _{low} | ρ_{mod} | SNR | σ_{grc} | σ_{BPR} | RMS |
|-------------|----------------|----|--------|--------------------|--------------|------|----------------|----------------|-----|
| IOgeosub | 040301-050129 | 10 | 0.47 | -0.52 | 0.62 | 1.3 | 4.8 | 2.3 | 4.2 |
| IOgeo | 040124-050131 | 12 | 0.39 | -0.57 | 0.48 | 1.2 | 4.6 | 2.1 | 4.3 |
| IODif | 040124-050131 | 12 | 0.34 | -0.58 | 0.46 | 1.1 | 2.4 | 1.1 | 2.3 |
| gracegeo | 020516-030516 | 9 | -0.22 | -0.94 | -0.14 | 0.79 | 11 | 3.6 | 12 |
| gracedif | 020516-030516 | 9 | 0.1 | -0.88 | -0.1 | 0.97 | 4.9 | 1.5 | 5 |
| piesgeo | 021129-050126 | 24 | 0.081 | -0.22 | 0.074 | 0.92 | 4.7 | 1.8 | 4.9 |
| piesdif | 021129-050126 | 24 | 0.071 | -0.23 | 0.11 | 0.92 | 3.9 | 1.4 | 4.1 |
| shaggeo | 030507-041117 | 16 | 0.18 | -0.45 | 0.72 | 0.22 | 4.1 | 8.5 | 8.7 |
| shaggeo-s | 030507-041117 | 16 | 0.23 | -0.4 | 0.73 | 0.23 | 4.1 | 8.5 | 8.6 |
| shagdif | 030507-041117 | 16 | 0.26 | -0.43 | 0.72 | 0.21 | 0.7 | 1.6 | 1.5 |
| drakegeo | 021227-050202 | 24 | 0.064 | -0.35 | 0.73 | 0.93 | 5.4 | 1.9 | 5.6 |
| drakedif | 021227-050202 | 24 | 0.21 | -0.22 | 0.68 | 1 | 3.9 | 1.6 | 3.9 |
| drakegeosub | 030201-040801 | 17 | 0.25 | -0.31 | 0.79 | 1 | 4.2 | 1.9 | 4.1 |

Table A.11: Velocity correlations of GRACE CSR ($r_{smooth} = 400$ km) with BPRs.

| Location | Span (yyymmdd) | No | ρ | 95% _{low} | ρ_{mod} | SNR | σ_{grc} | σ_{BPR} | RMS |
|-------------|----------------|----|--------|--------------------|--------------|------|----------------|----------------|-----|
| IOgeosub | 040301-050129 | 10 | 0.63 | 0.17 | 0.64 | 1.4 | 6.7 | 2.3 | 5.6 |
| IOgeo | 040124-050131 | 11 | 0.61 | 0.13 | 0.64 | 1.4 | 6.5 | 2.2 | 5.5 |
| IODif | 040124-050131 | 11 | 0.6 | 0.13 | 0.62 | 1.5 | 2.7 | 1.2 | 2.2 |
| piesgeo | 021129-050126 | 21 | 0.093 | -0.34 | 0.059 | 0.98 | 6.2 | 1.6 | 6.3 |
| piesdif | 021129-050126 | 21 | 0.15 | -0.32 | 0.056 | 1 | 4.3 | 1.3 | 4.3 |
| shaggeo | 030507-041117 | 15 | 0.27 | 0.018 | 0.67 | 0.41 | 5.8 | 8.8 | 9.1 |
| shaggeo-s | 030507-041117 | 15 | 0.3 | 0.076 | 0.7 | 0.43 | 5.9 | 8.8 | 9 |
| shagdif | 030507-041117 | 15 | 0.28 | 0.011 | 0.67 | 0.44 | 1.2 | 1.7 | 1.8 |
| drakegeo | 021227-050202 | 22 | 0.21 | 0.009 | 0.75 | 1 | 10 | 1.9 | 10 |
| drakedif | 021227-050202 | 22 | 0.28 | 0.056 | 0.72 | 1.1 | 6.7 | 1.6 | 6.4 |
| drakegeosub | 030201-040801 | 15 | 0.57 | 0.3 | 0.77 | 1.5 | 2.9 | 1.8 | 2.4 |

Table A.12: Velocity correlations of GRACE GFZ ($r_{smooth} = 400$ km) with BPRs.

| Location | Span (yymmdd) | No | ρ | $95\%_{low}$ | ρ_{mod} | SNR | σ_{grc} | σ_{BPR} | RMS |
|-------------|---------------|----|--------|--------------|--------------|-------|----------------|----------------|------|
| IOgeosub | 040301-050129 | 30 | 0.85 | 0.67 | 0.47 | 2.9 | 1.7 | 1.9 | 0.97 |
| IOgeo | 040124-050131 | 34 | 0.8 | 0.57 | 0.51 | 2.6 | 2 | 1.9 | 1.2 |
| IODif | 040124-050131 | 34 | 0.77 | 0.52 | 0.47 | 2.2 | 1 | 1 | 0.67 |
| gracegeo | 020516-030516 | 20 | -0.31 | -0.7 | -0.073 | 0.14 | 2.1 | 4.5 | 5.5 |
| gracedif | 020516-030516 | 20 | -0.29 | -0.68 | -0.11 | 0.13 | 0.8 | 1.9 | 2.2 |
| piesgeo | 021129-050126 | 68 | 0.38 | 0.19 | 0.1 | 0.58 | 1.3 | 1.8 | 1.8 |
| piesdif | 021129-050126 | 68 | 0.35 | 0.17 | 0.17 | 0.54 | 1 | 1.4 | 1.4 |
| shaggeo | 030507-041117 | 51 | 0.3 | -0.046 | 0.55 | 0.015 | 1.1 | 9.6 | 9.3 |
| shaggeo-s | 030507-041117 | 51 | 0.43 | 0.13 | 0.57 | 0.015 | 1.1 | 9.6 | 9.1 |
| shagdif | 030507-041117 | 51 | 0.26 | -0.081 | 0.56 | 0.016 | 0.2 | 1.8 | 1.6 |
| drakegeo | 021227-050202 | 68 | 0.39 | 0.2 | 0.59 | 0.6 | 1.5 | 1.9 | 1.9 |
| drakedif | 021227-050202 | 68 | 0.38 | 0.18 | 0.56 | 0.76 | 1.5 | 1.6 | 1.7 |
| drakegeosub | 030201-040801 | 50 | 0.52 | 0.32 | 0.67 | 0.74 | 1.5 | 2 | 1.8 |

 Table A.13: Velocity correlations of GRACE GRGS ($r_{smooth} = 600$ km) with BPRs.

| Location | Span (yymmdd) | No | ρ | $95\%_{low}$ | ρ_{mod} | SNR | σ_{grc} | σ_{BPR} | RMS |
|-------------|---------------|----|--------|--------------|--------------|-------|----------------|----------------|-----|
| IOgeosub | 040301-050129 | 10 | 0.69 | -0.19 | 0.64 | 1.9 | 2.9 | 2.3 | 2.1 |
| IOgeo | 040124-050131 | 12 | 0.6 | -0.3 | 0.48 | 1.5 | 2.8 | 2.1 | 2.2 |
| IODif | 040124-050131 | 12 | 0.61 | -0.26 | 0.46 | 1.6 | 1.6 | 1.1 | 1.3 |
| gracegeo | 020516-030516 | 9 | -0.34 | -0.9 | -0.18 | 0.23 | 2.4 | 3.6 | 5 |
| gracedif | 020516-030516 | 9 | -0.34 | -0.9 | -0.17 | 0.24 | 1 | 1.5 | 2.1 |
| piesgeo | 021129-050126 | 24 | 0.27 | -0.13 | 0.082 | 0.74 | 1.9 | 1.8 | 2.3 |
| piesdif | 021129-050126 | 24 | 0.2 | -0.19 | 0.12 | 0.69 | 1.6 | 1.4 | 1.9 |
| shaggeo | 030507-041117 | 16 | 0.071 | -0.54 | 0.65 | 0.043 | 1.8 | 8.5 | 8.6 |
| shaggeo-s | 030507-041117 | 16 | 0.16 | -0.49 | 0.67 | 0.048 | 1.8 | 8.5 | 8.4 |
| shagdif | 030507-041117 | 16 | 0.035 | -0.55 | 0.64 | 0.048 | 0.4 | 1.6 | 1.8 |
| drakegeo | 021227-050202 | 24 | 0.34 | -0.14 | 0.63 | 0.74 | 1.8 | 1.9 | 2.1 |
| drakedif | 021227-050202 | 24 | 0.44 | -0.011 | 0.62 | 1 | 1.8 | 1.6 | 1.8 |
| drakegeosub | 030201-040801 | 17 | 0.59 | 0.29 | 0.67 | 1 | 1.6 | 1.9 | 1.6 |

 Table A.14: Velocity correlations of GRACE CSR ($r_{smooth} = 600$ km) with BPRs.

| Location | Span (yymmdd) | No | ρ | $95\%_{low}$ | ρ_{mod} | SNR | σ_{grc} | σ_{BPR} | RMS |
|-------------|---------------|----|--------|--------------|--------------|------|----------------|----------------|------|
| IOgeosub | 040301-050129 | 10 | 0.72 | -0.26 | 0.65 | 1.4 | 1.9 | 2.3 | 1.6 |
| IOgeo | 040124-050131 | 11 | 0.68 | -0.29 | 0.65 | 1.3 | 1.9 | 2.2 | 1.7 |
| IODif | 040124-050131 | 11 | 0.65 | -0.33 | 0.62 | 1.3 | 1.1 | 1.2 | 0.98 |
| piesgeo | 021129-050126 | 21 | 0.16 | -0.21 | 0.028 | 0.6 | 1.6 | 1.6 | 2.1 |
| piesdif | 021129-050126 | 21 | 0.062 | -0.3 | 0.046 | 0.54 | 1.3 | 1.3 | 1.8 |
| shaggeo | 030507-041117 | 15 | 0.28 | 0.037 | 0.63 | 0.21 | 3.9 | 8.8 | 8.5 |
| shaggeo-s | 030507-041117 | 15 | 0.33 | 0.094 | 0.67 | 0.21 | 3.9 | 8.8 | 8.3 |
| shagdif | 030507-041117 | 15 | 0.28 | 0.027 | 0.62 | 0.21 | 0.7 | 1.7 | 1.5 |
| drakegeo | 021227-050202 | 22 | 0.34 | 0.1 | 0.7 | 1.1 | 3.4 | 1.9 | 3.3 |
| drakedif | 021227-050202 | 22 | 0.38 | 0.1 | 0.67 | 1.1 | 3 | 1.6 | 2.8 |
| drakegeosub | 030201-040801 | 15 | 0.66 | 0.39 | 0.73 | 1.4 | 1.8 | 1.8 | 1.5 |

 Table A.15: Velocity correlations of GRACE GFZ ($r_{smooth} = 600$ km) with BPRs.

| Location | Span (yymmdd) | No | ρ | $95\%_{low}$ | ρ_{mod} | SNR | σ_{grc} | σ_{BPR} | RMS |
|-------------|---------------|----|--------|--------------|--------------|-------|----------------|----------------|------|
| IOgeosub | 040301-050129 | 30 | 0.81 | 0.64 | 0.49 | 1.3 | 1.3 | 1.9 | 1.1 |
| IOgeo | 040124-050131 | 34 | 0.78 | 0.55 | 0.53 | 1.5 | 1.4 | 1.9 | 1.2 |
| IODif | 040124-050131 | 34 | 0.76 | 0.52 | 0.49 | 1.4 | 0.8 | 1 | 0.68 |
| gracegeo | 020516-030516 | 20 | -0.073 | -0.51 | -0.26 | 0.035 | 0.87 | 4.5 | 4.7 |
| gracedif | 020516-030516 | 20 | -0.1 | -0.53 | -0.34 | 0.038 | 0.4 | 1.9 | 2.1 |
| piesgeo | 021129-050126 | 68 | 0.28 | 0.088 | 0.083 | 0.38 | 1.1 | 1.8 | 1.8 |
| piesdif | 021129-050126 | 68 | 0.25 | 0.067 | 0.14 | 0.41 | 0.9 | 1.4 | 1.4 |
| shaggeo | 030507-041117 | 51 | 0.28 | -0.068 | 0.46 | 0.013 | 1.1 | 9.6 | 9.5 |
| shaggeo-s | 030507-041117 | 51 | 0.38 | 0.064 | 0.49 | 0.013 | 1 | 9.6 | 9.1 |
| shagdif | 030507-041117 | 51 | 0.25 | -0.1 | 0.47 | 0.014 | 0.2 | 1.8 | 1.7 |
| drakegeo | 021227-050202 | 68 | 0.29 | 0.073 | 0.52 | 0.35 | 1.1 | 1.9 | 1.9 |
| drakedif | 021227-050202 | 68 | 0.33 | 0.11 | 0.51 | 0.55 | 1.2 | 1.6 | 1.6 |
| drakegeosub | 030201-040801 | 50 | 0.44 | 0.19 | 0.59 | 0.38 | 1.1 | 2 | 1.8 |

 Table A.16: Velocity correlations of GRACE GRGS ($r_{smooth} = 800$ km) with BPRs.

| Location | Span (yymmdd) | No | ρ | $95\%_{low}$ | ρ_{mod} | SNR | σ_{grc} | σ_{BPR} | RMS |
|-------------|---------------|----|--------|--------------|--------------|-------|----------------|----------------|-----|
| IOgeosub | 040301-050129 | 10 | 0.75 | 0.044 | 0.67 | 1.6 | 2 | 2.3 | 1.5 |
| IOgeo | 040124-050131 | 12 | 0.66 | -0.14 | 0.5 | 1.3 | 1.9 | 2.1 | 1.7 |
| IODif | 040124-050131 | 12 | 0.67 | -0.1 | 0.47 | 1.5 | 1.1 | 1.1 | 0.9 |
| gracegeo | 020516-030516 | 9 | -0.32 | -0.87 | -0.54 | 0.15 | 1.7 | 3.6 | 4.5 |
| gracedif | 020516-030516 | 9 | -0.33 | -0.88 | -0.59 | 0.15 | 0.7 | 1.5 | 1.8 |
| piesgeo | 021129-050126 | 24 | 0.26 | -0.15 | 0.099 | 0.39 | 1.2 | 1.8 | 1.9 |
| piesdif | 021129-050126 | 24 | 0.15 | -0.2 | 0.13 | 0.47 | 1.2 | 1.4 | 1.8 |
| shaggeo | 030507-041117 | 16 | 0.084 | -0.5 | 0.44 | 0.028 | 1.4 | 8.5 | 8.5 |
| shaggeo-s | 030507-041117 | 16 | 0.18 | -0.43 | 0.46 | 0.028 | 1.4 | 8.5 | 8.4 |
| shagdif | 030507-041117 | 16 | 0.033 | -0.52 | 0.41 | 0.031 | 0.3 | 1.6 | 1.7 |
| drakegeo | 021227-050202 | 24 | 0.44 | -0.064 | 0.37 | 0.35 | 1 | 1.9 | 1.7 |
| drakedif | 021227-050202 | 24 | 0.49 | 0.05 | 0.55 | 0.77 | 1.3 | 1.6 | 1.5 |
| drakegeosub | 030201-040801 | 17 | 0.73 | 0.47 | 0.41 | 0.49 | 0.97 | 1.9 | 1.4 |

 Table A.17: Velocity correlations of GRACE CSR ($r_{smooth} = 800$ km) with BPRs.

| Location | Span (yymmdd) | No | ρ | $95\%_{low}$ | ρ_{mod} | SNR | σ_{grc} | σ_{BPR} | RMS |
|-------------|---------------|----|--------|--------------|--------------|-------|----------------|----------------|------|
| IOgeosub | 040301-050129 | 10 | 0.71 | -0.14 | 0.68 | 1 | 1.6 | 2.3 | 1.6 |
| IOgeo | 040124-050131 | 11 | 0.67 | -0.25 | 0.68 | 0.97 | 1.6 | 2.2 | 1.6 |
| IODif | 040124-050131 | 11 | 0.66 | -0.27 | 0.65 | 1 | 0.9 | 1.2 | 0.89 |
| piesgeo | 021129-050126 | 21 | 0.024 | -0.38 | 0.027 | 0.26 | 0.94 | 1.6 | 1.9 |
| piesdif | 021129-050126 | 21 | -0.069 | -0.47 | 0.054 | 0.31 | 0.9 | 1.3 | 1.6 |
| shaggeo | 030507-041117 | 15 | 0.35 | 0.065 | 0.54 | 0.063 | 2.1 | 8.8 | 8.2 |
| shaggeo-s | 030507-041117 | 15 | 0.43 | 0.15 | 0.57 | 0.064 | 2 | 8.8 | 8.1 |
| shagdif | 030507-041117 | 15 | 0.33 | 0.041 | 0.52 | 0.063 | 0.4 | 1.7 | 1.6 |
| drakegeo | 021227-050202 | 22 | 0.42 | 0.1 | 0.62 | 0.72 | 1.7 | 1.9 | 1.9 |
| drakedif | 021227-050202 | 22 | 0.44 | 0.097 | 0.63 | 0.97 | 1.8 | 1.6 | 1.8 |
| drakegeosub | 030201-040801 | 15 | 0.6 | 0.23 | 0.67 | 0.65 | 1.2 | 1.8 | 1.4 |

 Table A.18: Velocity correlations of GRACE GFZ ($r_{smooth} = 800$ km) with BPRs.

Appendix B

Time series of GRACE (CSR, GFZ) and in situ records

B.1 Bottom Pressure Series

This section contains the time series of the CSR and GFZ GRACE series plotted together with the local bottom pressure series. The plots show the averaged time series for the individual locations and the mean of neighboring locations. The green line represents the model values (GAC product). Plots of the GRGS solution can be found within the main text in chapter 5. An exception is the Drake passage plot. Here the GRGS solution is given and the GFZ version appears in the text. All plots hold for a GRACE smoothing radius of 800 km.

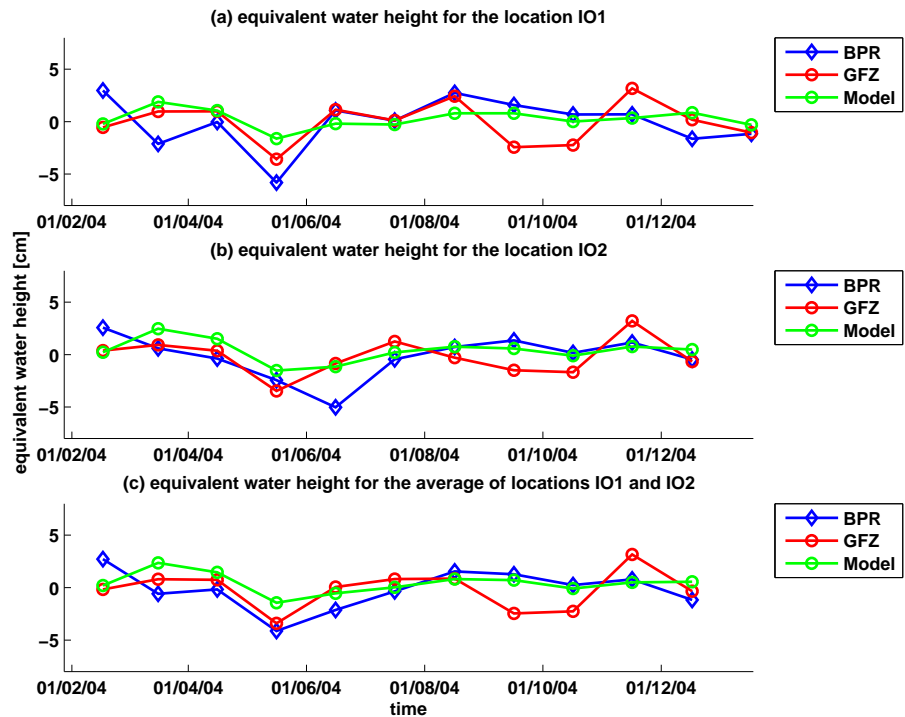


Figure B.1: Time series of the in situ records near Crozet and GRACE (GFZ).

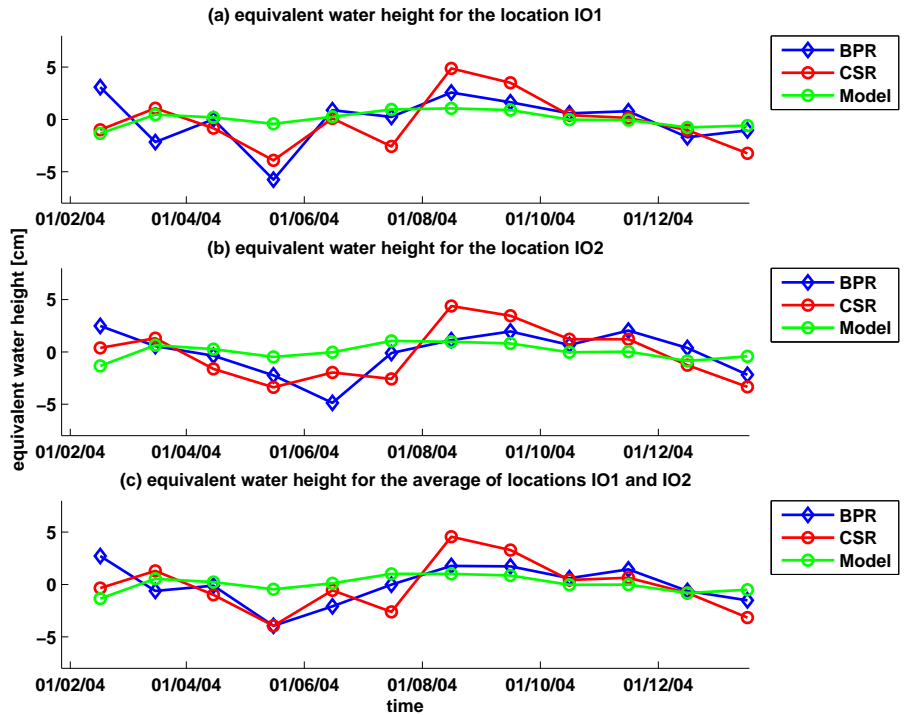


Figure B.2: Time series of the in situ records near Crozet and GRACE (CSR).

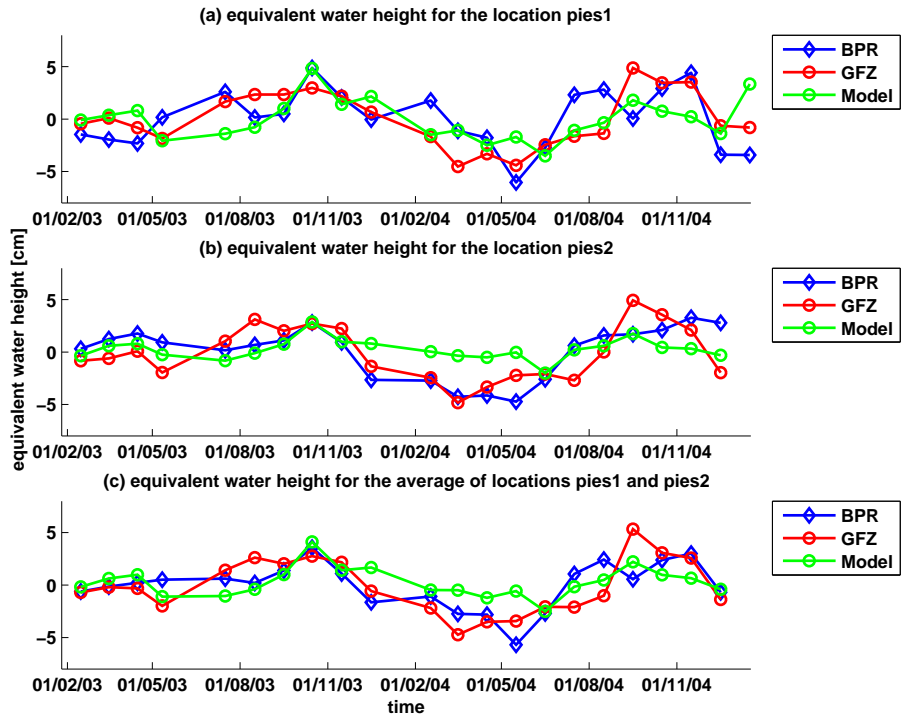


Figure B.3: Time series of the in situ records in the South Atlantic and GRACE (GFZ).

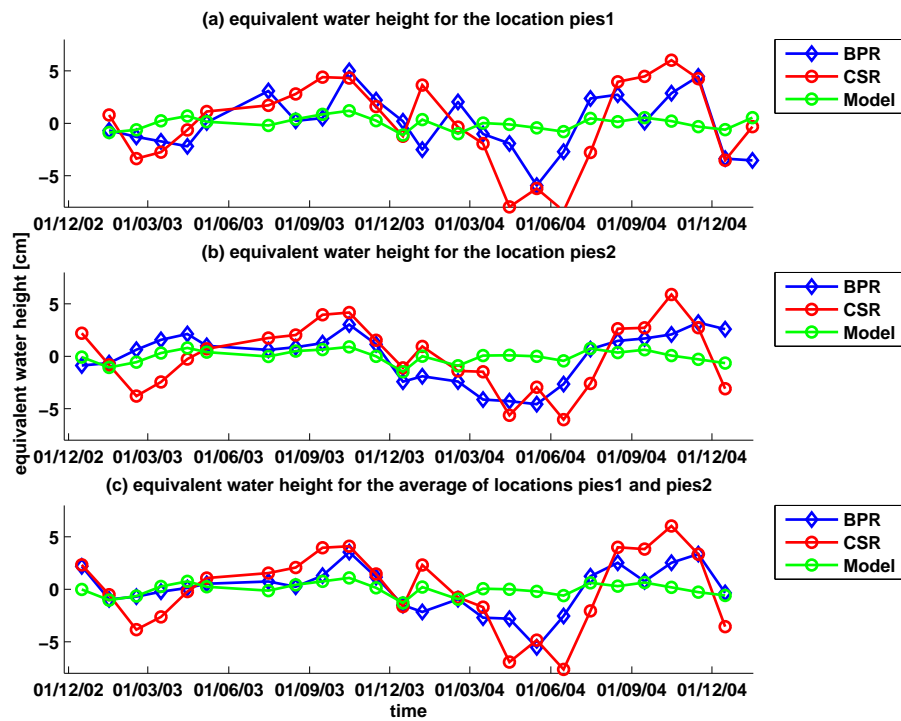


Figure B.4: Time series of the in situ records in the South Atlantic and GRACE (CSR).

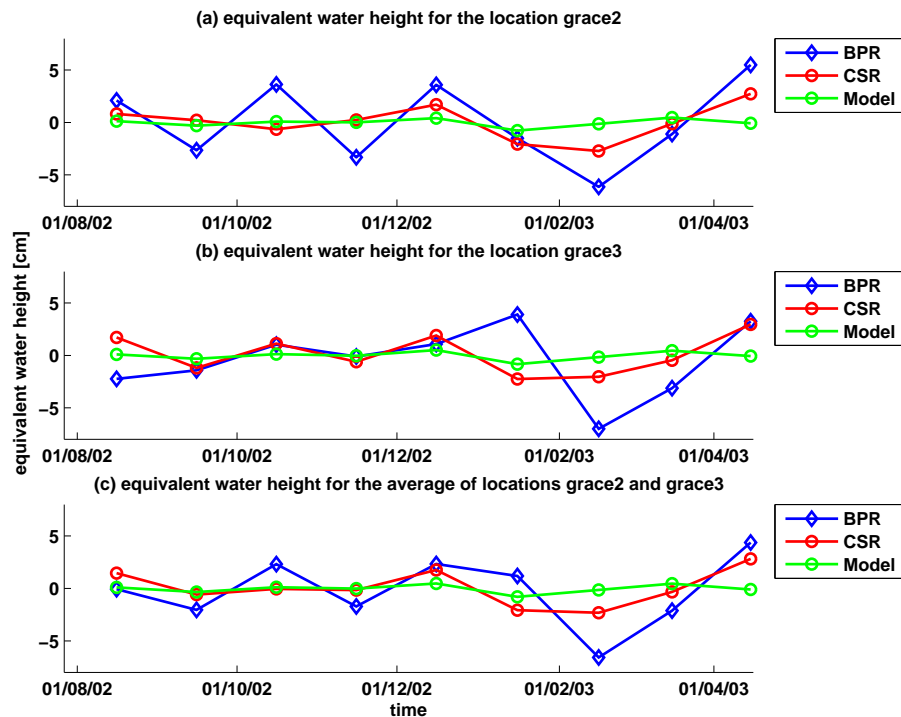


Figure B.5: Time series of the in situ records in the Argentine Basin and GRACE (CSR).

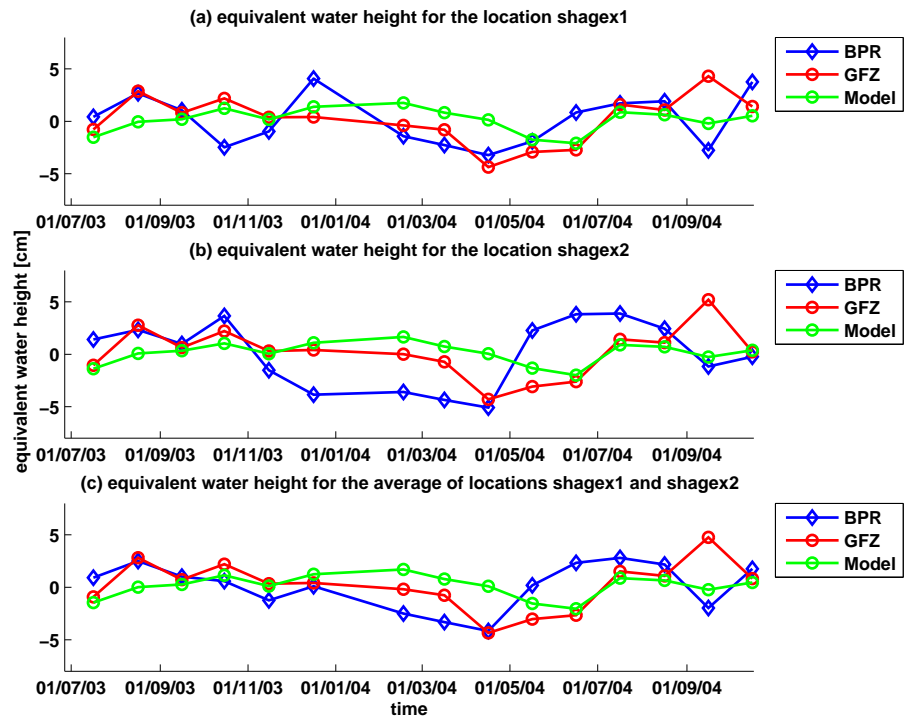


Figure B.6: Time series of the in situ records near Shags Rock and GRACE (GFZ).

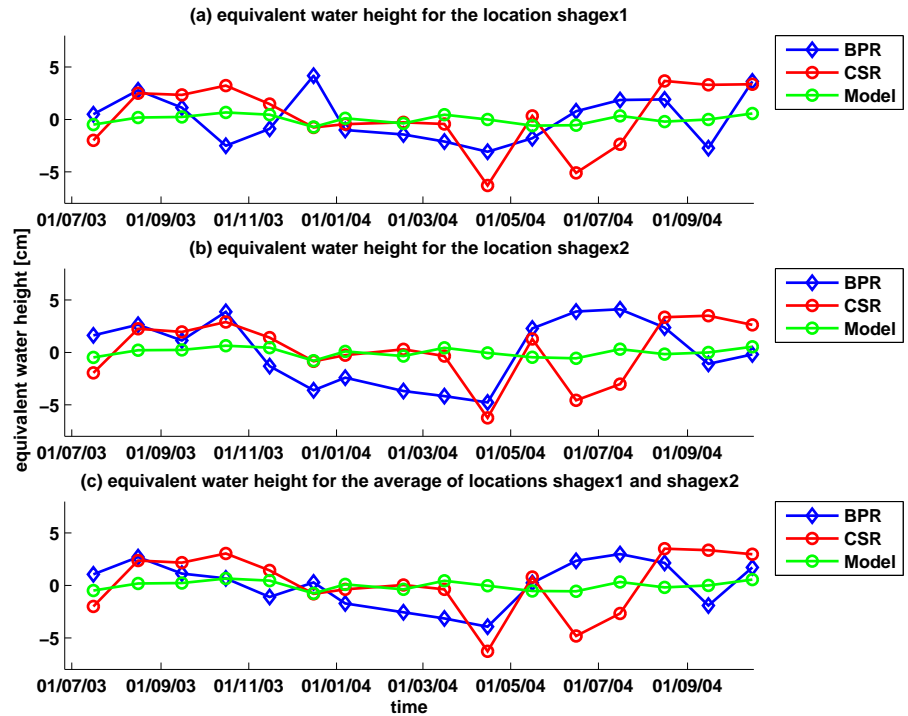


Figure B.7: Time series of the in situ records near Shags Rock and GRACE (CSR).

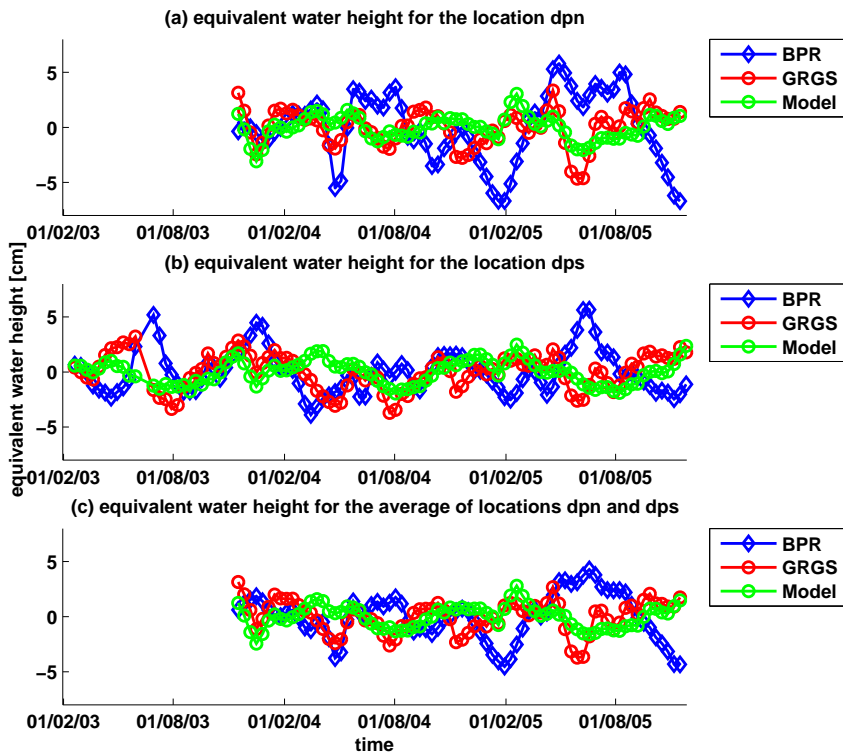


Figure B.8: Time series of the in situ records in the Drake passage and GRACE (GRGS).

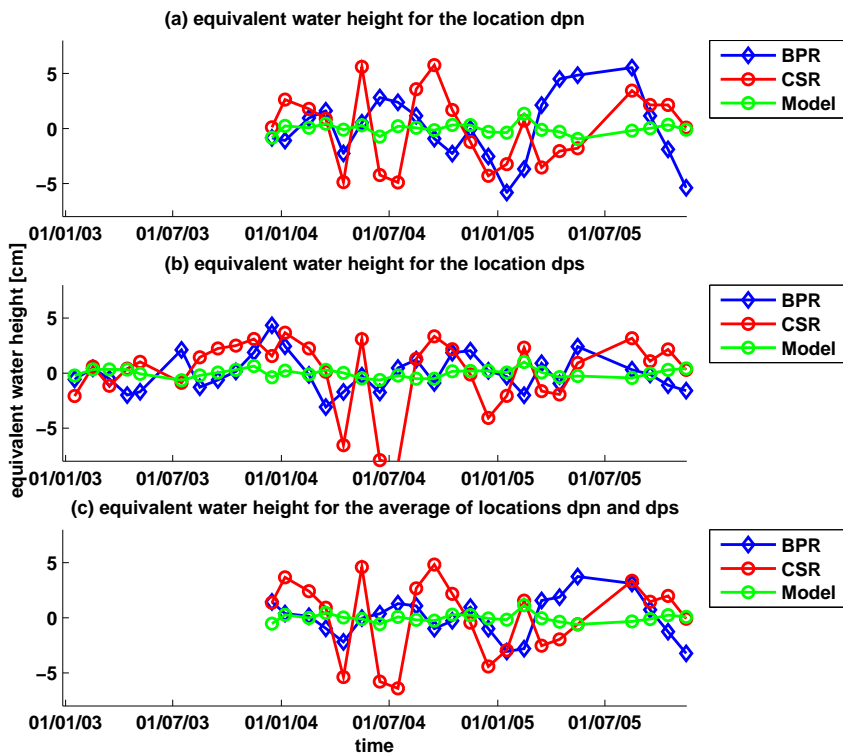


Figure B.9: Time series of the in situ records in the Drake passage and GRACE (CSR).

B.2 Geostrophic Transport series

The plots below depict some time series of the geostrophic transport variations obtained from the BPR recorders and from the GRACE solutions. The geostrophic transport of GRACE was obtained by calculating the eastward and southward component and decomposing them according to the positions of the BPR stations.

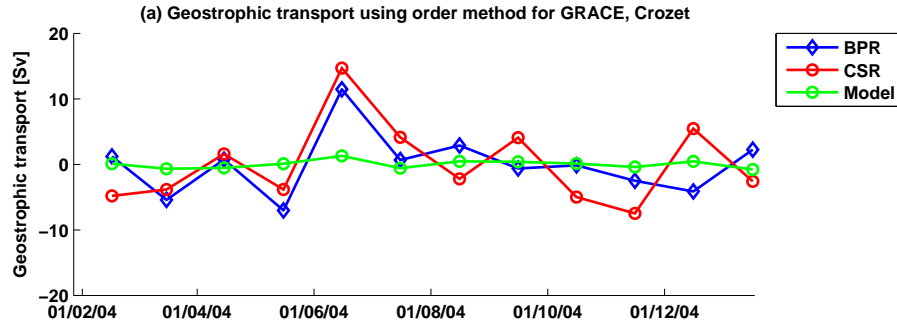


Figure B.10: Transport time series of in situ records near Crozet and GRACE (CSR).

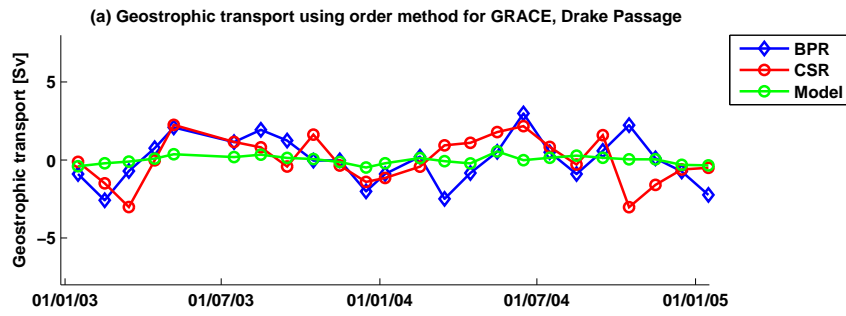


Figure B.11: Transport time series of in situ records in the Drake passage and GRACE (CSR).

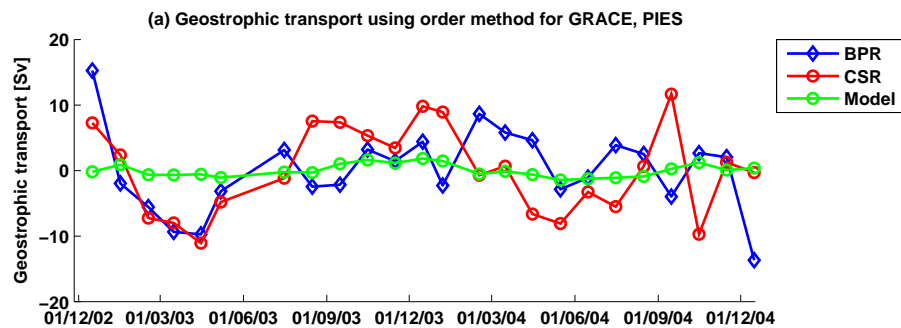


Figure B.12: Transport time series of in situ records in the South Atlantic and GRACE (CSR).

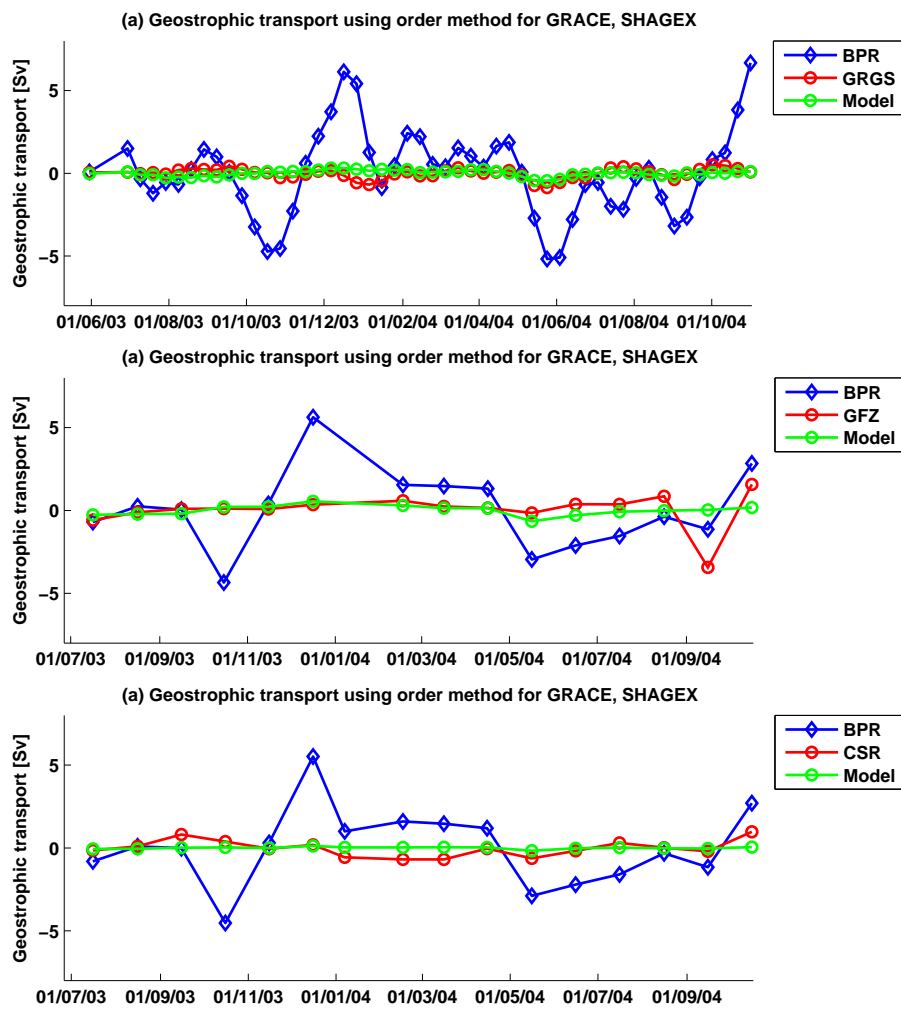


Figure B.13: Transport time series of in situ records near Shags Rock and GRACE (top:GRGS, middle:GFZ, bottom :CSR).

Appendix C

Spatial Correlation Plots

The plots below are derived from calculating the local bottom pressure series with the GRACE time series at different locations. All GRACE solutions are from GRGS and are smoothed using a 800 km smoothing radius. No time lag has been incorporated. Good correlations thus represent phenomena which are synchronous with the local BPR records. The signal to noise ratios are indicated with the contour lines. The plots for the Drake passage BPR series and the SHAGEX series are omitted as they don't display regions of important correlations.

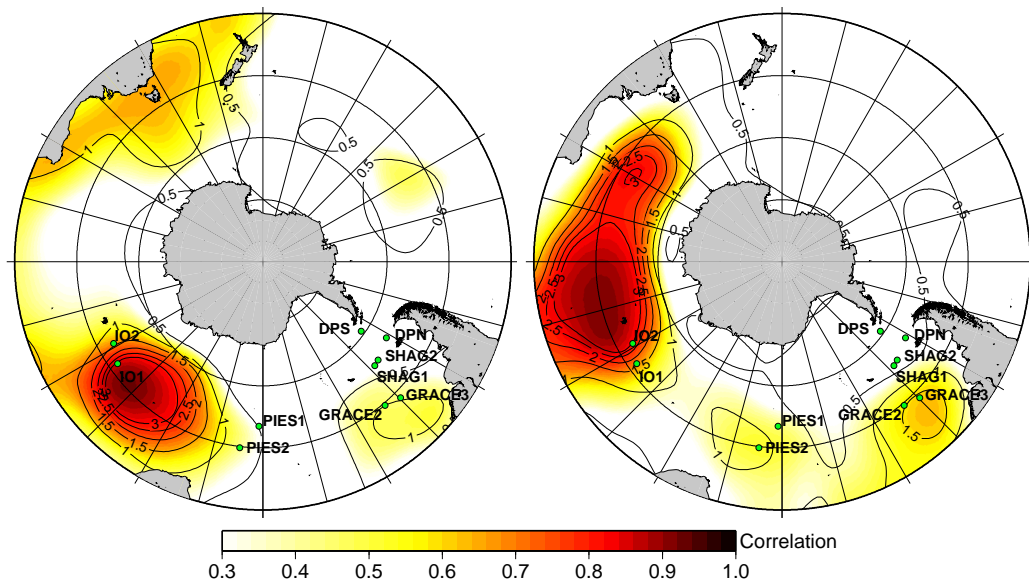


Figure C.1: Spatial correlation of IO1 (left) and IO2 with GRACE (GRGS).

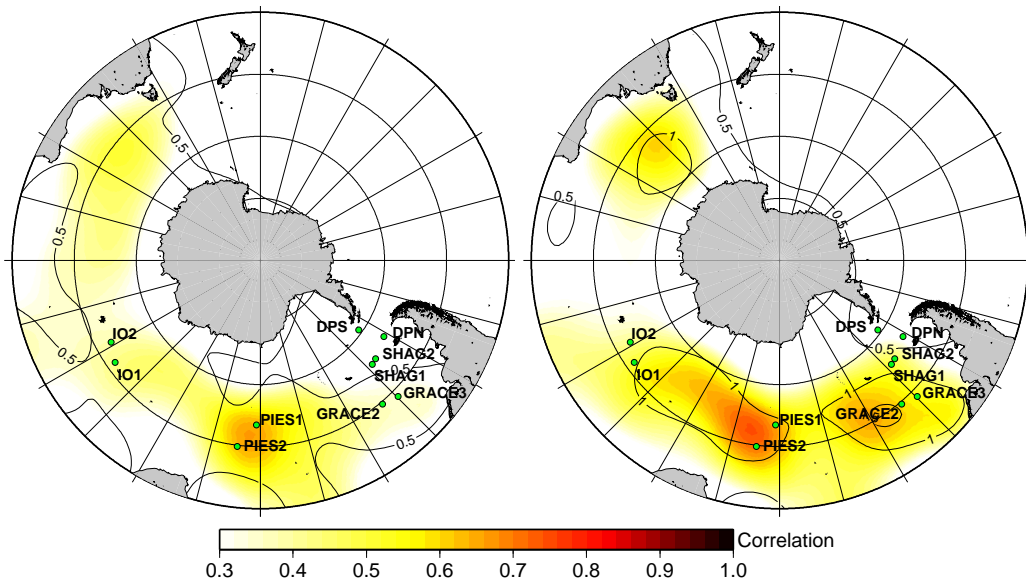


Figure C.2: Spatial correlation of PIES1 (left) and the mean of PIES1 and 2 with GRACE (GRGS).

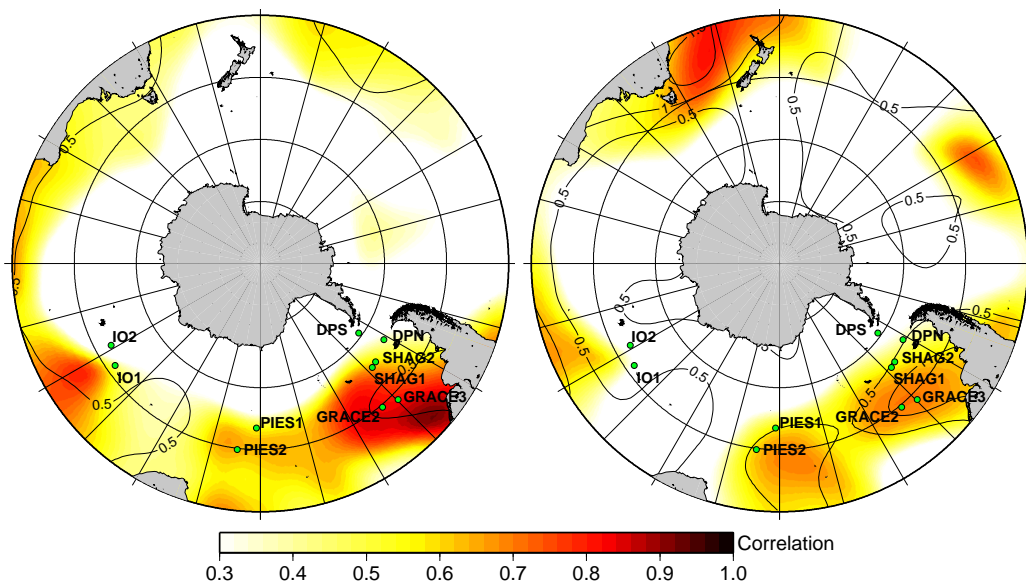


Figure C.3: Spatial correlation of grace2 (left) and grace3 with GRACE (GRGS).

Appendix D

Power Spectral Densities

The figures below display the power spectral densities of the best performing channels of the BPR records. The channels which have noisier measurements will have a stronger component in the high frequency part of the plot. The plot for the Shags rocks passage (only one channel per BPR) shows such a typical shape. The plots still show large values for the tidal constituents in the diurnal and semi-diurnal bands, however this is a relatively minor contribution compared to the raw series. All spectra are estimated using the Welch method with 8 segments overlapping by 50 %.

